Hydrogen production from irradiated aluminum hydroxide and oxyhydroxide

Josiane Kaddissy

NNT : 2016SACLS253

Thèse de doctorat

de

L'Université Paris-Saclay

préparée au

"CEA SACLAY "

ECOLE DOCTORALE N° 571

2MIB

Spécialité de doctorat Chimie

Par

Josiane Kaddissy

Titre de la thèse

Hydrogen production from irradiated aluminum hydroxide and oxyhydroxide

Thèse présentée et soutenue à «Saclay», le «03 Octobre 2016»:

Composition du Jury:

M, Mostafavi, Mehran	Professeur, LCP, Orsay	Président
M, Laverne, Jay	Professeur, Université de Notre Dame, USA	Rapporteur
M, Balanzat, Emmanuel	Directeur de recherche, CIMAP, Caen	Rapporteur
M, Saffré, Dimitri	Docteur Ingénieur, AREVA	Examinateur
M, Renault, Jean-Philippe	Chercheur CEA, CEA, Saclay	Directeur de thèse
M, Esnouf, Stéphane	Chercheur CEA, CEA, Saclay	Encadrant de thèse

Acknowledgment

As I was doing my thesis the Parable of the Talents always inspired me to go further and further with my work and never give up and I would like to share it with you:

*14 “For it will be like a man going on a journey, who called his
servants and entrusted to them his property. 15 To one he gave
five talents, to another two, to another one, to each according to
his ability. Then he went away. 16 He who had received the five
talents went at once and traded with them, and he made five
talents more. 17 So also he who had the two talents made two
talents more. 18 But he who had received the one talent went
and dug in the ground and hid his master's money.19 Now after a
long time the master of those servants came and settled accounts
with them. 20 And he who had received the five talents came
forward, bringing five talents more, saying, ‘Master, you
delivered to me five talents; here, I have made five talents
more.’ 21 His master said to him, ‘Well done, good and faithful
servant.[c] You have been faithful over a little; I will set you over
much. Enter into the joy of your master.’22 And he also who had
the two talents came forward, saying, ‘Master, you delivered to
me two talents; here, I have made two talents more.’23 His master
said to him, ‘Well done, good and faithful servant. You have been
faithful over a little; I will set you over much. Enter into the joy
of your master.’ 24 He also who had received the one talent came
forward, saying, ‘Master, I knew you to be a hard man,
reaping where you did not sow, and gathering where you
scattered no seed, 25 so I was afraid, and I went and hid your talent
in the ground. Here, you have what is yours.’26 But his master*

answered him, 'You wicked and slothful servant! You knew that I reap where I have not sown and gather where I scattered no seed? [27] Then you ought to have invested my money with the bankers, and at my coming I should have received what was my own with interest. [28] So take the talent from him and give it to him who has the ten talents. [29] For to everyone who has will more be given, and he will have an abundance. But from the one who has not, even what he has will be taken away. [30] And cast the worthless servant into the outer darkness. In that place there will be weeping and gnashing of teeth.' ***Matthew 25:14-30***

God gave each of us different talents and abilities. He expects us to develop them. These talents have to be used so others will be able to see them and benefit from them and glorify the heavenly father.

First and above all, I would like to thank God, the first and the last, whose blessings gave me the strength and patient to go all the length of this road. Thank you for being the light that shines in every darkest moment.

I would like to express my sincere gratitude to my director Jean-Philippe Renault for his scientific advises and fruitful discussions along with his supervision through the three years. As well as my supervisor Stephane Esnouf who taught me the first glances of defects created inside the solids and tried to transfer all his precious knowledge on electron paramagnetic resonance. I would like to thank them both for accepting me to do this thesis and for their guidance and help especially when I was writing the manuscript and preparing my defense. Thank you for your patience.

Besides my advisors, I would like to thank the rest of my thesis committee: Prof. Mehran Mostafavi, Prof. Jay laVerne, and Dr. Emanuel Balanzat, for their insightful comments and encouragements, but also for the hard questions which incented me to widen my research from various perspectives. Thank you for appreciating my work and giving me back my self-confidence. I could not have imagined having a better committee for my Ph.D defense, thank you for accepting to judge this work.

I would like to thank AREVA, for the financial support and also for all the technical help. I am so grateful to Dimitri Saffre who was always present to answer any question and who shared all his practical knowledge with me. It was a pleasure to work with

you. Toby Fares also helped us with fruitful discussions in the first year and I am so grateful.

My sincere thanks also go to Delphine Durand for training me on many gas spectroscopies and for trusting me to conduct all my analysis from the very beginning, thank you Delphine! I am also grateful to Vincent Dauvois for his pertinent discussions and for the organization he put inside LRMO laboratory to keep a perfect work environment. Thank you for waiting for me sometimes at night in order to finish my analysis without keeping me alone in the lab. I would like to thank Jean-Luc for his technical help sometimes and also for sharing his sense of humor I would like to thank all the LRMO especially Muriel who was always ready to answer any question and had a smile always drawn on her face. Thank you all for receiving me in your laboratory and allowing me to use research facilities, please consider all my deepest thanks.

Without the precious support of Eddy Foy at the LAPA in XRD analysis, it would not be possible to conduct this research. Thank you for always being here for help, for your clear explanation, your time and your kindness. I would like to thank Mickael Bouhier for Raman tests and for his gentleness and friendship and for Enrique Vega for SEM analysis that were also performed at the LAPA. I would like to express my gratitude to Michel Tabarant at SEARS for his ICP-AES analysis and for his efficiency and kindness. I should like to extend my special thanks to Romain Dagneli at SECR for BET measurements and support. My thanks also to Florence Porcher at the LLB for the neutron diffraction tests and for initiating me on Rietveld structure refinement. I am so grateful to Jocelyne Leroy at LICSEN for XPS analysis and for the time spent together discussing and trying to understand the alteration induced after irradiation. I would like to thank Marie-Noelle Amiot for receiving us to conduct EPR analysis at CEA. My deepest thanks go for Bruno Boizot who let us have enough time to analyze our samples in LSI- polytechnique. Thank you so much!

My deepest gratitude to my sister in law. Sahar Mouawad Kaddissy who helped me explain my set up and vessels by keeping nice Autocad and 3ds Max drawings in chapter 3.

In my daily work I have been blessed with a friendly and cheerful group. I would like to thank them all starting with Serge Pin that was always here for help and wise advices, Sophie le Caer, that had always encouraging words and pertinent scientific advices, Aurelie my special colleague and dear friend, I can’t imagine the thesis passing without you, thank you for always being here and listening to me and for making me laugh when needed louzzzz, you have a special place in my heart! Maxime thank you for your

friendship and for your jokes that always helped when I was stressed, I would like to thank you also for your open spirit and nice collaboration, we never fought on apparatus can you imagine? Laurent and your special humour, I appreciate your friendship, as well as David, Raj, Sandrine, Mickael, Gerarld, Fanny, Guangze, Imene, Imane, Dorra, Elodie, Eleonora, Daniel, Alexy, Anthoine, Yun Yun and Paul.

CEA was not only the site where I perfomed my PhD but also where I met amazing people I will never forget in my life especially Abed el Karim el Omar and Ibtihel Denden. Karim, thank you for initiating me to the basics of radiation chemistry and helping me with my irradiation experiments and also with OriginLab, thank you for your patience and for being a true brother, I am blessed and lucky to have a peaceful friend like you. Ibtihel, thank you for being a true sister in France, always careful and helpful and thank you for all your scientific advices and wise discussions you and Karim will always be not only dear friends but also trustworthy scientists.

Other past and present friends contributed both consciously and unconsciously to the achievement of the PhD especially my transition phase at Poitiers and the precious friends I met there and were always supporting me, El mekhtar Dya who was always helpful and supportive, Nissrine who showed with time what a true friend is, Joseph, Zeinab, Mohammad, Nancy, Jocelyne, Odissa, Soumaya, Haidar, and Claude Thank you! I would like to thank some true friends that were supporting me even when the wi-fi was week, thank you Nayla Tarabay and Mazloum for all your advices and love and Eliane for your belief and encouragement. Roua, Marc, Habib,Joelle, Sarah, Laure, Tarek and Stephane thank you!

Finally, I would like to thank my parents, thank you for your faith in me and for always supporting me throughout all my studies and giving me good ear even after midnight and even when you were so tired. Gisele, querida hermanita you've always been my advisor since my childhood, I am so proud of you and lucky to have you, thank you for all the effort you've done to make me be a better person. Gracias hermanita! I would like to thank my two brothers Gerard and Bernard and my sisters in law Sahar and Monie for always being here for me, checking on me, visiting me and believing in me! I love you my dear family and you have to know that without you I would not have done what I did until today.

I am especially grateful for Johnny Nawfal who was not only my boyfriend but also my best friend who watched over me and guided my choses all over these years. Thank you for listening to all my problems and trying to solve them even when yours were

bigger! You were always supporting me and your motivation and ambitions were contaminants, I am so lucky to have you and proud for all what I've learnt from you throughout the years. Thank you for your eternal love. Gracias amorcito por todo!

Résumé

Production de dihydrogène par irradiation d'hydroxyde et d'oxyhydroxide d'aluminium

Les travaux de cette thèse porte sur la compréhension des mécanismes de production d'hydrogène par radiolyse de l'hydroxyde et de l'oxohydroxide d'aluminium ($Al(OH)_3$ et AlOOH respectivement). Cette connaissance est fondamentale pour la détermination des sources de dihydrogène provenant des phases hydratées présentes à la fois dans les emballages de transport des combustibles usés et les colis de stockage.

Dans l'industrie électronucléaire l'usage de l'aluminium est fréquent. En particulier, AREVA a développé des emballages spécifiques, TN®12 ou TN®13, pour le transport terrestre et maritime des assemblages de combustible. La corrosion aqueuse (eau liquide ou vapeur) des surfaces d'aluminium conduit à la formation d'hydroxydes d'aluminium. Les hydroxydes d'aluminium présentent un polymorphisme assez riche. Dans cette thèse on s'est intéressé à la Bayerite ($Al(OH)_3$) et à la Boehmite (AlOOH) sous la forme de poudres nanométriques fournies par Sasol, Allemagne. En aval, cette thèse s'ancre dans la problématique de la sureté lors du stockage/entreposage et lors du transport de matériels irradiants, à base d'aluminium, présentant en surface des hydroxydes d'aluminium. Le risque identifié ici est celui du dihydrogène (explosivité), potentiellement émis lors de la radiolyse des hydroxydes d'aluminium.

La problématique aval s'insère dans une thématique bien plus vaste que celle stricte des hydroxydes d'aluminium abordée, parce que le risque de produire du dihydrogène se trouve très souvent dans le contexte du stockage/entreposage/transport (matériaux organiques, ciments, boues). En amont, c'est-à-dire sur le plan fondamental, cette thèse s'attaque au problème de la radiolyse de « l'eau » dite ici « solide », en comparaison à la radiolyse (bien mieux connue) de l'eau liquide. On retrouve des points communs, et bien sûr aussi des différences majeures, avec d'autres situations qui ont été étudiées récemment sous irradiation comme la radiolyse de l'eau nanoconfinée (zéolithes, géopolymères, bétons, argiles ou encore les verres de silice mésoporeux). L'étude de la radiolyse de cette « eau solide » est indissociable celle des défauts d'irradiation dans les hydrates d'alumine et donc on a étudié en parallèle la formation/émission de dihydrogène et la création de défauts d'irradiation dans le solide tout en abordant une characterisation multi-technique avant et après irradiations a fait appel à une dizaine de

techniques de caractérisation (DRX, FTIR/ATR, RAMAN, MEB, BET, ATG, RPE, ICP, XPS, analyse de gaz par chromatographie et spectrométrie de masse). et en étudiant l'effet de plusieurs paramètres sur la création de ces défaut tels que l'effet de taille, l'effet d'hydratation, d'impureté etc… Une étude préliminaire sur la brucite $Mg(OH)_2$) est présentée à la fin du manuscrit pour essayer de voir l'effet de taille et d'impureté et généraliser les résultats sur un plus grand nombre d'hydroxides. Ce manuscrit présente l'étude de deux polymorphes, des tailles de grains différentes, l'effet de l'hydratation, des impuretés, l'effet du pouvoir d'arrêt électronique (ou TEL pour Transfert d'Energie Linéaire), de la dose et des recuits. Cela permet de brosser un panorama général sur l'émission radioinduite de dihydrogène par les hydroxydes d'aluminium

Dans le premier chapitre, la littérature est présente. Dans les hydrates d'alumine, stricto sensu, on ne retrouve qu'un seul article très récent (2015) traitant du sujet, émanant du SRNL-USA. On trouve aussi deux autres articles plus anciens concernant l'étude des centres paramagnétiques par une équipe moscovite et une slovaque. C'est tout. Mentionnons aussi des études récentes sur la radiolyse de l'eau en surface d'oxydes provenant de l'Université de Notre Dame, USA.

Le plan est structuré en six chapitres, plus une introduction, une conclusion et deux courtes annexes. Les chapitres 4 et 5 présentent l'essentiel des résultats, ils concernent respectivement les matériaux secs et hydratés. Le noyau central des chapitres 4, 5 est précédé par un chapitre sur la caractérisation des matériaux non irradiés. Le chapitre 1 regroupe les rappels essentiels sur l'interaction particule matière et sur l'état de l'art en ce qui concerne la radiolyse de l'eau et les effets d'irradiation dans les hydroxydes. Considérant le contexte de ce travail, on présente, à juste titre, les deux mécanismes permettant la modification sous irradiation, les chocs balistiques (ou collisions élastiques) et l'excitation électronique (ou radiolyse). La radiolyse de l'eau est résumée en considérant l'eau dans tous ses états : eau liquide, eau gelée (glace) et eau liée (confinée et physi ou chimisorbée). Le chapitre fait aussi le point sur la création de défauts ponctuels, ici appelés centres colorés, dans les oxydes et les hydroxydes. Enfin le chapitre rappelle les quelques résultats publiés sur l'émission de dihydrogène par les hydroxydes irradiés. Le chapitre 2 se structure en trois parties. La première partie concerne les matériaux utilisés et détaille les protocoles choisis pour le de séchage et l'hydratation. La synthèse maison de grains de brucite de très petite taille (3 nm) est également présentée dans cette partie. La deuxième partie décrit les dispositifs et conditions d'irradiation ainsi que les protocoles de dosimétrie. Le chapitre se clôt par

la description des techniques de caractérisation. Le chapitre 3 présente la caractérisation des échantillons non irradiés. Les hydroxydes d'aluminium étant des matériaux complexes, il est était essentiel de partir sur des échantillons bien définis. Le chapitre se termine sur quelques résultats après des irradiations à fort TEL, supposées créer plus de modifications. En fait, on explore ici le potentiel de différentes techniques (FTIR, XRD et XPS). Aucune de ces techniques ne s'est révélée assez sensible pour étudier les modifications dans le domaine de dose de ce travail. Le chapitre quatre présente les résultats obtenus dans des échantillons « séchés » c'est-à-dire ne contenant a priori que des hydroxyles liées à l'aluminium. On s'attache donc à évaluer la contribution de « l'eau de structure » à la production de H_2. Trois matériaux différents ont été considérés : deux à « gros » grains (20 nm), bayerite et bohenite, et une bayerite à petit grains (5 nm). Les mesures de $G(H_2)$ non pas été seulement mesuré après irradiation, mais aussi lors de recuits conduits jusqu'à la température de transition de phase (les hydrates d'aluminium se décomposent alors complètement en alumine et eau). Une des questions que posent les résultats de G(H2) après irradiation et recuit est la rétention de dihydrogène et/ou de H° dans le matériau. Une des raisons évoquée est la diffusion.

La diffusion de H° devrait être encore plus rapide, mais paradoxalement la RPE montre que H° est bien présent après irradiation, au moins dans la bohemite. Une autre raison avancée pour la rétention est le piégeage de H_2 et ou H°. Ceci est séduisant mais les mécanismes et les sites de piégeage restent flous. Concernant l'effet de taille, qui est un autre point intéressant de cette thèse, on propose, pour expliquer les très faibles $G(H_2)$ dans le cas des petits grains, une hypothèse séduisante : on aurait tout au plus un H° par grain, ce qui limiterait les recombinaisons H°+H°. Le chapitre cinq présente les résultats obtenus dans des échantillons hydratés afin d'évaluer la contribution à la production de H_2 de l'eau (H_2O) adsorbée. Un des résultats marquants de cette thèse est la mise en évidence d'un fort effet d'interaction : $G(H_2)$ est bien supérieur à la valeur calculée par additivité (matériau sec + eau « libre »).
La thèse se termine par le chapitre six qui concerne une étude exploratoire sur des brucites synthétisées maison. Inévitablement, la synthèse à façon ouvre des perspectives que n'offre pas tout travail faisant appel à des matériaux commerciaux.

List of contents

List of figures

List of Tables

Introduction

During the storage or transportation of certain nuclear wastes, several gases are generated. Hydrogen is the dominant flammable gas of concern and its potential threat has drawn more and more attention.[1] The release of radiolytic hydrogen is important to quantify in order not to exceed the lower flammability limit (LFL). Usually safety demonstrations have to prove that hydrogen concentration is always lower than half of the LFL. This value corresponds to the minimum H_2 concentration necessary to support its combustion in air determined at room temperature and atmospheric pressure.[2,3]

Theoretically and practically speaking, this hazardous gas might originate from three sources: metallic corrosion, radiolytic and chemical oxidation of organic compounds in waste and radiolysis of liquid/vapor water.[1, 4]

However, a fourth source has been comparatively discounted: solid water. In fact, very significant amounts of water can be trapped in the form of hydrates or hydroxides in various materials used in the nuclear industry:

- Concretes are composed of different hydrated phases such as portlandite, $(3(CaO)\cdot 2(SiO_2)\cdot 4(H_2O))$, Gibbsite…,
- Salts such as $Mg(OH)_2$, $Ti(OH)_4$, $Co(OH)_2$ contained in co-precipitation sludges resulting from the decontamination of liquid effluents,
- Corrosion phases, for example, on aluminum fuel assembly or on flasks used in used fuel transportation.

The starting objective of our study is to gain a better understanding of hydrogen production from hydroxides found in radioactive wastes and from corrosion phases present in used fuel transportation flasks. These two themes are briefly presented below.

Used fuel transportation

Dry metal casks are concerned in our study, especially TN12 and TN 13 casks, designed by AREVA TN and used for transportation of used fuel. For nearly 40 years, these types of metal casks have been used to ship used nuclear fuel from Japan to Europe or within europe without any incident.

More detailed description as well as a scheme of the TN12 are shown in section 8.

The TN12 is made of two parts, a body and a basket designed to receive the fuel assemblies.

AREVA TN applied an anodizing film of aluminum oxide to the internal basket walls. It is this film that is of interest for us.

Depending on the aluminum surface, numerous assemblies can show corrosion and aluminum oxyhydroxides AlOOH or aluminum hydroxides $Al(OH)_3$ can be formed. This type of event can have an impact on transportation safety due to the risk of hydrogen being produced through radiolysis or the risk of damage to transported materials (e.g. fuel assemblies). [5]

Radioactive waste management

In France, liquid effluents of Low Level Activity and Intermediate Level Activity are decontaminated by using a process of insolubilisation of the radio-elements by chemical co-precipitation. This treatment permits to concentrate and immobilize the radioactivity in a solid matter. This mixture is named co-precipitation sludge and was intend to be embedded in bitumen. Following the decision of the French nuclear safety authority, some of the co-precipitation sludges could not be embedded in bitumen. Therefore AREVA NC develops a new process that permits to store the mixture of the mineral co-precipitation salts in the form of dry pellets

Therefore cementing is considered by the CEA. In this context it is important to know the impact of different parameters on radiolytic hydrogen production in these salts such as crystallite sizes, presence of impurities and relative humidity.

Recently, the radiolysis of $Al(OH)_3$ and AlOOH under γ irradiation was studied and hydrogen production from dry samples was quantified.[6] We chose to study this type of hydroxides because above all many structure variations exist such as $Al(OH)_3$, AlOOH, Al_2O_3. Therefore, molecular hydrogen production can be studied with respect to different form of water.

The main goal of the project is to better understand the mechanisms involved in the radiolysis of aluminum hydroxides and oxyhydroxides in particular chosen as a prototype for other hydroxides encountered in the nuclear waste industry.

We tried to take into account the fact that i) the hydroxide could be formed with different crystallite/particulate sizes, ii) the irradiation could occur in the presence or absence of humidity iii) the irradiated hydroxide could be subject to temperature elevation during transportation stage, for instance.

As a first step, the determination of molecular hydrogen production was evaluated with respect to structure and particle size. Actually little information exists relating particle size to hydrogen production.[7-8]

As a second step, the effect of adsorbed water and structural water on the molecular hydrogen production was studied. Different radiation sources were used such as Gamma radiation, electron beam radiations and heavy ions.

In the last part, preliminary results related to the impact of impurities on hydrogen production are shown.

To complete, radiation induced defects were identified and characterized. The main objective of these analyses is to identify the precursors of molecular hydrogen.

The novelty of this study resides in the quantification of molecular hydrogen not only at room temperature as it is commonly done but also by annealing at high temperature. Annealing was also used to study the thermal stability of the defects induced by radiation.

« Ne vous découragez pas, c'est souvent la dernière clef du trousseau qui ouvre la porte »

Le manuscrit retrouvé, Paulo Coehlo

1. Chapter 1: Literature review

This chapter sets the background to the thesis, introducing the basis of interaction of radiation with matter and the classification of ionizing radiations. This is followed by introducing water under its different forms and its behavior under irradiation. At the end, a state-of-the-art on the radiolysis of adsorbed and confined water in oxides and hydroxides is briefly explained followed by a general overview on their effects on hydroxides.

1.1 Absorption of radiation energy

In order to initiate radiation-chemical reactions or create point defects in non- metallic materials, ionizing radiations are used. These are composed of photons (gamma or X-ray, bremsstrahlung), accelerated particles (electrons, light ions, swift heavy ions) and particles ejected from radioactive emitters (α or β particles).

Electronic and nuclear energy loss can occur in irradiated materials.

Electronic energy loss is related to inelastic "collision", that is, ionization and excitation of target materials, and the nuclear is responsible for elastic collision, that is, displacement of atoms from the original sites. Electronic energy loss is predominant over nuclear for high energy ion.[9]

The linear energy transfer, abbreviated LET is conventionally used to describe the energy transfer per unit length of the track of the primary particle or secondary particle in the case of radiation or neutrons. It can be written as -dE/dx, where E is the energy deposited or lost and x is the depth.[10-12] Classically we differentiate between high-LET radiations that deposit energy densely along the path of the ionizing particle and low-LET during which energy is discretely deposited in the path of the ionizing particle.

Figure 1.1 specifies the variation of the LET for different types of radiations. The penetration of particles in matters is inversely related to their LET. For the same energy the particle with lower LET has a better penetrating comparing to a higher LET.[13]

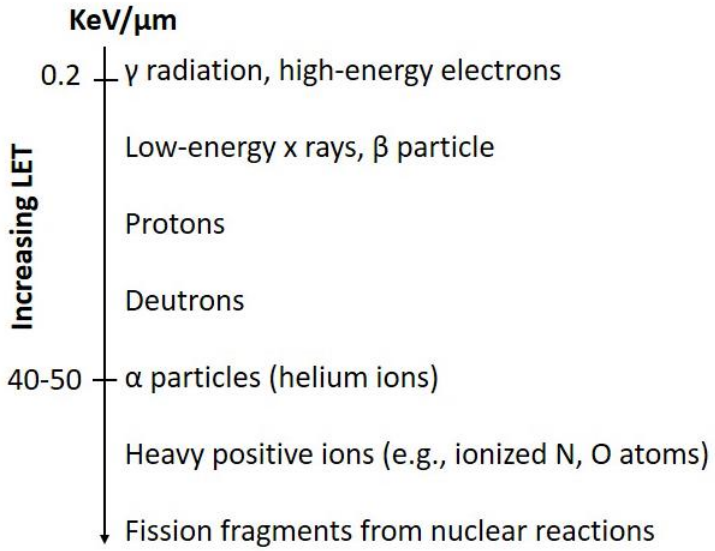

Figure 1.1. Variation of LET for different types of radiations and particles (from 0.2 keV/µm to above 50 keV/µm).[13]

Charged particles generally lose energy continuously through a large number of small energy transfers as they pass through matter.

It is admitted that all types of high energy ionizing radiations induce similar chemical changes in the irradiated material, although the relative proportions of the chemical products formed may differ.

The following section briefly describes the process by which fast electrons, ions and electromagnetic radiations interact with matter.

1.1.1 Electron

Elastic and inelastic scattering and emission of electromagnetic radiations are the most important processes occurring by the interaction of electrons (and positrons) with matter.

Radiation emission is favored when we have high electron energies and high atomic number (Z) while at low energies elastic and inelastic scatterings are favored. [13]

Electron accelerators are the most widely used machine sources, this is due to the relatively high power available in electron beams, the extremely low probability of inducing radioactivity in the irradiated products, and that the fact that the beams can be turned on or off at will unlike gamma irradiation facilities.[14] Electron beams generated by accelerators are monoenergetic and they give a uniform distribution of adsorbed dose in the irradiated matter. Electron beams are used for research purposes such as

pulse radiolysis or for processing applications, higher energy beams are utilized in nuclear physics.

Mainly three types of electron accelerators exist:[15]

- Electrostatic accelerators that produce continuous electron beam between 0.1-5 MeV (Van de Graff and Pelletron)
- Rhodotron ® accelerators based on recirculating a beam through successive diameters of a single coaxial cavity resonating in metric waves (2-10 MeV)
- Linear accelerators (LINAC) which deliver accelerated electrons in pulses of ns or micro second duration with a repetition of 1-500 Hz.
  High energies are delivered between 10 and 30 MeV.

1.1.2 Swift heavy ion

Ion accelerators can be classified according to the beam energy delivered as three categories:

- Low energy (1-10^2 MeV)
- Medium energy (10^2-10^4 MeV)
- High energy > 1 GeV

Interactions occurring with positive-ion radiations are the same as those with electrons. However, radiation is important here only at a very high energies (1000 MeV), elastic scattering is relatively unimportant and energy loss is principally by inelastic collisions with the electrons of the stopping material.

Positive ions travel in very nearly straight paths and are slowed down gradually as a result of a large number of small energy losses. Since each ion starts with the same energy, all ions will have about the same range, although the random nature of collisions gives rise to small variations in the range of individual ions. Compared to gamma rays and electron beams, ion beam has potential advantages such as a large and localized energy, production of a wider variety of secondary products and transmutability of material including nuclear reactions. Positive ion beams are used in radiation-physical technology in applications such as ion implantation and hardening metal surfaces.[13, 16]

1.1.3 Electromagnetic radiations X and gamma rays

Photons constituting electromagnetic radiations tend to lose a relatively large amount of energy whenever they interact with matter. They lose energy gradually through a number of energy-transfer events like electrons and other charged particles but the

greater part of their energy is lost through a single interaction. This results in a complete adsorption of the incident photon.[17]

High-energy photons interact with matter through:

- Photoelectric effects at low energies : 1-10^2 keV
- Compton scattering at higher energies : 10^2 - 10^4 keV
- Electron positron pair production for energy higher than 1.02 MeV and for materials containing heavy atoms

This interaction induces the formation of secondary electrons that interact with the target to produce transient species. Two artificial radioisotopes widely used as gamma radiation sources are ^{60}Co (activity 1.9-3.7 TBq/g) produced by exposing natural cobalt ^{59}Co to neutrons in a nuclear reactors and ^{137}Cs (activity 0.93 TBq/g) separated from the mixed fission fragments present in spent nuclear fuel elements and the radioisotope is available in the form of chloride. ^{60}Co decays to give an excited state of ^{60}Ni and ^{137} Cs which decays giving the ground state ^{137} Ba (Figure 1.2).[13]

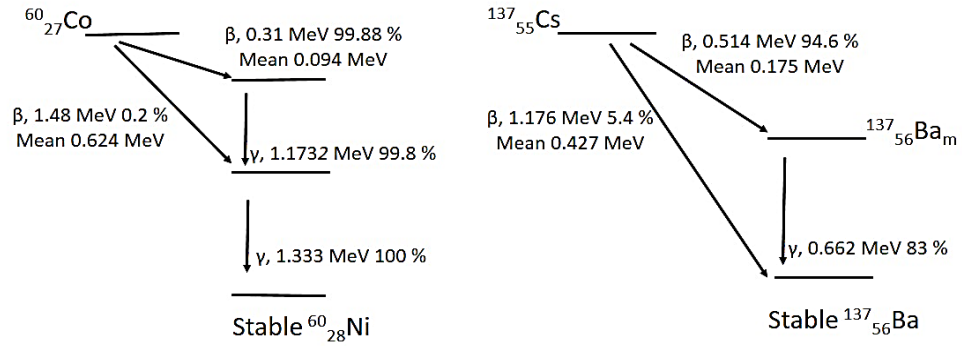

Figure 1.2. Radioactive decay of the γ-emitting isotopes: ^{60}Co and ^{137} Cs.[13]

1.2 Creation of defects

Defects can be created either by elastic collision or by electronic excitation.

1.2.1 Elastic collisions

Elastic collisions are direct mechanisms. For a given type of atom, the number of displacements per atom (dpa) can be calculated by the equation

$$dpa = \sigma_d \phi$$

Where σ_d is the atomic displacement cross section by elastic collisions and ϕ is the particle fluence.

The displacement cross section σ_d is directly determined by the threshold displacement energy E_d:

$$\sigma_d(E, E_d) = \int_{E_d}^{E_{max}} N(T) \frac{d\sigma}{dT} dT \quad \textbf{(1)}$$

where E is the kinetic energy of the incident particle, E_{max} is the maximal energy transferred to the target atom, $N(T)$ is the number of primary and secondary displaced atoms, and $d\sigma/dT$ is the differential elastic collision cross section. In the case of electron irradiation, the maximum energy T_m transferred by an electron is given by the following formula:

$$T_m \approx (2m_e/M)[(E + 2m_e c^2)\, E/m_e c^2] \quad \textbf{(2)}$$

E is the kinetic energy of the electron, M is the mass of target atoms and $m_e c^2 = 511\, keV$.

The cross section for displacement damage σ_d can be evaluated using Darwin-Rutherford formula:

$$\sigma_d(barns) = 0.2495 \left(\frac{Z^2}{\beta^4 \gamma^2}\right)\left[\frac{T_m}{T_d} - 1\right] \quad \textbf{(3)}$$

With $\beta = v/c$ and $\gamma = 1/\sqrt{1-\beta^2}$. Z is the atomic number of target atoms, v is the electron velocity and T_d the threshold energy. It is supposed that below T_d the displacement probability is zero while for energy greater than $T_d$is unity.

The average threshold energies of O and Al in Al_2O_3 are comprised between 41-90 eV and 18-24 eV, respectively.[18]

For polyatomic targets, σ_d is evaluated using the programs developed by Lesueur. [19] The calculations are based on the Kinchin–Pease model [20], they gave the displacement cross section as a function of the electron energy in polyatomic solids for different values of T_d.

1.2.2 Electronic excitation

In this case the projectile interacts with the electron of the target and transfers part of its energy. This perturbation of the electronic structure of the target can modify the local atomic structure and can induce defects formation. As the processes are often complex and indirect it is impossible to calculate the number of atoms that are displaced from their sites.

The concentration of defects results from the amount of energy absorbed by the material and a creation yield that must be measured. Then two basic concepts have to be defined: the dose and the radiolytic yield.

1.2.3 Absorbed dose

In insulator, the extent of modifications induced by inelastic collisions in a given material depends on the absorbed dose, which corresponds to the energy deposited by the radiation per unit mass of material. Its unit is the gray, Gy, and 1 Gy corresponds to 1 Joule of energy deposited in 1 kg of material ($1Gy = 1\ J{\cdot}kg^{-1}$)[1].

1.2.4 Radiolytic yield

Radiolytic yield concept, widely used today, was introduced in order to quantify the effect of radiation.

In 1952, Milton Burton suggested the G-value as the radiolytic yield which represents the number of molecules created or destroyed (M) per 100 eV of energy deposited in the system.[21]

The International System of units expresses G yield in mol/J where 1 molecule (100 eV) = $1.036\ 10^{-7}$ mol/J.

1.2.5 Elastic or Inelastic collisions

In practice, for some given irradiation conditions, it is important to determine what is the main process do defects creation. Then the ratio of the number of defects created by inelastic collisions $N_{inelas.}$ to the number of atoms displaced by elastic collisions $N_{elas.}$ can be evaluated:

$$\frac{N_{inelas.}}{N_{elas.}} = \frac{10^9 \cdot \left(-\frac{dE}{dx}\right)_{inelas.} \cdot e \cdot G}{N_0 \cdot \sigma_d} \quad \textbf{(4)}$$

Where $\left(-\frac{dE}{dx}\right)_{inelas.}$ is the stopping power for inelastic collisions (unity: $MeV.cm^2.g^{-1}$), G is the yield of formation of defects and N_0 is the number of atoms/cm^2 and $\sigma_d$is the surface area.

Using the lowest displacement threshold energy of Al determined for Al_2O_3, we estimated that if electron energy exceeded 1 MeV and G exceeds 10^{-10} mol/J, the

[1] In the earlier literature, doses were expressed in terms of Megarads: 1 Mrad = 10 kGy.

dominating process of defect creation is inelastic collisions (i.e radiolysis of the material).

The radiolysis of water is well known today, the next section describes some phenomena occurring in liquid water that may help us understand that of solid water. The value of radiolytic yield of H_2 formed in water would serve as a reference to compare our results.

1.3 Radiolysis of water

1.3.1 Different types of water

Four types of water can be described in the samples studied in this thesis:

- Physically adsorbed water that can be expelled from the sample without altering its structure
- Chemisorbed water strongly bound to the surface and is not expelled at low temperatures as physisorbed water
- Structural water supposed as hydroxyl groups forming the sample such as OH linked to Al in the structure $Al(OH)_3$
- Water of crystallization that consists of the intermolecular water trapped inside the structure and is not removed when heating and treating sample under vacuum.

They are depicted in Figure 1.3.

A number of measurements are carried out in order to depict water in contact with solids. Such measurements include TGA, IR, X-Ray, neutron diffraction, polarizing microscopy and solid-state NMR.

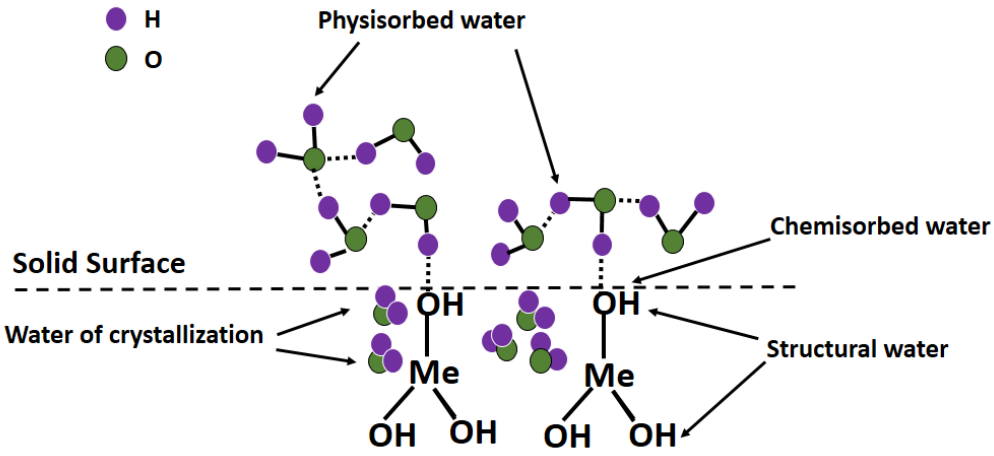

Figure 1.3. Surface states of alumina showing water in its four forms.

In the studied systems, the more important type of water is structural water, but on highly divided materials, chemisorbed and physisorbed water are important.

1.3.2 Liquid water

This section is briefly described and only basic knowledge on water radiolysis is given. When exposed to radiation, the ionization of water molecules occurs leading to the formation of various ion species, radicals and new molecules.[7]

Water radiolysis can be written as:

(5)

$$H_2O \rightarrow e_{aq}^-, HO^\bullet, H^\bullet, HO_2^\bullet, H_3O^+, H_2O_2, H_2$$

A few nanoseconds after irradiation in water, the following species are present:

$HO^\bullet$, $H^\bullet$, $HO_2^\bullet$, H_3O^+, OH^-, H_2O_2, H_2 of which the following are stable: H_2O_2, H_2, H_3O^+, and short-lived free radicals e^-_{aq}, $HO^\bullet$, $H^\bullet$, $HO_2^\bullet$.

Typically, water radiolysis flows in two main stages: the *non-homogenous* and *homogenous stages*.[22]

This first consists of three main stages taking place on different typical time scales (Figure 1.4): [13]

- *The physical stage*, which is achieved fs after the initial matter-ionizing radiation interaction, consists in energy followed by fast relaxation processes. This leads to the formation of ionized water molecules (H_2O^+), excited water molecules (H_2O^*) and sub-excitations electrons (e^-).
- *Physico-chemical stage*, which takes about 10^{-12} s after the passage of ionizing radiations, numerous processes occur including ion-molecule reaction,

dissociative reaction, auto ionization of excited states, thermalization of sub excitation electrons (solvation of electrons), hole diffusion and so on.

- *Chemical stage*, starts at 10^{-12} s and is achieved at 200 ns after the passage of ionizing radiations. It is the phase in which reactions occur between species formed in previous steps: recombination between radicals, ions, molecules and free electrons.

The *homogenous stage* is signed by the diffusion of species contained in the spurs that are small zone where transient intermediates are created. It is achieved in 100 ns after the passage of ionizing radiations.

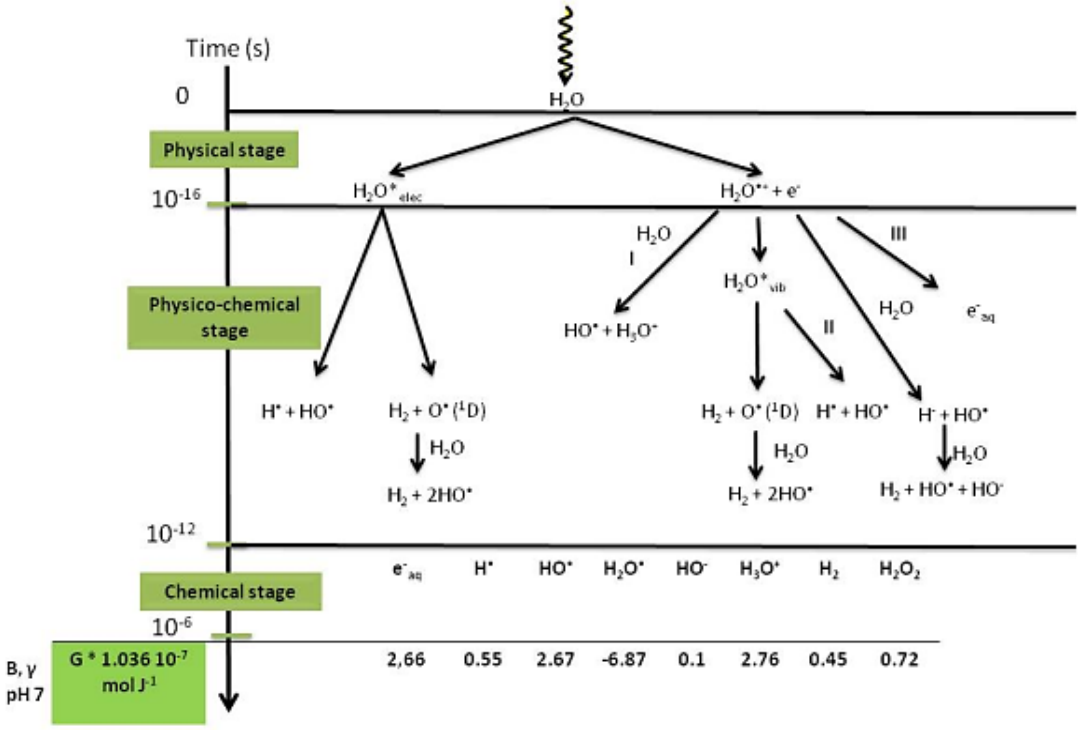

Figure 1.4. Main reactions arising from the radiolysis of liquid water and associated time scales.[23]

It is worth noting here that three types of radiolytic yields may exist depending on the time species are measured. In our study only the global radiolytic yields are considered.

- Initial radiolytic yields $\boldsymbol{G°(X)}$

  These yields are related to species produced at the end of the physichochemical stage in the irradiated material, in other words at almost 10^{-12} s after the passage of radiation ions. These yields are difficult to measure since they are formed at a very short time.

- Primary radiolytic yields, $\boldsymbol{g(X)}$

These yields are related to radical and molecular species that escaped from the ionization cluster at 1 microsecond after the passage of ionizing radiation. They have an homogenous distribution in the system.

- Global or apparent radiolytic yields, $\boldsymbol{G(X)}$

  These yields are attributed to that measured few minutes after the passage of ionizing radiations. These are essentially attributed to radiolytic yields of species formed from stationary radiolytic reactions.

Radiolytic yields of the primary species formed from the radiolysis of liquid water at pH=7 are resumed at the bottom of Figure 1.4 and recalled in Table 1.1.

Table 1.1: Radiolytic yields of primary species formed during water radiolysis.[23]

	$\mathbf{e_{aq}^-}$	$\mathbf{H^\circ}$	$\mathbf{HO^\circ}$	$\mathbf{H_2O}$	$\mathbf{HO^-}$	$\mathbf{H_3O^+}$	$\mathbf{H_2}$	$\boldsymbol{H_2O_2}$
G (mol/J) x 10^{-7}	2.57	0.53	2.58	-6.63	0.10	2.66	0.43	0.69

1.3.3 Adsorbed water

Since the pioneer work of Caffrey and al, the adsorption of molecules on minerals is well known to enhance their degradation.[24] This result is attributed to exciton energy transfer between the solids and the adsorbed molecules.

1.3.3.1 Physisorbed and chemisorbed water

It has been shown that a small amount of physisorbed water may lead to a large yield of H_2 such as in the case of FeO and Fe_2O_3 and other oxides where H_2 yields were several orders of magnitude greater than that of bulk water.[25] To conclude, there are three types of oxide:

- Oxides with a $G(H_2)$ < G(bulk water) such as MnO_2, Cr_2O_3 and ZnO (0.001-0.01 molecules/100eV),
- Oxides with a $G(H_2)$ close to G(bulk water) such as TiO_2, SiO_2, V_2O_5, NiO and CdO (0. 1-1 molecules/100eV),
- Oxides with a $G(H_2)$ > G(bulk water) such as La_2O_3, ZrO_2 and MgO (50-100 molecules/100eV).

The very high values measured for the latter categories can only be explained on the assumption of a diffusion of energy from the oxide into the adsorbed water leading to an apparent excess formation of H_2.

The currently proposed mechanism is an exciton transfer

(6)

$$MeO_x \rightarrow e^- + H^+$$

(7)

$$e^- + H^+ \rightarrow exciton$$

Exciton has a mean life time of about 150 fs. Exciton, electron and hole are the main mobile species on the very short time. They have two destinies: they will be either trapped by interstitial sites or diffuse to the surface where they initiate chemical reaction with the adsorbed water:

(8)

$$MeOH + exciton \rightarrow SiO^{\circ} + H^{\circ}$$

(9)

$$H^{\circ} + H^{\circ} \rightarrow H_2$$

Electron, hole and exciton are not the only precursors of H_2. Hole electrons or H atoms may pass through the interface and produce H_2 by dissociative attachment reactions while exciton at the surface may also transfer energy to the confined water leading to H_2 production by excited state dissolution.[7-8] Many species are still unknown and the mechanism responsible of the production of H_2 is still not clear.

First radiolysis study on wet silica gel, alumina and silica alumina was made in 1962 followed by the study on quartz in 1965.[26-27] Trapped H atoms were detected inside the sample cavities using EPR analysis. However, the most detailed studies have been conducted on zeolites and will be described in the next section.

Controlled-pore glasses (CPG) have been studied and pore size ranged from 8 to 300 nm.[7] For hydrated and dry glasses, the H_2 production increases when the pore size decreases. Two assumptions were used to explain the increase of $G(H_2)$ when the pore size decreases: a) limited distance of exciton migration to the surface and b) the process is controlled by the number of silanol available at the surface.

Moreover, H_2 measured using 10-MeV electrons pulses are smaller than those obtained under gamma irradiation. A possible explanation would be the reaction of H_2 precursors with unstable species, that can be accumulated at high dose rate but whose steady-state concentration would be too low at low doses. Radiolytic yields of dry and hydrated CPG are resumed in Table 1.2.

Table 1.2. Evolution of molecular hydrogen yields G(H_2) from dry Gamma and electron irradiated CPG as a function of pore size. [7] The dose rate is 1.7 Gy/ns for pulsed electron irradiation and 2 Gy/min for gamma irradiation.

Pore diameter of the glass (nm)	Electron	Gamma
8	$(2.4\pm0.9)\times10^{-9}$	$(2.2\pm0.1)\times10^{-7}$
25	$(1.7\pm0.3)\times10^{-9}$	Non determined
50	$(1.3\pm0.1)\times10^{-9}$	$(3.2\pm0.4)\times10^{-7}$
300	$(5.1\pm0.4)\times10^{-10}$	$(2.1\pm0.1)\times10^{-7}$

1.3.3.2 Water trapped in Zeolite

It has been shown that the nature of chemical interactions between water and the absorbent differs when comparing porous materials such as silica gel to zeolites. In the case of silica gel, water molecules are adsorbed on surface hydroxyls which act as active sites in energy-transfer phenomena.[28] In zeolite water systems, the cation is often considered as the adsorption site of water but the anionic oxygen atoms are preferred as active sites for energy transfer.[29]

Depending on the zeolite type, the behavior with respect to radiation may differ. Molecular sieve zeolites 3A, 4A and 5A (representing pore size 3Å, 4Å and 5Å respectively) were studied and showed different dependence of adsorbed water. 3Å interestingly showed that framework oxygen atoms of zeolite structure are active sites for energy transfer rather than cations contained in zeolite cavities.

The size of cation in zeolite cavity seems to affect the chemical interaction between adsorbed water and active sites for energy transfer.[30] A part from the A type zeolite, Y type was investigated and dehydroxylated zeolite (NaY) containing different acidic sites were conceived depending on the calcination temperature used to vary the acidic strength. This Y type was compared to a decationated form (HY) characterized by its structural hydroxyl groups. It has been showed that when no physisorbed water is present, H atoms are formed from the decomposition of surface hydroxyl groups. $G(H_2)$ and $G(H)$ are produced by, the contribution of Lewis sites formed during dihydroxylation and Bronsted acidic nature of hydroxyl groups.[29]

It has been demonstrated that not only specific surface area is important in the production of H_2 but also the cavity size. In the case of zeolite, smaller sized cavities

released higher H_2.[31] Molecular hydrogen production has been enhanced compared with bulk water due to energy transfer. The enhancement can be multiplied by three and increased with increasing water quantity interacting with the zeolite and was between $6.2x10^{-9}$ mol/J for 3.1 % of water and $1.7x10^{-8}$ mol/J for 19.1%. Increasing the organization of water seems to decrease the hydrogen production. Compared to liquid water, a modification of the migration properties of the intermediate species of radiolysis may be implied in confined water and a perturbation of the recombination mechanisms may occur resulting in the excessive production of hydrogen compared to free liquid water.[32]

1.4 Water in a solid state

Ice radiolysis was also studied and would be interesting comparing to water of crystallization. Chemical effects of ionizing radiation are harder to interpret on ice than in liquid water. Many authors were interested by the irradiation of crystalline D_2O and H_2O ice.[33,34,35] NEXAFS spectroscopy was used to bring great information on the structure of ice and its surface reactivity.[36-37]

Irradiation alters the structure of ice and produces H, H_2, O_2, H_2O_2 and HO_2 as shown in Figure 1.5.[33]

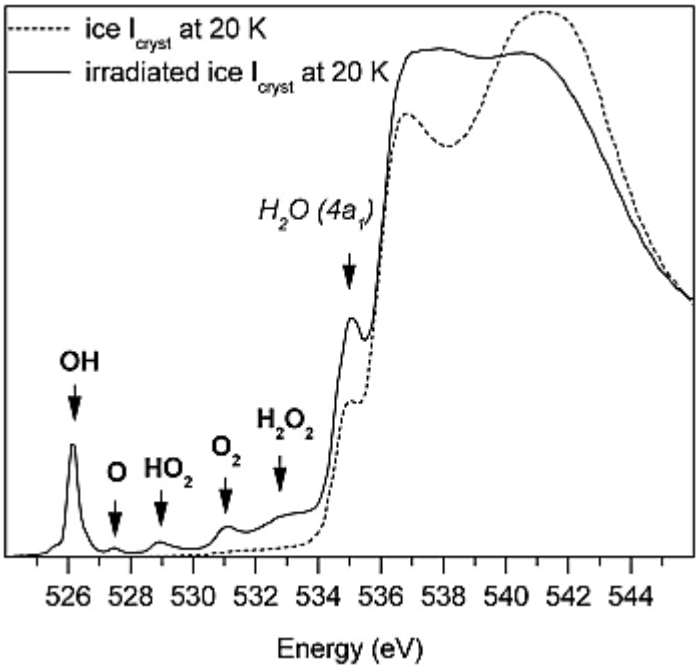

Figure 1.5. Crystalline ice film deposited at 150 K and cooled at 20 K before irradiation (dashed line) and after irradiation at saturation (full line). The arrows indicate the spectral fingerprints

of each photolysis product, except for the peak labeled H_2O (4a1) , which is the 4a1 state of condensed water.[33]

After irradiation and at greater doses, a disorder could occur and crystallized water becomes amorphous. In 1979, Gills [36] demonstrated that the irradiation of crystalline D_2O leans to the production of two types of localized excess electrons having different behaviors related to dose per pulse, temperature and doping with certain additives: One type has an absorption band in the visible and the other in the infrared.

Direct and simultaneous observation of the induced irradiation products is hard because of the lack of techniques. O^- were seen to be formed in Gamma irradiated D_2O at 77 K.[35] Table 1.3 resumes some H_2 radiolytic yields deduced from the literature. In general, radiolytic yields are lower than that of bulk water. Two explanations may be possible:

- Firstly, in solids free radicals are certainly less mobile
- Secondly, energy transfer by means of excitons may be important and promotes recombination of electron and holes.

Table 1.3. Hydrogen yields measured for irradiated ice.

Temperature	Irradiation source	$G(H_2)$ (mol/J) x 10^{-7}	Reference
-80°C and -196°C	α-ray	0.7	[38]
-196°C	self-irradiation	0.27	[39]
-15°C	X-ray	0.25	[34]
-80°C	α-ray	0.14	[40]
-100°C	X-ray	0.1	[34]
-180°C	X-ray	0	[41]

1.5 Irradiated Hydroxides

The main changes that occur in a hydroxide subjected to irradiation are creation of color defects, H atoms and molecular hydrogen.

First some definitions about color centers will be presented. Some examples will be given for Al_2O_3 because this material is interesting for our study.

1.5.1 Definition of color centers

When a semiconductor or an insulator is irradiated with high energy radiation, one of the primary processes is the creation of electron-hole pairs. The pair-creation energy ϵ is approximatively 3 times the band gap E_g.[42] Holes and electrons created by radiation can be trapped by impurities (compensators in the case of doping) or lattice imperfections. Point defects such as interstitials (lattice atom or ion displaced from its normal site) or vacancy (lattice ion missing from its normal site) can be native defects or created by elastic collisions. In ionic solids, point defects can be either anionic or cationic. These defects can be detected by various techniques, especially electron paramagnetic resonance and optical absorption. [43]

In conclusion, a change of charge state of an impurity in an insulator is a common product of ionizing radiation. Depending on the nature of the host lattice and the type of impurity electrons or holes are captured. The temperature has a major role also in the stability of the centers. In ionic crystals there is a wide variety of defects due to the presence of both cation and anion sub-lattices, the multiplicity of charge states and different type of impurities. Different nomenclatures of defects exist. Numerous authors use Kroger-Vink notation. Hayes and Stoneham propose another nomenclature that is resumed below: [22]

- F centers: negative-ion vacancies containing the same number of electrons as the charge of the normal lattice ion. F centers can be vacancies with one or two electrons.
- V centers: positive-ion vacancies whose neighbors contain the same number of holes as the charge of the normal lattice ion that is missing.
- H centers: negative-ion interstitial atoms that has combined with a lattice ion so that a molecular ion shares a normal lattice site. It doesn't have a net charge compared to the perfect lattice.[44]

When the center is adjacent to an impurity, the nature is specified by subscripts, for example, a F-center adjacent to a Na impurity is written F_{Na}. The charge state is referred to the normal charge state of the lattice site. The valence of the center is represented by the superscript, for example, a V-center with a net negative charge is written V^-. These defects are schematized in Figure 1.6.

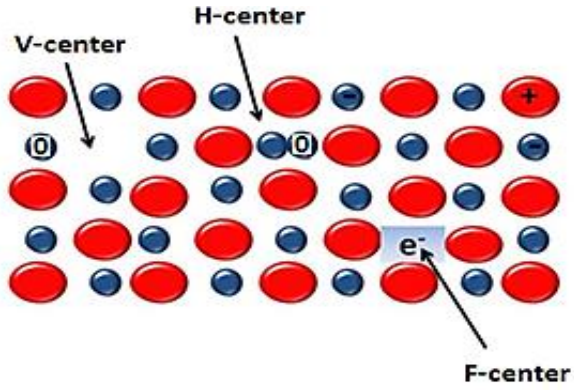

Figure 1.6. Illustration of radiation-induced color centers.

Substitutional impurities are designated by specifying the ion under brackets, for example, in oxide the two common type of substitutional impurities are $[Y^{-}]$ or $[Me^{3+}]$ where Y and Me denote anion and metal ion respectively.

In oxides the hole is trapped at a cationic defect (cation vacancy or charge deficient cation) site and is localized on neighboring oxygen. It is trapped in the $2p_z$ oxygen orbital pointing towards the cationic defect. The resulting center is a O^- ion, it has a spin ½ and the g-factor anisotropy is determined by the axial component of the crystal field and is given by: [45]

(10)

$$g_z = g_e$$

(11)

$$g_x = g_y = g_e - \frac{2\lambda}{\Delta}$$

g_e: free electron g-factor

$\lambda = -0.017\ eV$: spin-orbit coupling constant of the O^- ion

Δ: energy splitting creating by the cationic defect

To sum up the ESR spectrum of a O^- ion is an axial anisotropic line with $\boldsymbol{g_x = g_y > g_z \approx g_e}$.

Another important defect identified in oxide is superoxide center O_2^-. In this case the hole trapped in a π-type molecular orbital made of $2p_x$, $2P_y$ oxygen orbitals. When O_2^- is trapped in a solid, the g-factor is given when $\delta \gg \lambda$:

(12)

$$g_y = g_e$$

(13)

$$g_x = g_e + \frac{2\lambda}{\Delta}$$

(14)

$$g_z = g_e + \frac{2\lambda}{\delta}$$

$\lambda = 0.014\ eV$: spin-orbit coupling constant of the O_2^-

Δ: energy splitting between the ground state and the antibondong π_g^* orbital containing the unpaired electron

δ: energy splitting of the π_g^* manifold

To sum up the ESR spectrum of a $\boldsymbol{O_2^-}$ center is an anisotropic line with $\boldsymbol{g_z > g_x > g_y \approx g_e}$.

1.5.2 Colors centers in oxides

Irradiation of oxides such as MgO, BaO, CaO, Al_2O_3 and so on by energetic particles leads to the displacement of an atom into an interstitial position leaving a vacancy behind, and forming what is commonly called a Frenkel defect. Interstitial and vacancy can be neutral. Anionic vacancies can trap one or two electrons (so-called F centers) and cationic vacancies can trap holes (so-called V-centers).[18]

V centers in alkaline earth oxides were shown to be intimately connected with impurities such as Na^+, Li^+, F^- and OH^-.[46] In insulator as the overall charge must be conserved, it is easy to state that impurities play an important role in the stabilization of defects. It has been also shown that the overall number of anion vacancies is determined by a number of factors: [29]

- The concentration of Mg^{2+} and other acceptor type impurities such as Ca^{2+}, L^+, N^{3-}…
- The concentration of the compensation donor type impurities such as Si^{4+}, Ti^{4+}, F^-, OH^-…

Table 1.4 gives a summary of some results obtained in Al_2O_3.

Gamble et al studied gamma-irradiated single crystals of Al_2O_3 at 77 K.[45] They observed a single asymmetric, anisotropic line with $g_z = 2.012$, $g_x = g_y = 2.008$ and $\Delta H_{pp} \sim 5\ mT$. This line was decomposed in three Gaussian components with isotropic g values: $g_1 = 2.020$, $g_2 = 2.006$ and $g_3 = 2.006$. The first two components are attributed to a trapped hole localized on an anion adjacent to a charge deficient cation site and the last one to a single electron trapped at an anion vacancy.

Cox using Al_2O_3 doped with Mg, Li and Ti, identified ESR parameters of one hole centers $[O^-Mg^{2+}]$, $[O^-Li^+]^-$ and V^{2-}.[47] He also observed S=1 centers attributed to the localization of two holes on two anions neighbors of the cation defect.

By comparing EPR spectra of pure and Fe-doped single crystals of Al_2O_3 irradiated using gamma at 77 K, Bauer and Whitmore suggested that one center is created and correspond to a trapped hole localized on an anion adjacent to a substitutional divalent iron.[20]

Lee et al showed that V_{oH}^{-} centers are observed in gamma irradiated Al_2O_3 at 300 K.[30] These centers disappears upon oxidation of Al_2O_3 at 1350°C in air. In oxidizing samples, two holes centers V^{-} are observed. They anneal out at 380 K and are replaced by another hole center V^{2-}.

Fe^{3+} and Cr^{3+} were found in pure Al_2O_3 located in substitutional cation sites. Cr^{3+} was also detected in aluminum oxide.[48] Fe^{3+} impurities are presented by an EPR line at $g = 4.3$.

Table 1.4: Characteristic g-values, peak-to-peak ΔH_{pp} width and aluminum hyperfine constant a of paramagnetic centers in irradiated Al_2O_3.

Center	g_x	g_y	g_z	a (mT)	ΔH_{pp} (mT)	Reference
F	2.0045				1.0	[49]
F*	2.0060				1.8-3.0	[45]
O^-	2.0155				4.3-5.0	[49-50]
O^-					4.3	[51, 50]
O^-	2.009				2.3	[52]
O^- or V_{Me}	2.0200				2.5-3.0	[45]
O^- or V_{Me}	2.0060				2.5-3.0	[45]
Al-O^--Al	2.0036	1.0				[49]
Al^{2+}	2.0200	1.9850		$a_{x,y}$=4.6 a_z=4.85		[49]
$Al^{3+}O^-$	2.0110				4.4	[53]
$[O^-Mg^{2+}]$	2.030	2.016	2.003			[47]
$[\boldsymbol{O^-Li^+}]^-$	2.023	2.014	2.003			[47]
V^{2-}	2.020	2.013	2.003			[47]
V_{OH}^-	2.0110	2.0180			4.5	[17]
V^{2-}	2.0130	2.0110			5.0	[17]
	$\lvert D \rvert$ (GHz)	**$\lvert E \rvert$ (GHz)**				
$[\boldsymbol{O^-Li^+}]$	3.05	0.8				[47]
$\boldsymbol{V^-}$	3.44	0.86				[47]

* Single electron trapped at an anion vacancy

1.5.3 F-center in hydroxides

F centers were detected in different hydroxides irradiated using X-ray at room temperature [50] and Gamma ray at 77 K.[54-55] They can be located in the bulk as well as on the surface. [50, 56] They have been identified in $Al(OH)_3$ and $Mg(OH)_2$ using EPR spectroscopy as a narrow singlet with a g factor of 2.002-2.004.[50, 54] In $Mg(OH)_2$ and

$Ca(OH)_2$ F centers can be formed due to localization of the electrons of the biographic vacancies[57] as well as in mechanically treated samples as demonstrated in $Al(OH)_3$.[54] Table 1.5 gives a summary of ESR parameters of F-centers identified in different hydroxides.

Table 1.5. Characteristic g-values, peak-to-peak width of F-centers in irradiated hydroxides.

gx	gy	gz	ΔHpp (mT)	Material	Reference
1.9919			0.6	$Sr(OH)_2$	[58]
2.0020				$Al(OH)_3$*	[54]
			0.14	$Al(OH)_3$	[50]
1.999				$Mg(OH)_2$	[56]
1.9998-				$Ca(OH)_2$	[56]
1.9807			2.0	$Ba(OH)2.7.4H_2O$	[59]
1.9807			2.0	$Ba(OH)2.1.7H_2O$	[59]
1.9807			2.0	$Ba(OH)_2$	[59]

* Hydrargillite

1.5.4 Hole centers in hydroxides

Hole centers in hydroxide are identified as O^-. Compared to oxide this center is unique because it is neutral in charge and does not require a charge compensator such cationic vacancy or impurities. Then it results in an unstrained lattice.

O^- identified in gamma irradiated hydrargillite $Al(OH)_3$ and Al_2O_3 at 77 K was shown to be located in the subsurface. Attributed g factors were respectively, g_{av}=2.016 ± 0.001 ($\Delta H_{1/2}$ = 5.3 mT) and g = 2.0122 (ΔH = 3 mT). O^- was also observed in X-ray irradiated $Al(OH)_3$ with a g factor of 2.0155 ± 0.001 ($\Delta H_{1/2}$ = 4.3- 5 mT).[50] O_3^- with g = 2.012 was encountered in irradiated $Al(OH)_3$. It was described to be formed as an interaction between O_2 adsorbed in vacancies with O^- ion-radical and shown to be stable up to 300 K.[54] Blaginina also observed oxygen anion defects related to Al^{3+} (Al^{3+} O^-) with a g factor of 2.011 (ΔH of 4.4 mT).[53] Two types of O^- were detected in irradiated $Al(OH)_3$ dried for 10 h at 433 K then sealed under vacuum in EPR tubes. The first one was seen to be trapped and stabilized in $Al(OH)_3$ and the second one exhibits a 11 lines spectra characteristic of a hyperfine interaction with the magnetic moments

of two Al^{3+} ions (I=5/2).[50] A third type can be described which is O^{2-} formed by the reaction between two O^-.[55]

The effect of vacuum, air and temperature on O^- ion-radicals was also studied and is shown in the case of Hydrargillite $Al(OH)_3$ irradiated at 77 K using γ-particles [54]. Different centers were formed depending on the atmosphere (air or vacuum) in which samples are irradiated and on the treatment received before irradiation. On increasing the dose and annealing, the nature of EPR spectra is difficult to be depicted since a superposition of several singlets belonging to O^- ion-radicals in various stabilized sites (for example in Al_2O_3 and $Al(OH)_3$) is observed.[56, 60]

Steinik and Barsova[54] observed no difference in concentration of paramagnetic centers between materials irradiated in vacuum and in air. They concluded that the centers are probably located in the bulk or subsurface layer.

The study of the accumulation of paramagnetic centers with respect to the dose could lead us to know whether intrinsic radiation centers are formed and the biographical defects existing before irradiation are filled by electron holes or not.

Conducting a study on Mg and Ca hydroxides, Barsova [56] shows that 2 centers could be formed after irradiation:

The first one formed at 77 K and 300 K and having a short spin lattice relaxation period that could be assigned to O^- ion-radical and that could be formed as following:

(15)

$$OH^- \rightarrow OH + e^-$$

(16)

$$OH^- + OH \rightarrow O^- + H_2O$$

(17)

$$OH^- \rightarrow O^- + H$$

The second is not formed in samples irradiated at 77 K and exposed to air and has a long spin-relaxation period (surface electron center).

Symons suggested that O^- is formed by deprotonation of OH radicals:[61]

(18)

$$OH + H_2O = H_3O^+ + O^-$$

The formation of O^-, O_2^- and O_3^- is also reported in $Sr(OH)_2$, $Ba(OH)_2$ and $Mg(OH)_2.7H_2O$.[58, 66]

Table 1.6 represents a summary of the major radiation induced defects explained above in different irradiated samples. g values are given as encountered in the literature.

Table 1.6. Characteristic g-values, peak-to-peak width and aluminum hyperfine constant of hole centers in irradiated hydroxides.

Center	gx	gy	gz	a (mT)	ΔHpp (mT)	Material	Reference
O^-	2.0759		2.0019			$Ca(OH)_2$	[46]
O^-	2.0480		2.0020			$Mg(OH)_2$	[56]
O^-	2.0754		2.0012			$Ca(OH)_2$	[56]
O^-	2.0468		2.0036			$Ba(OH)_2.7.4H_2O$	[59]
O^-	2.0810-2.0710					$Ba(OH)_2.7.4H_2O$	[59]
O^-	2.024-2.015		2.003			$Ba(OH)_2.1.7H_2O$	[59]
O^-	2.024-2.015		2.003			$Ba(OH)_2$	[59]
O^-	2.0122				3.0	Al_2O_3-$Al(OH)_3$	[54]
O^-	2.0674		2.0010			$Sr(OH)_2$ / $Sr(OH)_2.H_2O$	[58]
O^-	2.024-2.015		2.0030			$Ba(OH)_2$ / $Ba(OH)_2.1.7H_2O$	[58]
O^-	2.0170				4.0	$Al(OH)_3$	[52]
O^-					5.2	$Al(OH)_3$	[50]
O^-*	2.0620		2.0010			$Sr(OH)_2$ / $Sr(OH)_2.H_2O$	[58]
O^- *	2.0587		2.0010			$Sr(OH)_2$ / $Sr(OH)_2.H_2O$	[58]
O^- *	2.0556		2.0010			$Sr(OH)_2.7.4H_2O$	[58]
O_2^-	1.9664	1.9719	2.3101			$Ca(OH)_2$	[62]
O_2^-	2.0840		2.0010			$Sr(OH)_2.H_2O$	[58]
O_2^-	2.0510		2.0020			$Ba(OH)_2.7.4H_2O$	[63]
O_3^-	2.0170	2.0060	2.0010			$Sr(OH)_2$/ $Sr(OH)_2.H_2O$	[58]
O_3^-	2.0170	2.0080	2.0010			$Ba(OH)_2$/$Ba(OH)_2.1.7H_2O$/$Ba(OH)_2.7.4H_2O$	[63]
Al-O^--Al				a=1.03		$Al(OH)_3$	[50]

* near one or more H_2O

1.5.5 H radicals in hydroxides

In alkaline earth hydroxides irradiated with γ-rays at 77 K two symmetrical signals separated by 50 mT and having a width of 0.32-0.40 mT are observed in EPR spectra.[57, 64] This doublet was assigned to H radicals. These radicals were already seen in X-ray irradiated single crystals of hexagonal ice [65] and X-ray irradiated polycrystalline ice where they appeared at 4 K and disappeared above 60 K.[66]

Two types of H atoms were resumed in the case of alkaline earth elements described by Spitsyn et al.[57]

- A type formed by radiolysis of sorbed water (water crystallized) and are stabilized in tetragonal cavities between OH^- layers (A type has a hyperfine structure of 50.4 mT and $\Delta H_{1/2}$ = 0.36 mT).

- B type that appeared in thermally treated samples (B type has a hyperfine structure of 48.6 mT and $\Delta H_{1/2}$ = 0.34 mT).

ESR spectra of H radicals were also observed in γ-irradiated hydrargillite ($Al(OH_3)$ at 77 K [54] and in X-ray and γ -irradiated Bohemite, Gibbsite and Bayerite at 77 K.[64] Vedrine showed that disorder tends to reduce the thermal stability of H radicals.

Radiolytic yields of H radicals were resumed in Table 1.7. These yields were determined using EPR and are not frequently quantified.

Unlike others hydroxides some aluminum hydroxides were described to stabilize atomic hydrogen at room temperature and higher. For example, studying irradiated AlF3:OH and AlOOH with different irradiation sources (^{60}Co, X-ray, Hg-lamp and sunlight), Scholz et al observed atomic hydrogen up to a maximum temperature of 280ºC in AlF3:OH and to 150ºC in $Al(OH)_3$.[67] They suggested that the stabilization of H radicals requires the presence inside the matrix of symmetric host cages. As observed in the case of low temperature irradiated Boehmite, the yield of observable H radicals can be reduced by milling. It assumes that this treatment induces a cage deformation that prevents the stabilization of the H radicals and promotes their chemical reactions. Crystallographic shapes were shown to be important in the production of H_2, this could be due to the symmetry and several types of stabilization sites of atomic H.[57, 68]

To sum up, in order to form trapped H radicals, suitable precursors have to be present in the irradiated environment:[69]

- Impurities should be the minimum possible,
- Symmetrical local environment has to exist in order to prevent H atoms from leaving the cage-like structural units where H radicals are stabilized and prevent them from participating in chemical reactions.

Table 1.7. Radical hydrogen radiolytic yields found in literature Irradiated with ^{60}Co at 77 K.[57]

Material	G(H°) (10^{-7} mol/J)
$Mg(OH)_2$	0.14
$Ca(OH)_2$	0.22
$Sr(OH)_2.8H_2O$	0.10
$Sr(OH)_2$	0.083
$Ba(OH)_2.8H_2O$	0.21
$Ba(OH)_2$	0.10

1.5.6 Hydrogen production in hydroxides

As seen before, the radiolytic yield of molecular hydrogen depends on the form of water. Table 1.8 summarizes $G(H_2)$ in different hydroxides, some hydroxides may have a substantial contribution to H_2 formation. Moreover the type of anionic metal forming hydroxide affects the production of H_2.

Westbrook and al studied the molecular hydrogen production from Boehmite AlOOH and Bayerite and Gibbsite $Al(OH)_3$ under Gamma irradiation. Interestingly, they noticed no molecular hydrogen production from $Al(OH)_3$ containing more radiolysable sites. In order to interprete their result, they used density functional theory (DFT) and explained that the removal of a hydrogen atom is energetically more favorable from Boehmite than from Gibbsite (Estimated energy barrier for H atom loss from Boehmite was supposed to be 7.3 eV and for Gibbsite 7.9 eV). Also the estimated energy for molecular hydrogen removal was higher in the case of Gibbsite (6.46 eV) than in Boehmite (4.2 eV) which can explain the higher radiolytic yield in the latter case.

Table 1.8. Molecular hydrogen radiolytic yields found in literature. Values in parentheses represent the total hydrogen released after dissolution.

***Baked at 100°C for 24 hours. Specific surface area not specified.**

**** 1.3310^{-8} bar 200°C ($Ba(OH)_2$) 130°C ($Sr(OH)_2$). Specific surface area: 0.5-1.5 m^2/g**

***** Baked at 60°C for 24 hours. Particle size 45-63 µm.**

Material	Irradiation	$G(H_2)$ (10^{-7} mol/J)	Reference
$Ca(OH)_2$*	^{60}Co	0.21	70
$Ca(OH)_2$*	He 5 MeV	0.051	
$Mg(OH)_2$*	^{60}Co	0.053	
$Mg(OH)_2$*	He 5 MeV	0.038	
$Sr(OH)_2$**	^{60}Co	0.13 (0.20)	58
$Sr(OH)_2$ H_2O**		0.042 (0.10)	
$Sr(OH)_2$ 7.4 H_2O**		0.031 (0.05)	
$Ba(OH)_2$**		0.073 (0.083)	
$Ba(OH)_2$ H_2O**		0.093 (0.21)	
$Ba(OH)_2$ 7.4 H_2O**		0.052 (0.072)	
AlO(OH)***	^{60}Co	0.057-0.13	6
$Al(OH)_3$***		0	

1.6 Conclusion

A general overview of radiation interaction with matter was presented. In insulators such as oxide and hydroxide, many point defects and color centers are created either by elastic collision or electronic excitation. The presence of water at the surface or inside the structure induces the production of molecular hydrogen. The radiolysis of water depends on the solid and on the bonding between water molecules and solids or on the bonding of water molecules themselves.

In solids unlike the radiolysis of liquid water, energy transfers via exciton or charge carriers play a major role in the modification induced by radiation. These processes are complex, therefore they were only relatively well documented for a limited number of materials. As seen in the literature review above, radiolytic yields of molecular hydrogen are available for some hydroxides but the effect of many factors encountered in practice (as nuclear waste assemblies, for example) such as specific surface area, nanometric particle size, impurities, temperature, structural and adsorbed water has not been specifically studied.

The aim of the work presented in the following sections is to contribute toward clarification of the impact of particle size and impurity on the production of molecular hydrogen in aluminum and magnesium hydroxide and in aluminum oxyhydroxide. We also payed special attention to study the contribution of structural and adsorbed water.

The primary ambition of this study was to clarify the mechanism of formation of hydrogen from structural water encountered in hydroxide. Since many questions remain unanswered, we tried to discuss the following ones:

What are the precursors of molecular hydrogen in hydroxides and oxyhydroxides?

Are hydrogen atoms the only precursors?

What are the main transformations related to the production of H_2 and how do defects interfere in the production of molecular H_2?

Molecular hydrogen production with respect to many physical parameters will be presented. Detailed EPR studies will be exposed in order to try to characterize the defects associated with molecular hydrogen. A simulation to other hydroxides could be done using conclusions drawn from AlOOH and $Al(OH)_3$

2. Chapter 2: Facilities, equipment and techniques

In this chapter, chemicals, radiation sources and analytical techniques employed in this project are described. Drying optimization as well as hydration of AlOOH L and $Al(OH)_3$ and $Mg(OH)_2$ synthesis are represented.

Structure and radiation induced defects characterization are listed as well as gas analysis.

2.1 $Al(OH)_3$ and AlOOH

The main investigation was led on granular powders of oxyhydroxides AlOOH (Boehmite) and hydroxides $Al(OH)_3$ (Bayerite). In order to ensure reproducibility all samples were taken from the same batch procured from Sasol, Germany.

AlOOH was studied in two different crystallite sizes, while one particle size was investigated in the case of $Al(OH)_3$. Large particle size and small particle size will be denoted AlOOH L and AlOOH S respectively.

2.1.1 Drying optimization

Samples placed in glass ampules were dried by heating the powder using a Carbolite tube furnace under high vacuum conditions (10^{-4} mbar). Before defining the suitable temperature adopted, temperature and heating duration were determined. Drying was optimized using the thermogravimetric analysis (TGA) in order to determine the amount of water present in the samples and to be sure that structural water was not affected by heat treatment.

Drying conditions were optimized considering the weight loss between 20˚C and the temperature of the first Derivative thermogravimetric curve (DTG) peak due to the loss of non-chemically bound water (physisorbed water). Care was taken not to exceed the temperatures higher than that of the DTG peak due to complete dehydration of the structure corresponding to Al_2O_3 formation. Related transition temperatures are 350°C for $Al(OH)_3$ and 450°C for AlOOH,[71] though it was proved that thermal decomposition could occur at 200°C under secondary vacuum,[72] therefore this limit was not exceeded while preparing our samples.

The optimum conditions adopted were 170°C during 5 hours for AlOOH and 130°C during 4 hours for $Al(OH)_3$.

AlOOH S has to be evacuated very slowly before starting heat treatment. Two hours were needed to evacuate the sample by gradually diminishing the pressure without letting the powder spread all over the ampule and joints.

2.1.2 Hydration

In this study, samples were placed into desiccators, which contain various saturated salt solutions to generate desired levels of relative humidity, denoted as RH, Water uptake was evaluated by weighing each sample periodically.

Lithium chloride purchased from Sigma Aldrich with a reference number 746460-100G, Potassium carbonate purchased from Sigma Aldrich with a reference number 791776-100G and Sodium chloride purchased from Sigma Aldrich with a reference number S9625-500G were used in order to obtain a RH of 11, 44 and 74 % at room temperature consequently.[73-74] The weight of each sample was determined periodically. Each saturated salt solution was prepared by adding salt to warm (about 40°C) distilled water and stirring until having a supersaturated solution. The last-mentioned element is then cooled to ambient temperature and allowed to set for at least 24 hours before use. All salt crystals should be covered by the solution.

In order to avoid the exposition of samples to air and avoid the rebalance of water uptake, some materials were placed in Pyrex ampules connected to another ampules containing a salt solution. These experiments will serve to give an error bar range.

Water layers

In order to understand how much water is adsorbed on each sample surface when applying a certain relative humidity, we introduced water layers, this is important to understand if molecular hydrogen produced comes only from adsorbed water.

In PuO_2 oxide, it was supposed that the average area of a water molecule is 0.22 mg/m^2 and the number of water layers can be determined as explained below. [75]

For instance, at 11% imposed relative humidity, AlOOH L adsorbs 0.6 g of water/100 g AlOOH L. Having a specific surface area of 40 m^2/g, this sample adsorbs a fraction of 0.66 water layer:

(19)

$$\frac{\mathbf{0.6 g H_2O}}{\mathbf{100 g AlOOH \times 41 \frac{m^2}{g} AlOOH \times 0.00022 \frac{g}{m^2} H_2O}}$$

In our calculations, the value supposed by Livingston as the average area of a water molecule is 0.28 mg/m^2 is going to be used deduced from the cross-sectional areas of water on over twenty non porous adsorbate systems similar to that used in our study.
The previous equation resumes water layers formed in each hydrated case and is needed to deduce the radiolytic yield of the adsorbed water deduced by energy received by the fraction of water only and not by all the system. The amount of water is difficult to be measured accurately. Error bars were introduced (10, 4 and 3% for AlOOH L, AlOOH S and $Al(OH)_3$ consequently) by considering the minimum and maximum value in each case.

2.2 $Mg(OH)_2$

2.2.1 Sample preparation

In order to study the effect of impurity and smaller particle-size (3 nm) on molecular hydrogen production, $Mg(OH)_2$ was prepared using a simple one-step synthesis following Sutto method.[76] Nanoparticles of $Mg(OH)_2$ were prepared using potassium superoxide (KO_2) purchased from Sigma Aldrich with a reference number 278904 50G, magnesium sulfate ($MgSO_4$) from Sigma Aldrich with a reference number 63136 1KG F and methanol purchased from Sigma Aldrich with a reference number 34860-1L-R. In order to vary the impurity, magnesium nitrate hexahydrate ($Mg(NO_3)_2.6H_2O$) was used instead of $MgSO_4$ and was bought from Suprapur Merck Gemany with a reference number 5855.
Among the different syntheses performed only 3 will be chosen to study the molecular H_2 production with respect to impurity. The difference between the three chosen syntheses is clarified as follows:

- The first synthesis (represented by violet color henceforth) is prepared by adding $MgSO_4$, KO_2 and methanol and waiting for complete dissolution in order to minimize particle size, the suspension was centrifuged at 10 000 min^{-1} and washed with distilled water (8 times, 30 min/centrifugation at 20°C). Before use, this test was oven-dried at 60°C for a weekend. **This sample has 18% K_2SO_4 as impurity amount.**
- The second synthesis (represented by orange color henceforth) was conducted in the same way as the first synthesis but suspension was washed 11 times and freeze-dried for one night. **This sample has 1% K_2SO_4 as impurity amount.**

- The third synthesis (represented by olive color henceforth) where ($Mg(NO_3)_2.6H_2O$) was added instead of $MgSO_4$ and suspension was oven-dried at 60°C after 7 rinses with distilled water and 2 rinses with methanol. **This sample has 7% KNO_3 as impurity amount.**

Synthesized tests will be compared to a commercial $Mg(OH)_2$ purchased from Nanostructured and Amorphous Materials, Los Alamos **pure at 98%**. This reference sample has a 19 nm particle size.

2.3 Irradiation Experiments

2.3.1 Radiation sources

2.3.1.1 The linear accelerator LINAC

Irradiations were performed using the electron pulses of a Titan Beta, Inc. linear accelerator (Laboratoire Interdisciplinaire sur l'Organisation Nanométrique et Supramoléculaire LIONS, CEA Saclay, France). Electrons of 10 MeV with a pulse length of 10 ns were used. All experiments were done at a pulse frequency of 5 Hz. Only one test at 1 Hz was done in order to verify that samples were not heated during irradiation.

Glass ampules containing the materials were directly placed in front of the window from where electron beam goes out.

2.3.2 Gamma source Cesium-137

In this study, Gamma irradiations were carried out by gamma-rays from Cs-137 source (Nordion Gammacell®, LIONS, CEA Saclay, France). The Gammacell is well shielded and encased in welded steel. The cesium-137 source material is in the form of 137CsCI, its activity is 50 TBq approximatively. It is contained in a stainless steel tube as seen in Figure 2.1. This tube is placed next to the irradiation chamber that contains a canister in which 6 10 cc-ampules can be placed in cylindrical holder. The canister is placed on a rotating plate, once irradiation starts, the samples turn around the source in order to ensure dose uniformity.

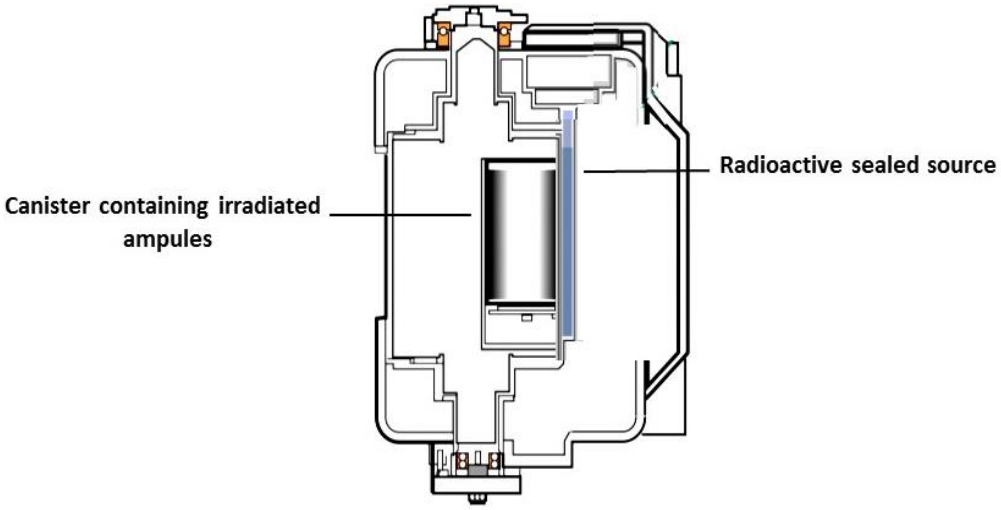

Figure 2.1. Scheme of a Gammacell 3000 in irradiation position. The Cs-137 radioactive source is in the vicinity of samples contained in a canister.

2.3.3 Heavy ion irradiation

Samples placed in thin wall Pyrex ampules (4 mm diameter and 0.38 mm thickness) were irradiated using heavy ions at GANIL (Grand Accélérateur National d'Ions Lourds, Caen, France) in the IRRABAT chamber. During irradiation the chamber was under vacuum and the temperature of the samples was comprised between 20 and 25°C. The ions used in these experiments were $^{36}Ar^{18+}$ at 95 MeV/nucleon (i.e. 3 GeV) The samples were irradiated at two fluences: 1.25-1.30 10^{12} and 2.6-2.63 10^{12} ions.cm^{-2}and the flux was 3-4 10^{8} ions.cm^{-2}.s^{-1}. The approximate water equivalent doses corresponding to these fluences are 500 and 1000 kGy respectively. The deposited energy in the materials and mean LET values were evaluated using SRIM program.[10] The calculation considers the thickness of the irradiation window and a cylindrical geometry (see Figure 2.2). The LET values were estimated to 709-762 eV/nm for $Al(OH)_3$, 837-864 eV/nm for AlOOH L and 864-894 eV/nm for AlOOH S.

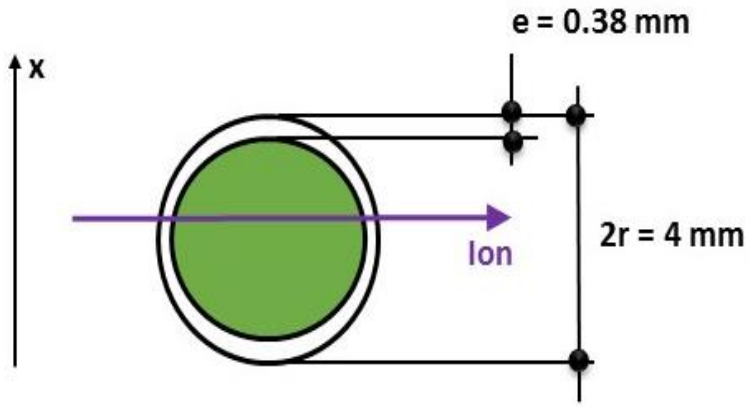

Figure 2.2. Used geometry to calculate the received dose. The diameter of the bottom of the ampule was 4 mm and 0.38 mm the glass thickness.

2.3.4 Dosimetry

Fricke dosimeter,[77-78] was used to determine the dose rate delivered by the Gammacell and was around 5.3 Gy/min.

The same dosimeter was used to measure the dose delivered per pulse from the LINAC. It was comprised between 20 and 30 Gy/pulse.

The difference between water and the irradiated materials are expected to be minimal.

The Fricke solution was prepared using chemicals of high purity, including ammonium iron (II) sulfate hexahydrate ($(NH_4)_2\,Fe(SO_4)_2 \cdot 6H_2O$) purchased from Labosi-Analypur with a reference number A 3045, sodium chloride (NaCl) purchased from Sigma Aldrich with a reference number S9625-500G, and sulfuric acid (H_2SO_4) purchased from Sigma Aldrich with a reference number 258105-2.5L, using a 1 L volumetric flask. First, 22 ml of sulfuric acid [H_2SO_4] (95.0–99.0%) was diluted with 250 ml of Milli-Q water, and then 0.06 g sodium chloride, and 0.392 g of ferrous sulfate were added. The solution was added to the volumetric flask and diluted to the final volume of 1 L with Milli-Q water. The flask containing the Fricke solution was sealed and stored away from natural and artificial light sources for 24 h before use. Sodium chloride should be used in order to suppress the effect of organic impurities in the solutions.

When irradiated, ferrous sulfate solutions first give water decomposition to give free radicals (H, OH) and molecular products (H_2, H_2O_2):

(20)

$$H_2O + radiation \rightarrow H, OH, H_2, H_2O_2$$

Then the following series of reactions occur: [79-80]

(21)

$$H + O_2 \rightarrow HO_2$$

(22)

$$OH + Fe^{2+} \rightarrow Fe^{3+} + OH^-$$

(23)

$$HO_2 + Fe^{2+} \rightarrow Fe^{3+} + HO_2^-$$

(24)

$$HO_2^- + H^+ \rightarrow H_2O_2$$

(25)

$$H_2O_2 + Fe^{2+} \rightarrow Fe^{3+} + OH + OH^-$$

(26)

$$H + Fe^{2+} \xrightarrow{H+} Fe^{3+} + H_2$$

According to the reactions represented above
$G(Fe^{3+}) = 2G(H_2O_2) + 3G(H^{\circ}) + G(HO) = 15.6\, molecules/100$ eV around 25˚C. As seen below, ionizing radiation converts ferrous ions, $Fe^{2+,}$ into ferric ions, Fe^{3+}, with a known radiation yield. The production of the Ferric ions (Fe^{3+}) was followed using a UV-Vis spectrometer Shimadzu UV-2550 located in the LIONS, CEA-Saclay, France. Then the absorbed dose to the Fricke solution, DF, is:

$$DF = \frac{OD}{\varepsilon G(Fe^{3+})\rho l}$$

Where OD is the increase in optical density at 303 nm and ε is the extinction coefficient of Fe^{3+} at 303 nm minus the extinction coefficient of Fe^{2+} at the same wavelength. We use a value of 20205 M^{-1} cm^{-1} for ε. $G(Fe^{3+})$ is the radiation yield of Fe^{3+}, ρ is the density of the Fricke solution and l is the length of the light path of the cell.[78, 81] Hence, a correction for fading was not considered. The colorimetric dose response is linear up to 400 Gy.[82] Figure 2.3 presents an example of Fricke dosimetry curve. Error bars are considered as 15%.

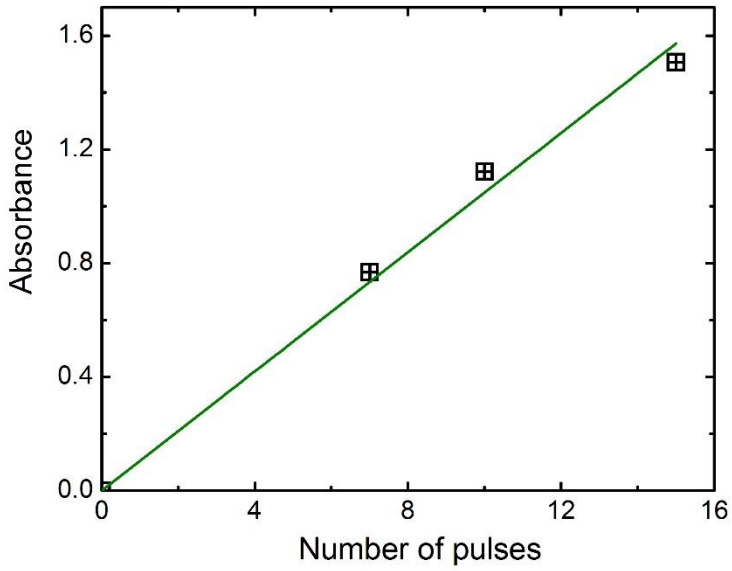

Figure 2.3. Fricke dosimetry curve showing the variation of absorbance with respect to pulse number delivered by the LINAC.

Fricke dosimetry was verified by using thiocyanate dosimetry.

The SCN^- ions contained in a solution of potassium thiocyanate (KSCN) react with OH radicals and produce $(SCN)_2^-$ ions:

(27)

$$OH + SCN^- \rightarrow OH^- + SCN^\circ$$

(28)

$$SCN^\circ + SCN^- \rightarrow (SCN)_2^-$$

The $(SCN)_2^-$ ions are quantified using optical adsorption at 475 nm.

The dosimetry is usually made in 0.01 mol dm^{-3} air or oxygen-saturated solution. The dose is calculated from $D = G\varepsilon l\rho$ using absorbance at 475 nm and $G\varepsilon$= 2.6x10^{-4} m^2J^{-1} where ε is the extinction coefficient at 475 nm, l is the light path in the optical cell and ρ is the density.[83]

L-α–alanine EPR dosimetry was used in order to determine the dose delivered in the EPR tubes and Dewars irradiated with electron beams (see section 2.3.5.1). Alanine pellets bought from Sigma Aldrich were placed in the EPR tubes and the height of alanine column was enough to cover the whole active region of the microwave cavity in the EPR spectrometer. After irradiation, L-α–alanine amino acid (CH_3-$CH(NH_2)$-COOH) is deaminated and produces a stable alkyl free radical, CH3C•HCOO. The concentration of these radicals is proportional to the absorbed dose over a wide range

of doses (1–105 Gy) and can be estimated quantitatively using the EPR spectrometry.[84, 85-86]

2.3.5 Radiation vessels

2.3.5.1 Vessels used to measure H_2 production

Sample vessels dedicated to evaluate molecular hydrogen produced and radiation induced defects are described in this section. For a better comprehension these vessels were drawn and shown below.

Most of the samples irradiated using electron beam dedicated to analyze molecular H_2 were placed in 10 mL Pyrex ampules with valves as seen in Figure 2.4. It was easy to use the same ampule for many irradiations by removing the valve and introducing the powder. Only the bottom of the ampule was irradiated and was conceived to have a spherical homogeneous shape. The preliminary washing of the ampules was optimized in order to reduce as far as possible the hydrogen production of the empty ampules.

Ampules washing procedure:

A solution of nitric acid 2M was prepared. Small magnetic stir-bars made of Teflon were used in each ampule containing nitric acid in order to stir all night long at 70°C. The next day, ampules were rinsed with acidic solutions by gradually decreasing their concentrations in order to avoid any glass attack. Ampules were then rinsed and filled with distilled water and left at 70°C for one night. In the morning, they were oven-dried at 120°C. The ampules were then placed in the oven at 350°C in order to regenerate the glass. By using this protocol, H_2 produced from empty irradiated ampules greatly improved from 40 ppm to 4-5 ppm for the same dose using electron beam irradiation.

Figure 2.4. Pyrex ampule equipped with a valve used to analyze hydrated samples irradiated using electron beams and that used for annealing. Longneck ampules were used in order to keep the rubber seal attached to the valve clean and maintain the vessel leak proof.

These ampules with a valve were especially dedicated for hydrated samples and for annealing experiments since many analyses were needed and it is possible to open the valve and insert samples as many times as we want.

Though, dry samples were irradiated in ampules able to be sealed to maintain airtight integrity since low quantities of H_2 are released and sometimes gas could not directly be analyzed after irradiation (see Figure 2.5). These ampules having a volume of 20 ml were used for Gamma analyses where irradiation is homogenous and only glass and powder were irradiated. Ampules used in Figure 2.5 were also used for dry samples irradiated with electron beams since low H_2 quantities were released. These ampules have an aperture side where we can introduce the sample and gas (pure Helium) and another sealed one that permits the gas analysis. This side looks like a pig tail (Figure 2.5, right), it was connected to the chromatography and once the desired vacuum is achieved, the tail was broken and released gas was analyzed.

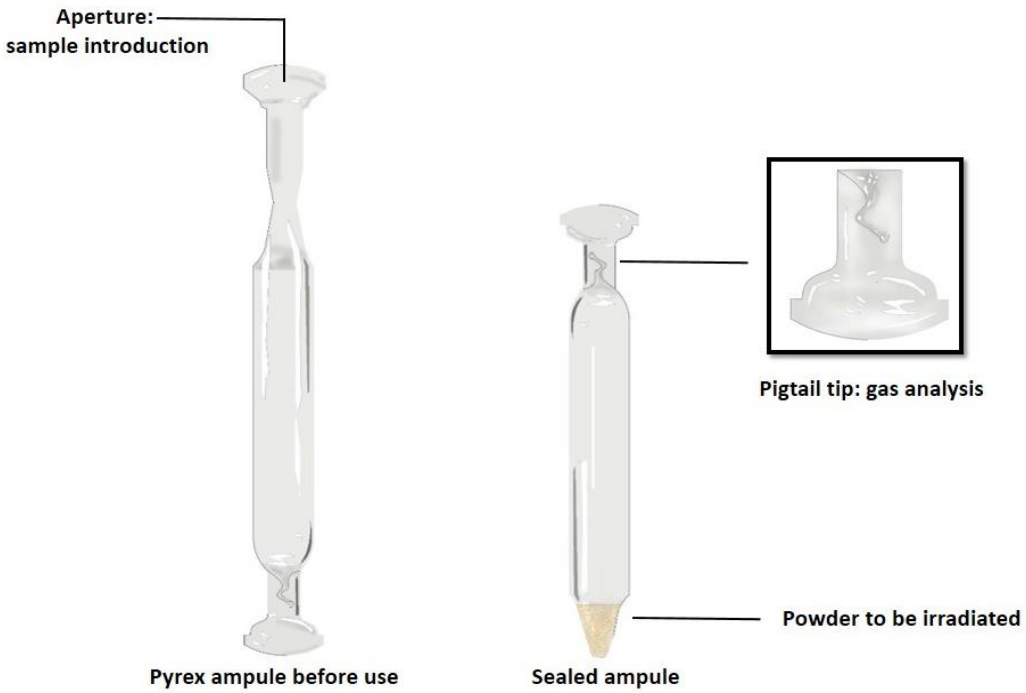

Figure 2.5. Pyrex ampules equipped with a pigtail used to analyze dry electron beam irradiated samples and all Gamma irradiated samples. The aperture from one side facilitates the introduction of the sample and gas (left). Ampules are then sealed, powder is irradiated and gas is analyzed by breaking the pigtail (right).

Ampules used for heavy ions irradiations were conceived to be airtight, as seen in Figure 2.6. They were sealed and have a volume of 6 cm^3 after sealing. These sealed ampules, as seen in the previous ampule, have a pigtail that needs to be broken in order to analyze the gas that is released after irradiation. This ampule was conceived for heavy ions with a bottom diameter of 4 mm and a glass thickness of 0.5 mm. Only the bottom containing the powder was irradiated and was conceived thinner in order to avoid important beam attenuation caused by the glass. Helium gas was used as a pure gas to fill the ampules before sealing.

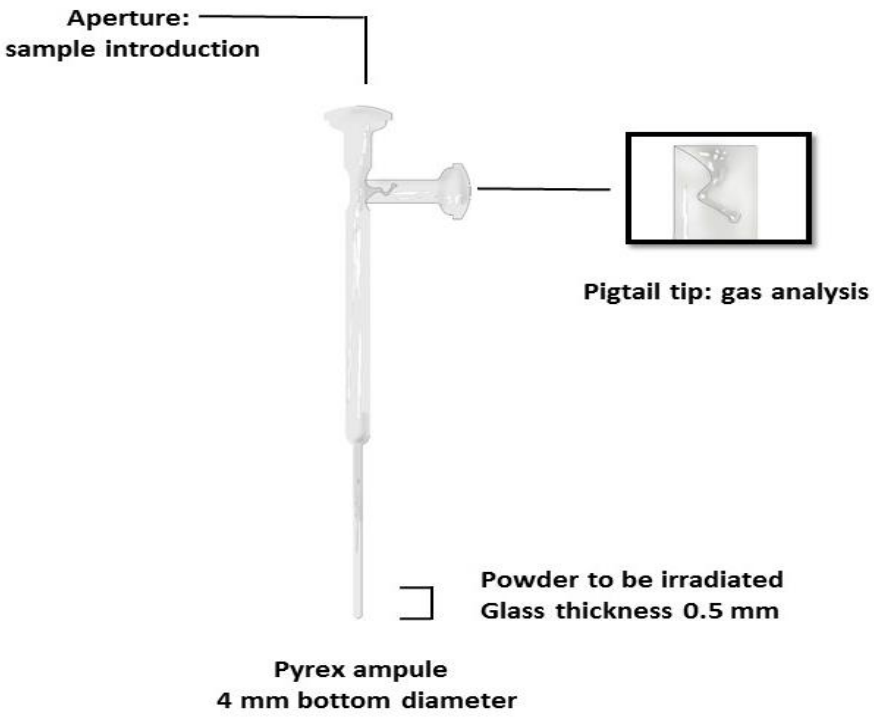

Figure 2.6. Pyrex ampules equipped with a pigtail used to analyze samples irradiated using heavy ions. The aperture from one side facilitates the introduction of the sample and gas (left). The bottom is 4 mm diameter tube. Ampules are then sealed, powder is irradiated and gas is analyzed by breaking the pigtail (zoom on the right).

2.3.5.2 Vessels used for EPR analysis

Concerning samples dedicated to EPR analysis, Room temperature EPR sample cells were standard NMR tubes evacuated and flame-sealed. Though, samples dedicated to low temperature EPR, also irradiated at low temperature were irradiated in EPR cold finger quartz Dewar Figure 2.7. Samples irradiated for low temperature EPR were made into pellets. It was essential in order to irradiate in the same vessel and analyze by EPR without creating irradiation defects in the zone analyzed by the EPR. The pellet is irradiated while it is hanged to the wire and once irradiated it is released to the bottom of the where it is supposed to be analyzed by EPR.

Dewars are filled with liquid nitrogen in order to keep the samples irradiated at 77 K.

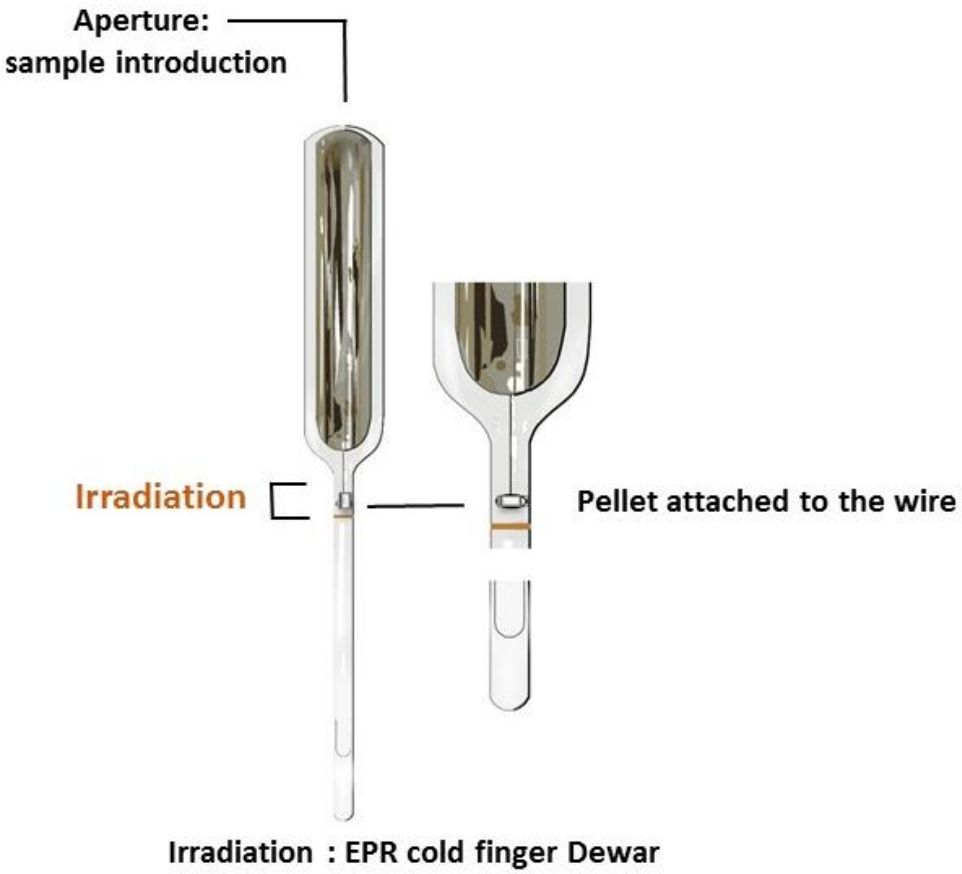

Figure 2.7. EPR cold finger Dewar used to analyze irradiated pellets at low temperature. The sample is introduced attached to a metallic wire (left) and is then irradiated at the top of the thin quartz tube. After irradiation the pellet is released to the bottom of the Dewar in order to be analyzed by EPR.

2.3.5.3 Annealing experiments vessels

In order to quantify the release of molecular hydrogen trapped after irradiation, detrapping experiments were conducted using dissolution or annealing. A scheme of the ampule used is described in Figure 2.8.

Dissolution ampules were made conic-like from the bottom in order to irradiate the minimum possible quantity and to be able to dissolve it without wasting many days since dissolution was hard even when finding the suitable dissolvent.

Figure 2.8. Conic-like Pyrex ampules equipped with a J Young valve that resists to acidic and basic attack used to analyze gas released from dissolved irradiated samples.

Annealing experiments serving for the quantification of molecular hydrogen released from the structure were done at different temperatures using the same ampules described in Figure 2.4.

As seen in Figure 2.9, a first ampule containing irradiated powder was attached to another one that serves as a water trap. Glass balls are inserted in the water trap ampule in order to increase the specific surface of water adsorption. The ampules are connected with a glass connection under vacuum. Annealing was done from 40°C to 250°C (40°C/hour) and at 500°C for 120 minutes in the case of AlOOH L and S and at 400°C for 90 minutes in the case of $Al(OH)_3$. Annealing experiments were conducted until complete dehydration of the materials that leads to the formation of Al_2O_3 in order to release all the gas that may be trapped inside the structure.

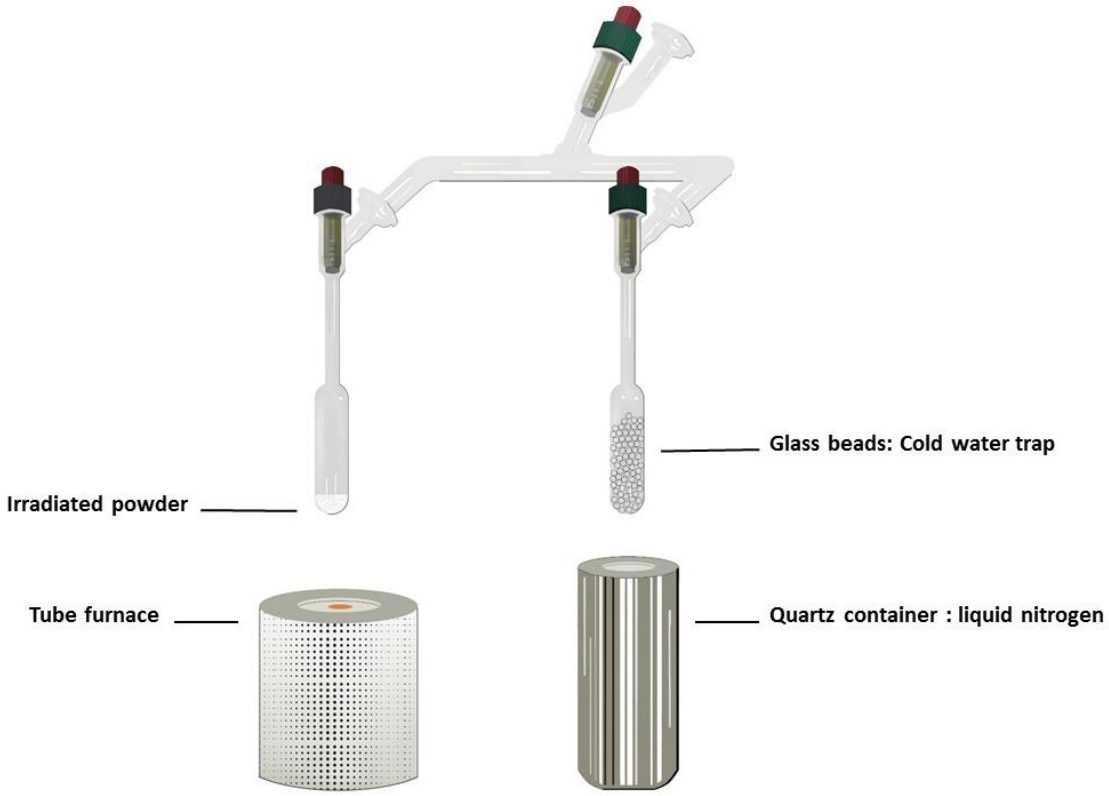

Figure 2.9. Annealing system consisting of the evacuated irradiated ampule (left) heated with a tube furnace until transition temperature is attended and connected to another ampule under vacuum (right). This latter is cooled using liquid nitrogen in order to trap water and adsorb it on the glass beads inside.

2.4 Characterization before and after irradiation

2.4.1 X-ray Crystallography (XRD)

X-Ray diffraction (XRD) was used for three main purposes: phase identification, crystallite size estimation and comparison before and after irradiation.

X-Ray Diffraction was performed at the Laboratoire Archéomatériaux et Prévision de l'Altération (LAPA) CEA-Saclay, France. Material structures were investigated using a photon microprobe, built on a Rigaku RU 200 rotating anode X-ray generator running at 55 kV and 21 mA. The beam delivered by a molybdenum anode (Kα ~ 17.45 keV - 0.070 nm) was monochromatized by a toroidal multilayer mirror and then focused on a surface of 100 100 μm^2 with an average flux of 20.106 ph/s. Diffraction patterns were collected in transmission mode with an image plate (GE Healthcare), and then circularly integrated with FIT2D (ESRF). Data processing was carried out with the EVA software (Bruker AXS) and the ICDD-JCPDS database.

In order to estimate the crystallite size D (Å), Scherrer equation was used:[87]

(29)

$$\boldsymbol{D = \frac{K\lambda}{\beta cos\theta}}$$

Where K is the Scherrer constant, λ is the wavelength of X-radiation (λ_{Mo}= 0.707 cm), θ the diffraction angle (degree), β is the X-ray diffraction broadening (radian).

In order to determine the X-ray diffraction broadening (β) that is the width of a powder diffraction considering the broadening due to the experimental equipment, a 5 microns alumina is used to determine the instrumental broadening. β is then determined from Warren's formula:

(30)

$$\beta = \sqrt{B_m^2 + B_S^2}$$

Where B_m is the measured peak width at half peak height (radian) and B_S the one of the standard material used which is alumina here.

Crystallite size is inversely related to the full width at half maximum of an individual peak: the narrower the peak, the larger the crystallite size. This is due to the periodicity of the individual crystallite domains, in phase, reinforcing the diffraction of the X-ray beam, resulting in a tall narrow peak. If the crystals are defect free and periodically arranged, the X-ray beam is diffracted to the same angle even through multiple layers of the specimen. If the crystals are randomly arranged, or have low degrees of periodicity, the result is a broader peak.

2.4.2 Infrared spectroscopy (IR)

In order to determine disorder and functional groups, Fourier transform infrared spectroscopy (FTIR) was performed on a Bruker Tensor 27 FTIR spectrophotometer using the ATR (attenuated total reflectance) technique with a Golden Gate accessory at LIONS, CEA-Saclay, France. Spectra were collected over the range of 4000-500 cm^{-1} at a 4 cm^{-1} resolution from 100 scans. Data were analyzed using OPUS software.

2.4.3 Raman spectroscopy

The Raman spectrometer was done at LAPA, CEA-Saclay, France. It is an Invia reflex from the Renishaw Company equipped with a frequency-doubled Nd: YAG laser emitting at 532 nm and a solid state laser emitting at 473 nm. The laser beam is focused

on the sample through an optical microscope with a 50X LEICA objective, the spectral resolution achievable by the CCD detector is around 2 cm $^{-1}$. Laser spot size on the samples is less than 2 µm. Spectra were recorded between 200 and 4000 cm^{-1} with a 2400 l/mm grating. Thanks to a motorized stage mapping, acquisitions can be collected. The hyper spectral images obtained provide fruitful information on the localization of various crystalline phases constituting the observed systems.

2.4.4 Scanning electron microscopy (SEM)

The morphology and topography of nanoparticles were recorded using a scanning electron microscopy (SEM) at LAPA, CEA-Saclay, France equipped with a Field Emission Gun (FEG) type JEOL (JSM-7001F). Power and voltage were adjusted in order to attend a spatial resolution of a few nm. Powders were placed in aluminum support that we engraved in order to keep the powder stuck in the engraved holes. This step was essential in order to avoid using carbon support films where we noticed a disturbing charge accumulation on the surface of the powder. Samples were therefore metallized with a carbon coater before observation in the scanning electron microscope.

2.4.5 Brunauer, Emmett and Teller analysis (BET)

The specific surface areas, noted BET-SSA, were calculated using Brunauer Emmett Teller (BET) method where adsorption point P/P0 ranged between 0.06 and 0.2. This analysis was done in collaboration with Romain Dagneli.

Adsorption-desorption isotherms with nitrogen were collected on a Micrometrics (ASAP 2010 Instrument) apparatus at 77 K at the Laboratoire de Mesures et Modélisation de la Migration des Radionucléides (L3MR), CEA-Saclay, France. Samples were prepared by drying 1 g of each material under vacuum at 90°C for 1 h followed at 105°C for 2 h to ensure a complete moisture desorption before analysis. Pore size distribution was obtained using a Barrett Joyner Halenda (BJH) model on the desorption isotherm.

2.4.6 Thermogravimetric analysis (TGA)

Thermogravimetric measurements were performed with a Mettler-Toledo TGA/DSC at LIONS, CEA-Saclay, France. The samples (approximately 30 mg) were placed in alumina crucibles and heated from 20 to 1000 °C (at 10 °C/min) under a nitrogen flux of 50 mL/min. The data was analyzed using STARe software.

Sorption and desorption under conditions of defined relative humidity were also conducted using a humidity generator HumiSys (low flow) (InstruQuest, Boca Raton, FL, USA) coupled to the TGA. This RH generator is designed to inject humidity into the sample chamber by means of a heated transfer line, with a maximum flow rate of 5 L/min. The RH is controlled inside the sample chamber using temperature and humidity sensors placed inside the chamber, a few centimeters from the sample.

The relative humidity is measured using a RH sensor (Vaisala HMT337) with an accuracy, including hysteresis, non-linearity and repeatability, of ±1% RH on the range 1–100% RH and for a temperature between 15 and 25 °C. Each 10% RH step was imposed for 1 hour.

2.4.7 Electron paramagnetic resonance magnetometer (EPR)

In order to detect the defects induced after irradiation, Electron paramagnetic resonance (EPR) was conducted at *Labora*toire National Henri Becquerel (LNHB), CEA-Saclay, France and Laboratoire des solides irradies (LSI), Ecole Polytechnique, France. Spectra were acquired on an X-Band EMX Bruker spectrometer (X-Band) with a 100 kHz field modulation. In most case microwave power and amplitude modulation were 10 mW, a 1 Gauss, respectively. The microwave frequency was measured with a frequency counter. Quantification was estimated using a hydroxyl-TEMPO sample as a standard. The error on the conversion factor is estimated at 25%. A cold finger Dewar was used for measurements at 77 K.

The principle of EPR spectroscopy is presented briefly in the following.[88]

As a result of the Zeeman Effect, the state energy difference of an electron with S=1/2 in magnetic field H_0 is:

$$\Delta E = g\mu_B H_0 \quad \textbf{(31)}$$

Where μ_B is the Bohr magneton and g the gyromagnetic factor which is 2.0023 for free electron and H_0 the magnetic field. To induce transition between the energy levels, the electron should absorb a quanta of energy $h\upsilon$ (h is Planck's constant). Then, the preceding equation is expressed as:

$$h\upsilon = g\mu_B H_0 \quad \textbf{(32)}$$

Then g value is given below:

(33)

$$g = \frac{71.4484 \cdot \upsilon\ (GHz)}{H_0\ (mT)}$$

The g-factor of the paramagnetic center is sensitive to its constituting atoms due to spin-orbit coupling. In most cases, it is a tensor that mirrors the electronic structure of the paramagnetic center resulting from the interaction of crystal field with orbitals.

In the general case, if we suppose that axes x, y and z are the principal directions of the g-tensor and the corresponding g-factor principal values are g_x, g_y and g_z, g can be written as followed:

(34)

$$g^2 = g_x^2 sin^2\theta cos^2\varphi + g_y^2 sin^2\theta cos^2\varphi + g_z^2 sin^2\theta cos^2\varphi$$

θ and ϕ are the polar angles of the field direction with respect to the coordinate system of theprincipal directions of the g-tensor principal values.

Single crystals analyses are often needed to determine the relation between g-factor principal values and the crystallographic or molecular axes.

In randomly oriented samples numerical simulations of EPR spectra are needed to determine the g-factor principal values.

Another source of information on paramagnetic center can be the hyperfine structure that results from the magnetic interaction between the unpaired electron and the nuclear spins.

Two kinds of hyperfine interactions exist:

- *Fermi-contact interaction* when the electron density is non-zero at the nucleus X. This magnetic interaction gives rise to a isotropic hyperfine coupling a_X that is proportional to the unpaired electron density at the nucleus,
- *Dipolar hyperfine interaction* which represents the interaction between the magnetic moments of the electron and of the nucleus. The corresponding hyperfine coupling is a strongly anisotropic traceless tensor. In practice this interaction is weak and rarely resolved except in single crystals.

Each nucleus X with a nuclear spin I splits the line into equidistant $2I + 1$ lines. n non-equivalent nuclei give rise to $(2I + 1)^n$ lines while n equivalent nuclei give rise to $2nI + 1$ lines whose intensities distribution is calculated using Pascal's triangle.

2.4.8 Inductively coupled plasma atomic emission spectrometry (ICP AES)

Inductively coupled plasma atomic emission spectroscopy (ICP-AES) also referred to as inductively coupled plasma optical emission spectrometry (ICP-OES), was used for the detection of trace metals.

ICP-AES (Perkin Elmer Optima 2000 DV) at Laboratoire d'Intégration de Systèmes et des technologies (LISL), CEA-Saclay, France, served to determine the elementary composition of studied samples. Argon gas was used to create the plasma, and SPEX solutions were used for calibration.

$Al(OH)_3$ was analyzed after dissolution in sodium chloride (4 molar concentration of NaCl):[89] The dissolution of 0.12 g of Bayerite in 20 ml NaCl (4M) was achieved in a day at 150°C with continuous agitation.

AlOOH was analyzed after dissolution in sodium hydroxide (4 molar concentration of NaOH)[90];0.02g of AlOOH were dissolved in 20 ml sodium hydroxide (4 molar concentration of NaOH) during 5 days at 160°C with continuous agitation to be dissolved.

The content of traces in our samples was calculated by determining the number of nanomoles per million of cells.

2.4.9 X-ray photoelectron spectroscopy ( )

X-ray photoelectron spectroscopy (XPS) consists of measuring the photoelectrons emitted from top 10 nm of the material being irradiated by monochromatic X-rays. Owing to the particle size of our materials, these experiments let us identify their elemental composition, and the bonding of the atoms. A Kratos Analytical Axis Ultra DLD, using an Al Kα source monochromatized at 1486.6 eV was used NIMBE, CEA-Saclay, France. We used a hemispheric analyzer working at pass energy of 160 eV for the global spectrum, and 20 eV when focusing on the sole core levels. Energy calibration was realized using C1s = 285 eV.

2.5 Gas analysis

According to hydrogen concentration; the ampules containing irradiated samples were analyzed using two different techniques: micro-Gas chromatography and Trace-gas chromatography. Gas analysis were conducted in the Laboratoire de radiolyse et de la matière organique (LRMO) and LIONS, CEA-Saclay, France.

The concentration (mol/kg) of molecular hydrogen produced is deduced from the following equation:

(35)

$$[\boldsymbol{H_2}] = \frac{\boldsymbol{P_f} \cdot \%\, \boldsymbol{H_2} \cdot \boldsymbol{V_a}}{\boldsymbol{R} \cdot \boldsymbol{T} \cdot \boldsymbol{m_s}}$$

Where P_f is the final pressure, $\%\, H_2$ is the percentage of hydrogen measured by the chromatography, V_a is the volume of the irradiated ampule and m_s is the mass of the irradiated sample.

Radiolytic yields (G (H_2)) are calculated using the total energy deposited in the material.

(36)

$$\boldsymbol{G(H_2)} = \frac{\boldsymbol{[H_2]}}{\boldsymbol{D}}$$

This radiolytic yield can be deduced from the slope of the linear regression deduced from the graph of the production of H_2 as a function of the absorbed dose (Gy in D).

2.5.1 Gas chromatography µ-GC

Hydrated samples irradiated with electron beams and annealed samples were analyzed by µ-GC (µGC-R3000 SRA instrument) (LIONS) and Agilent 450 (LRMO) using ultrahigh purity argon (argon 6.0) as the carrier gas. Gas chromatographs were equipped with a Pomp turbo HiCube 80Eco (Pfeiffer) that provides a secondary vacuum. Irradiated gas is expanded in the chromatography line evacuated under vacuum. An automatic injection is performed after expanding the gas (0.3-0.4 bar) and mixing it with 1.2 bar of argon for 5 minutes in order to have a pressure greater than the atmospheric one before injecting.

The estimated error in the gas measurement is less than 10%. In this separation technique, gas phases are separated in three minutes. It is carried out in a capillary column (20 m MS 5Å, temperature 45°C, pressure 180 kPa). In the injector all the components in the sample will be vaporized (Injection time: 100 ms). The carrier gas was pure argon. Thermal conductivity detector was used. Soprane 3.5 software was used to control the µ-GC and data processing A calibration curve is obtained using standard gas mixture with various concentrations of H_2 (from 100 to 1000 ppm).

Figure 2.10 presents the calibration curve obtained for the SRA µ-GC.

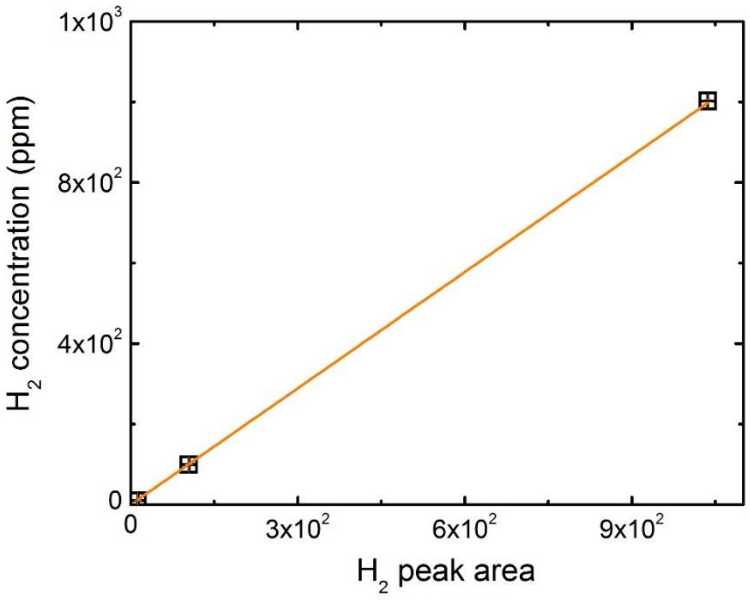

Figure 2.10. SRA µ-GC standard calibration curve ranging from 10 to 1000 ppm.

2.5.2 Trace gas chromatography

An Agilent 6890 Trace-Gas Chromatograph (Agilent Technologies, Santa Clara, CA) combined with a pulsed-discharge He photoionization detector from VICI Instrument Co, Inc. (PPD model D-3, Houston, TX) has been employed for the determination of molecular hydrogen released from electron beam irradiated samples. The estimated error in the gas measurement is less than 10%. The carrier gas used was ultra-high-purity helium. This technique provides the precision and detection limit (10 ppb) suitable for dry irradiated samples. In the case of GC chromatography and since small amounts of H_2 are detected, standards used were 0.5, 2, 10 and 100 ppm Figure 2.11.

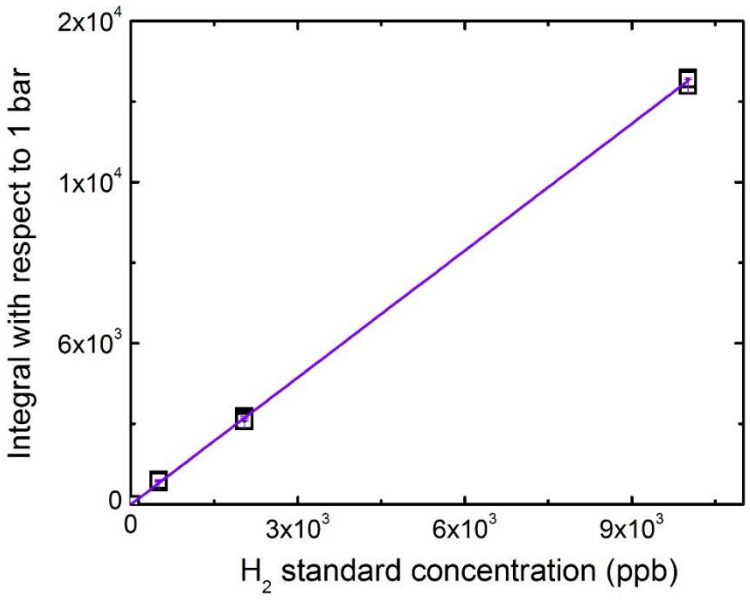

Figure 2.11. GC-Traces standard calibration curve ranging from 0.5 to 100 ppm.

Theoretical concentration of standard H_2 in ppb is plotted to the peak area. Peak area is divided by each initial expansion pressure so all samples are normalized to the same value. As for µ-GC, calibration curve was obtained using standard gas mixture.

2.5.3 Gas mass spectrometer MAT 271

Molecular hydrogen released from hydrated samples irradiated using Gamma rays and dry and hydrated samples irradiated using heavy ions was analyzed using a high resolution quantitative gas mass spectrometer with direct inlet for chemical and isotopic analysis (Thermo Fischer Scientific MAT-271) at LRMO, CEA-Saclay, France. Ionization occurred by electron impact, mass separation was performed with a magnetic sector, and ion detection by Faraday cup and electron multiplier. The detection limit was about 10 ppm depending on the gas matrix and mass interference.[91] After irradiation the gas mixture was admitted to the mass spectrometer via a "molecular" leak which means that the gas flow at the leak is in the molecular flow regime. Gas composition could be determined accurately because there is no mass discrimination and the leak rate of each gas is known using Graham's law (inversely proportional to the square root of the gas molar mass).

2.6 Summary

The chemicals and a variety of characterization methods used for surface and structure characterization before and after irradiation have been described in this chapter. Irradiation sources used for studying H atom formation in the radiolysis of AlOOH and $Al(OH)_3$ as well as chromatographs used to detect molecular hydrogen released and radiation induced defects have been detailed.

3. Chapter 3 Sample characterization

In this chapter, the atomic organization and bonding inside nanoparticles are detailed. The results of optimizing hydration and drying are shown. Impurities and specific surface area are presented. After comparing pristine and dry samples, the effect of hydration on samples is also shown. The characterization of irradiated samples is also presented. The content of this chapter is essential in order to understand in the next chapters the effect of structure, particle size, water sorption, particle size and irradiation on the production of molecular hydrogen.

3.1 Atomic organization of the nanoparticles

3.1.1 X-ray Crystallography (XRD)

The XRD pattern of the aluminum hydroxide and oxyhydroxides and the attributed crystallographic planes are shown in Figure 3.1.

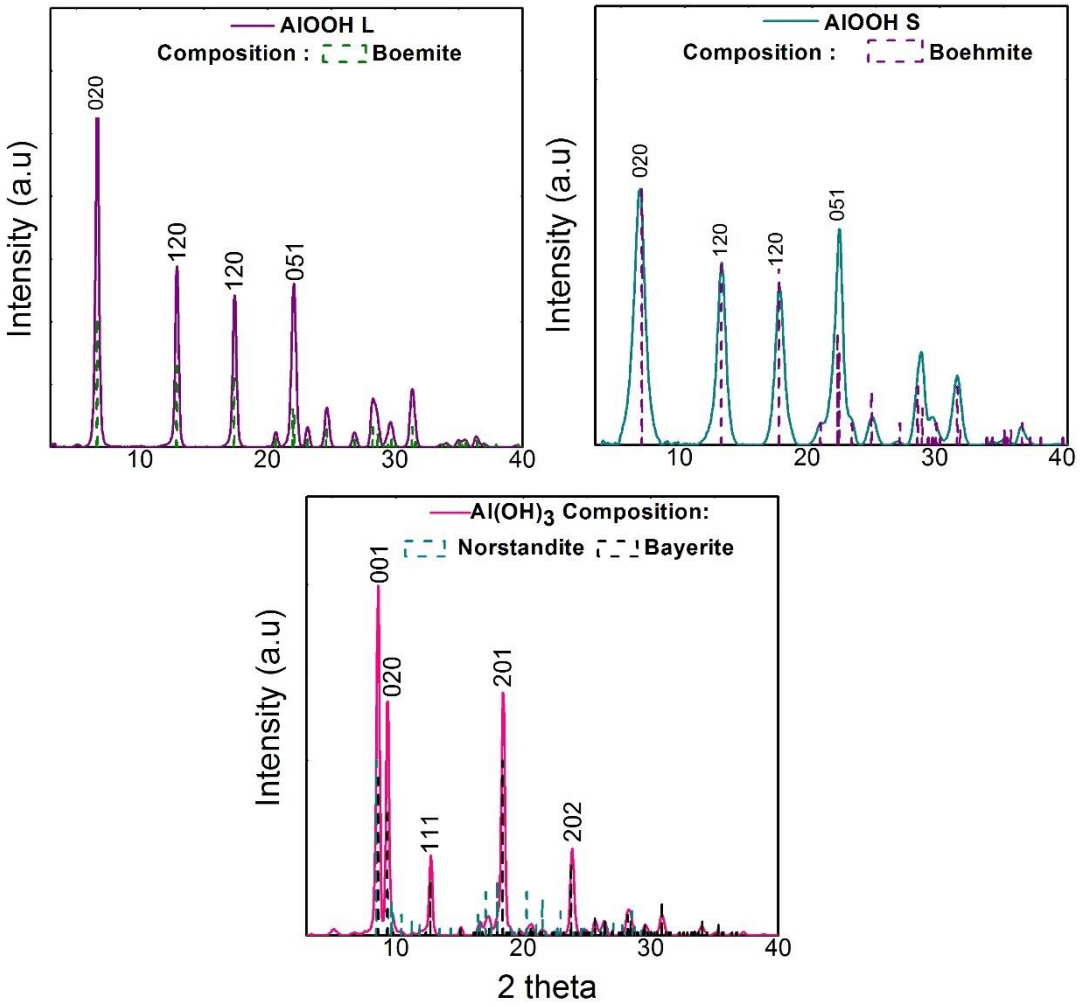

Figure 3.1. X-ray diffraction pattern of AlOOH L, AlOOH S and $Al(OH)_3$.

Boehmite was the only phase present in AlOOH L and S but $Al(OH)_3$ contains Bayerite and Nordstrandite (polymorph of Boehmite).

Concerning AlOOH L, the higher diffraction peak observed corresponds to the crystallographic plane (020). On the other hand, AlOOH S diffractorgram shows the lowest diffraction peaks. Concerning, $Al(OH)_3$ we observe a relatively higher intensity peak for the (001) and other crystallographic phases were seen such as (020) and (201). Spectra obtained were comparable to others in the literature.[92-93].

The XRD patterns of AlOOH S showing broader peaks confirm the smaller crystallite size. The peaks were narrower in the other AlOOH L and $Al(OH)_3$.

In order to see if any phase transformation occurred after heat treatment XRD was conducted on heated samples.

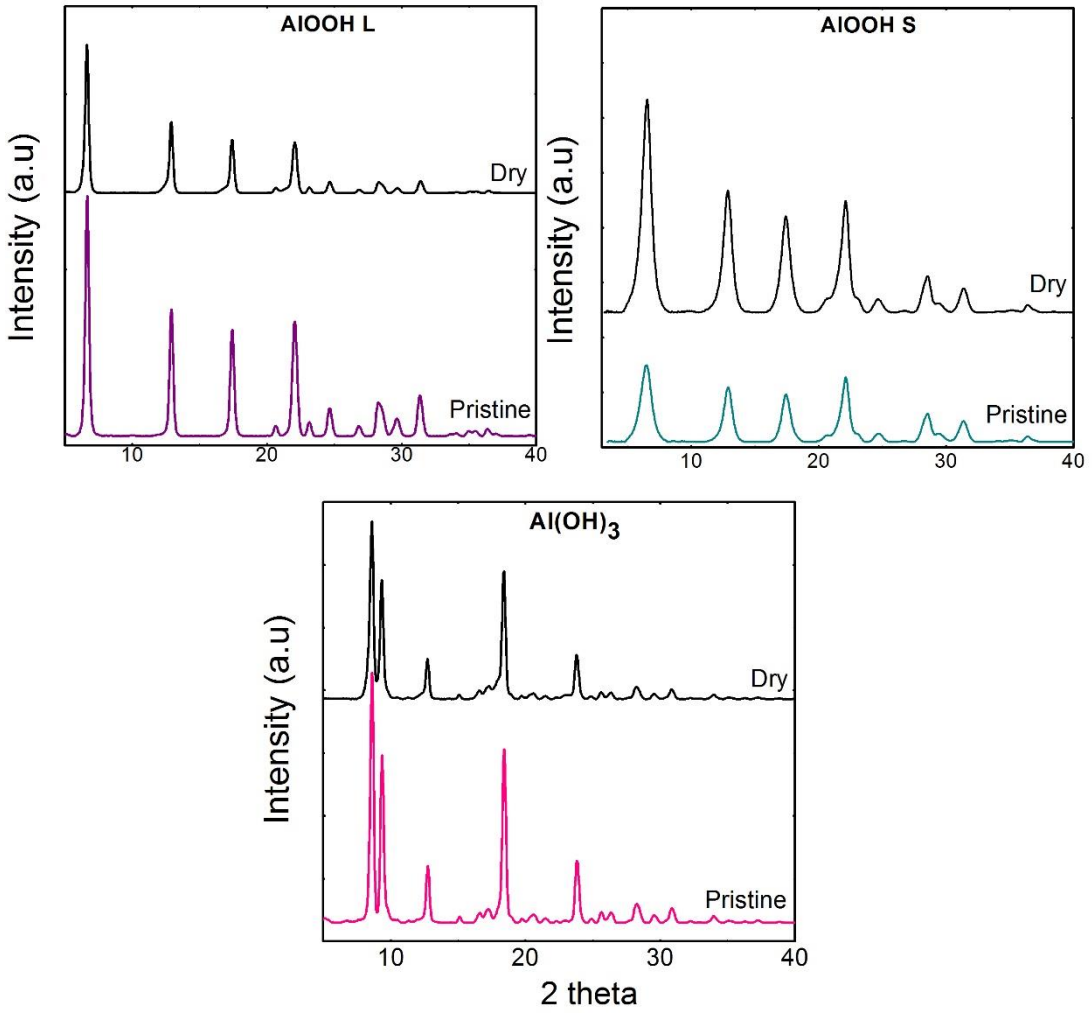

Figure 3.2. DRX of AlOOH and $Al(OH)_3$ comparing pristine and dry samples.

From DRX, we concluded that AlOOH L and S have an orthorhombic structure while $Al(OH)_3$ has an monoclinic one (Figure 3.3 and Figure 3.4).

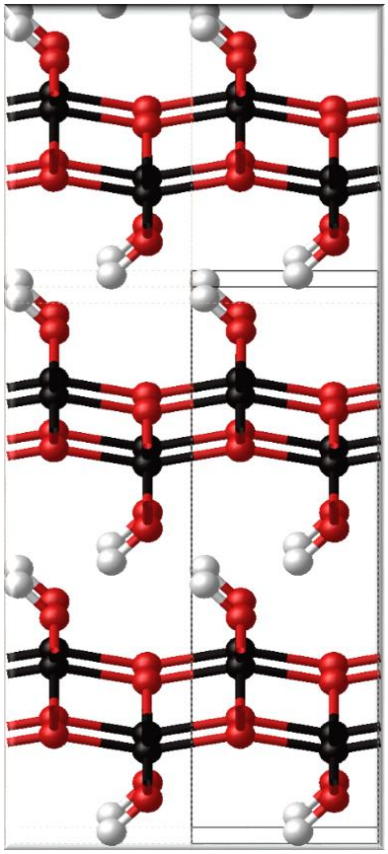

Figure 3.3. Modeled AlOOH showing 3 layers where each Al is linked to one O and OH.

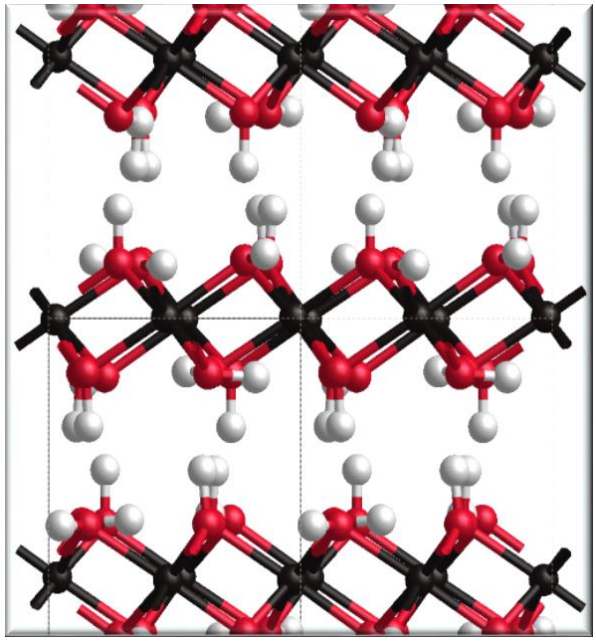

Figure 3.4. Modeled $Al(OH)_3$ showing 3 layers where each Al is linked to three OH.

3.2 Bonding inside Nanoparticles

3.2.1 Infrared spectroscopy (IR)

FTIR spectra obtained on the Boehmite and Bayerite samples are presented in Figure 3.5. It's worth noting here that all spectra's intensities were normalized based on the most intense peak in each case. The attributions of the main IR bands are presented in Table 3.1 along with the literature data.

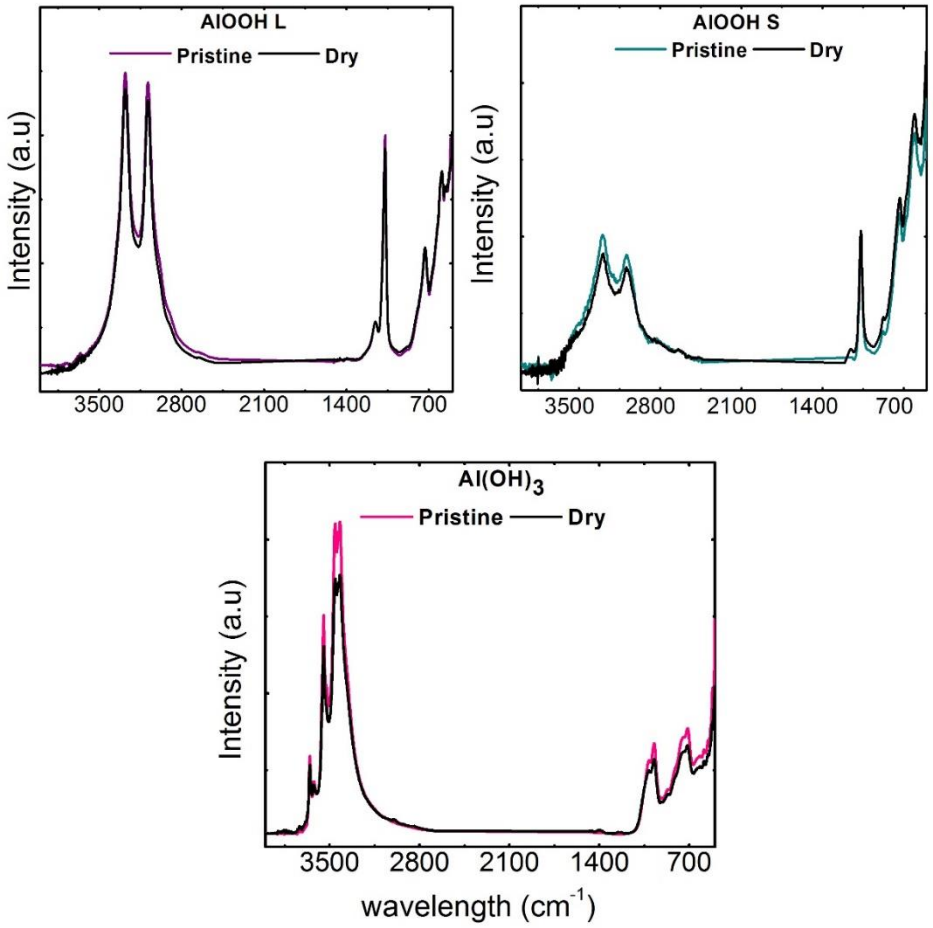

Figure 3.5. IR spectra of AlOOH and $Al(OH)_3$ comparing pristine and dry samples.

$Al(OH)_3$ spectra show sharp bands at 3548 and 3454 cm^{-1}. These bands attributed to υ OH were seen in Bayerite and Gibbsite samples described in many papers.[71, 94-97] The peak at 973 cm^{-1} seen in our $Al(OH)_3$ was also described as δ OH found in Gibbsite.[71, 94]

AlOOH S spectra show broad bands at 3295 cm^{-1} and 3093 cm^{-1}. They are in agreement with other literatures where they are attributed to OH stretching in other Boehmites.[71, 98] At 1066 cm^{-1} we have a δ OH bending.[99]

AlOOH L spectra show sharp and redshifted by 5 wavenumbers bands at 3281 cm^{-1} and 3088 cm^{-1}. These bands corresponding to Al-OH stretching groups were found in other

Boehmite samples described by Kloprogge et al.[71] The band found at 1071 cm^{-1} attributed to υ Al-OH symmetric bending was in agreement with other studies done on Boehmite and diaspore which is an α-AlOOH.[77,100 71, 101]

Comparing AlOOH L and S one can see the difference in the peak width. This can lead us to deduce that the number and strength of interactions between neighboring molecules or intermolecular interactions vary a lot and cause the bands to be relatively broad. As summarized by Brian Smith, the width of the IR peaks in a solid is determined by the number of chemical environments in a sample that is related in its turn to the strength of molecular interactions.

Table 3.1. Summary of the frequencies encountered in the IR spectra of AlOOH L, AlOOH S and $Al(OH)_3$. Attribution and comparison to the literature.

	Frequency (cm^{-1})	**Attribution**	**Reference**
AOOH L and S	1066-1071	δ OH	1068[99] 1070[101] 1071[71] 1077[102]
	3088-3093	υ OH	3090[98] 3092[99] 3096[71]
	3281-3295	υ OH	3283[71] 3295[99] 3297[98]
$Al(OH)_3$	973	δ OH	969[71] 980[94]
	3421	υ OH	3428[96-97] 3417[95]
	3454	υ OH	3452[71] 3453[95] 3468[94]
	3548	υ OH	3547 [95] 3617[94]

3.2.2 Raman spectroscopy

Raman spectroscopy was led in order to see if any H-H bonding could be seen after irradiation in the zone of 4161.13 cm.[1 103] This was not identified and maybe the sensitivity was not enough to detect small amounts of H_2 created in the irradiated samples. Therefore Raman spectra will be especially used as a complementary method to IR and to determine the low-wavenumber region (200-1200 cm^{-1}) (Figure 3.6).

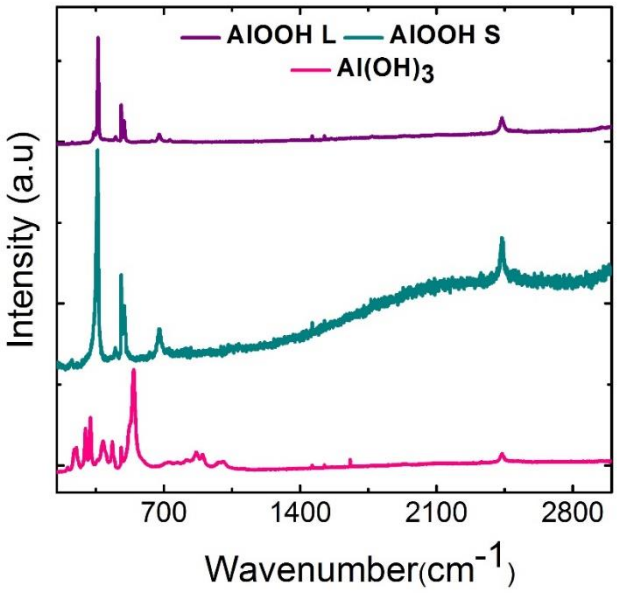

Figure 3.6. Raman spectra of $Al(OH)_3$ and AlOOH.

Table 3.2. Summary of the frequencies encountered in the Raman spectra of $Al(OH)_3$, AlOOH L and AlOOH S. Attribution and comparison to the literature are also shown.

	Frequency (cm^{-1})	Attribution	Reference
AOOHL and S	356-358	Al-O	360[104]
	480-488	Al-O	495[104]
	675-677	γ OH	674[104]
	3073-3077	υ OH	3085[104]
	3217-3223	υ OH	3220 3226[104]
$Al(OH)_3$	246	Al-O	250[104-105]
	325	Al-O	322[104-105]
	439	Al-O	435 446 [104]
	545	γ OH	545[104-105]
	537	γ OH	538[104-105]
	910	δ OH	918[104-105]
	995	δ OH	995[105]
	3415	υ OH	3420[104]
	3651	υ OH	3652[104]
	3545	υ OH	3532 [104]

Ruan et al and Huang et al published some works on Gibbsite, Bayerite Diaspore and Boehmite and their results were compared to ours in Table 3.2.[104-105]

Table 3.2 summarizes the major peaks. Raman spectra of Bayerite, Gibbsite and Diaspore were more complex than that of the Boehmite in the low-wavenumber region that are assigned to deformation and translational mode of the alumina phase. To sum up the region between 2800 and 3700 cm^{-1} is associated with hydroxyl groups in aluminum oxyhydroxides and hydroxides while between 700 and 2000 cm^{-1} the bands are assigned to Al-O bond. [104, 106]

3.2.3 X-ray photoelectron spectroscopy (XPS)

For all minerals XPS survey spectra and high resolution core line spectra (O 1s and Al 2p) were obtained. Figure 3.7 shows details of each survey and the fits conducted on each sample.

$Al(OH)_3$, AlOOH L and S show Al 2p transition at 74.10, 74.08 and 74.09 eV respectively with a FWHM of 1.4 eV already observed in similar Bauxite samples.[107] For all samples the doublet Al 2p 3/2 and 1/2 are in the same fit.

In the case of $Al(OH)_3$ one strong peak was observed at 531.70 eV and a weaker one at 533 eV. The first peak is attributed to the hydroxyl group Al-OH and the second is assigned to organic oxygen coming from the carbon substrate.

Two major peaks related to O 1s were seen in the case of AlOOH L and S at 530.7 eV and at 531.9-532 eV Figure 3.7. A third broader peak was also seen at 532.9-533.5 eV. By comparison with the XPS spectra of $Al(OH)_3$, the peak centered at 531.9-532 eV is attributed to hydroxyl group and the peak at 530.7 eV to O^{2-}.

For $Al(OH)_3$ the ratio O to Al was equal to 3 to 1 and that was expected based on the composition of $Al(OH)_3$. For AlOOH the ration O to Al was 2 to 1.

Table 3.3 resumes peak attribution, position and concentration in the case of AlOOH L, S and $Al(OH)_3$.

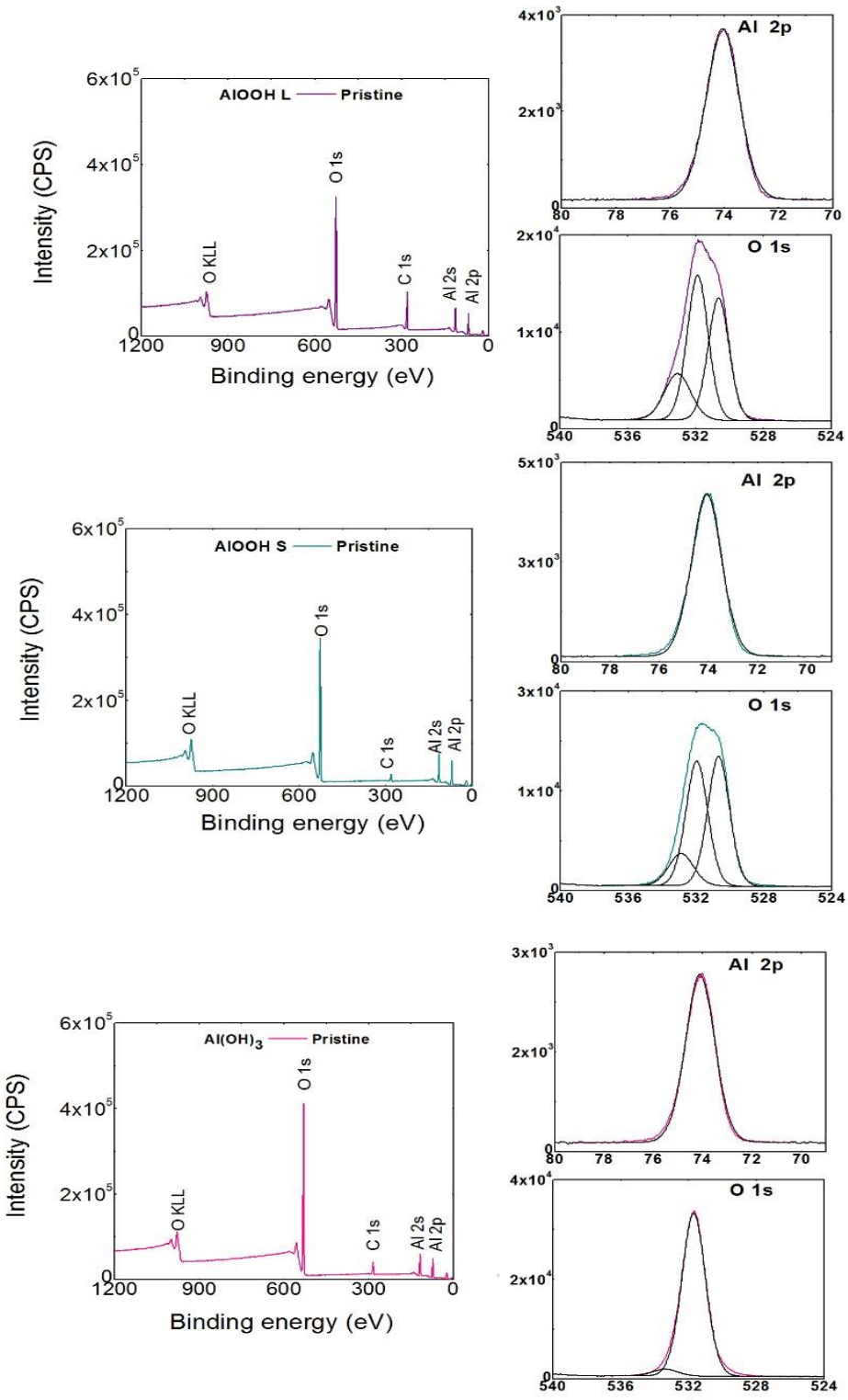

Figure 3.7. XPS survey spectra of pristine AlOOH L, AlOOH S and $Al(OH)_3$ and high resolution of Al 2p and O1s.

Table 3.3. XPS peak position and atomic concentration of each element before irradiation.

Before Irradiation	Name	Position (eV)	FWHM	Area	Concentration (%)
AlOOH L	O 1s-1	530.65	1.459	18193.67	17.50
	O 1s-2	531.89	1.459	21507.14	20.68
	O 1s-3	533.07	1.840	8697.20	8.36
	Al 2p	74.08	1.431	5002.34	19.48
AlOOH S	O 1s-1	530.69	1.516	24293.33	29.07
	O 1s-2	531.97	1.516	23378.69	27.98
	O 1s-3	532.90	1.729	6903.76	8.26
	Al 2p	74.09	1.433	5760.98	27.92
$Al(OH)_3$	O 1s-1	531.70	1.643	52829.17	62.49
	O 1s-2	533.39	1.741	2355.53	2.79
	Al 2p	74.10	1.424	4411.00	21.12

Our studies are comparable to similar ones done by Rotole and Sherwood on a variety of aluminum hydroxide phases.[108-112] The differences in energy among the aluminum hydroxide and oxyhydroxides are very small and are in the same order of magnitude as the experimental precision of XPS, moreover the differences in energy between irradiated and pristine samples are due to the precision of XPS and are not to be considered.

3.3 Impurities

3.3.1 Inductively coupled plasma atomic emission spectrometry (ICP-AES)

As seen from Figure 3.8, samples bought with the highest purity available were not free of trace impurities.

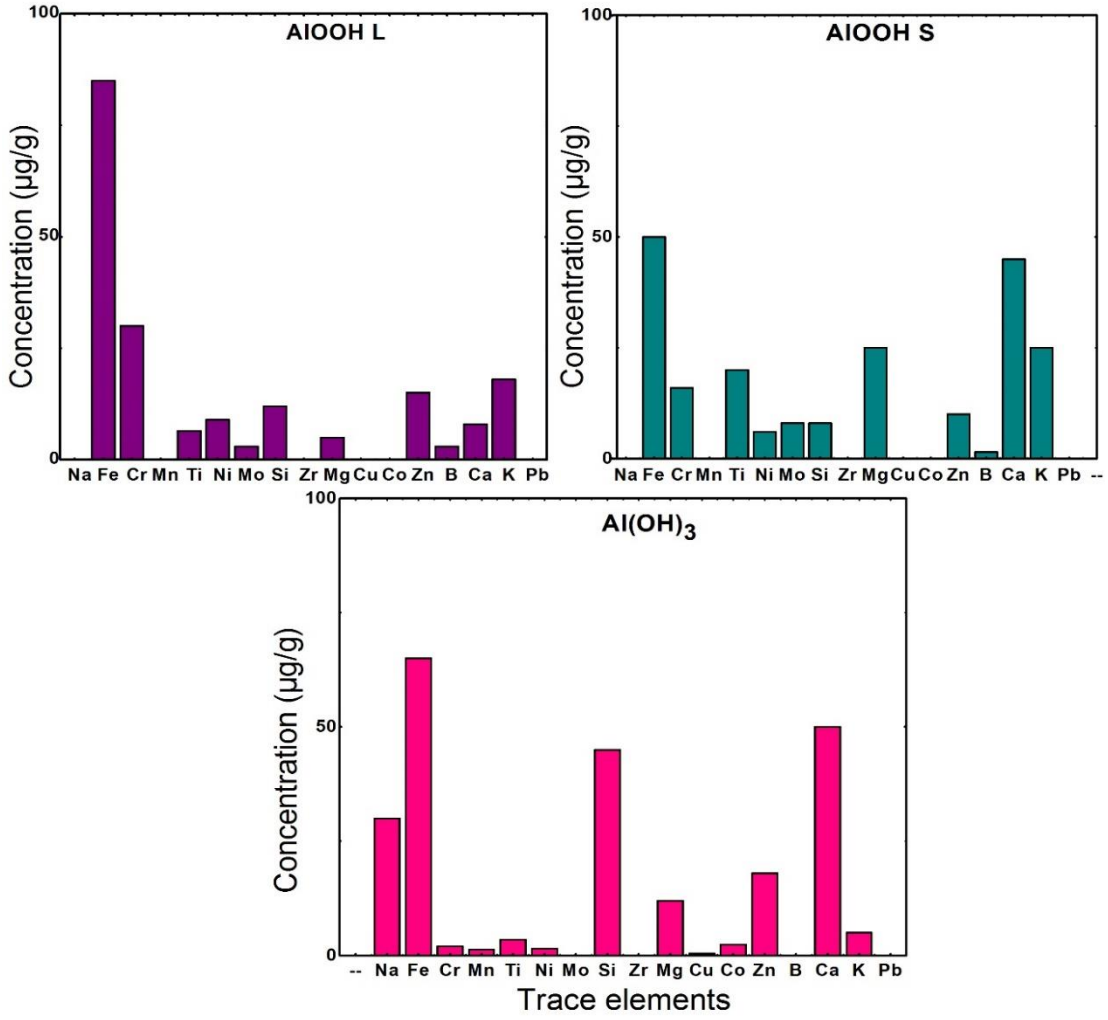

Figure 3.8. ICP-AES of AlOOH and $Al(OH)_3$ showing chemical trace impurities in each case.

Iron seems to be the most important being at 85, 65 and 50 µg/g in AlOOH S, AlOOH L and $Al(OH)_3$ respectively. Na was only detected in $Al(OH)_3$. Na is known to be present in Zeolite solid systems and to capture electron. It was only detected in $Al(OH)_3$. The presence of chromium impurities in aluminum oxides is a known fact; it can penetrate into the nanopowder in the course of production as well as Fe^{3+} that has been described in many other systems.[48]

3.3.2 Electron paramagnetic resonance magnetometer (EPR)

Figure 3.9 shows EPR spectra of the pristine materials at room temperature.

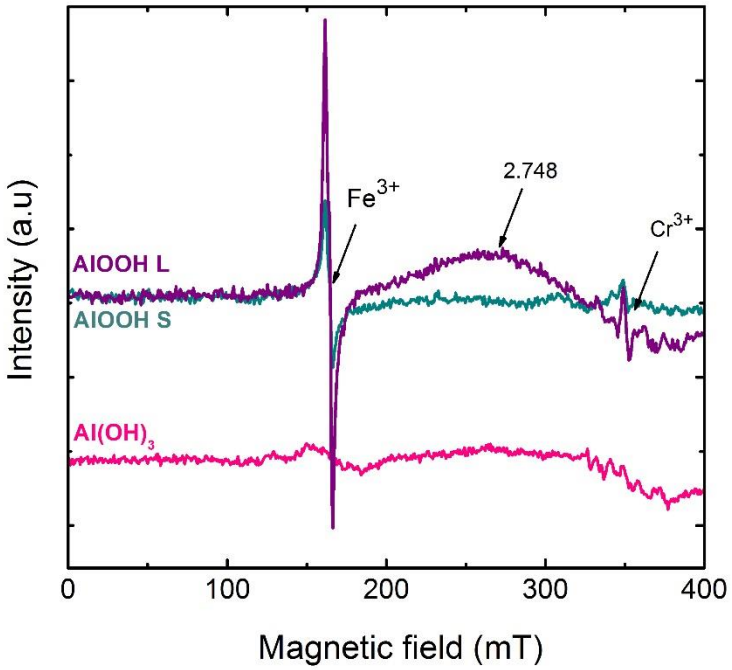

Figure 3.9. EPR spectrum of pristine AlOOH L, AlOOH S and $Al(OH)_3$ showing paramagnetic impurities

No impurities are shown in non-irradiated $Al(OH)_3$, Non-irradiated AlOOH shows three signals: one intense peak at g = 4.25 characteristic of Fe^{3+}, another broad one at 267 mT (width 113 mT) and a third small peak is seen g = 1.99 attributed to Cr^{3+}.[48, 113-115] No Mn^{2+} detected in the three samples.

The morphology of our samples will be discussed in the next section.

3.4 Particle shape and surface

3.4.1 Scanning electron microscopy (SEM)

The SEM images of pristine samples presented in Figure 3.10 show that the materials consisted of particles with irregular shapes, a few nanometers in size.

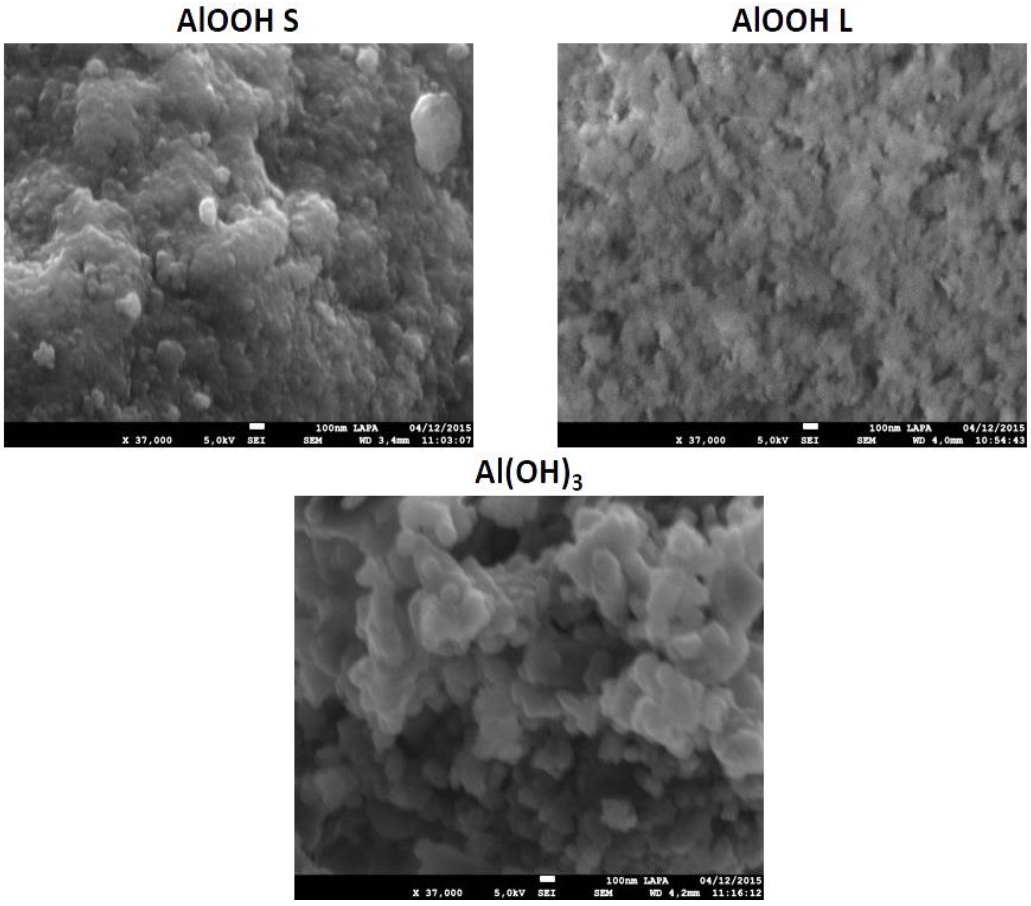

Figure 3.10. Scanning electron microscopy: differences between pristine AlOOH S, AlOOH L and $Al(OH)_3$ (x 37 000).

Not much information could be extracted from these images since the imaging of individual nanoparticles with SEM was difficult. Nevertheless, some conclusions on the size and shape could be drawn, a clear difference was seen between AlOOH S and L where S has more spaces between particles. $Al(OH)_3$ has spherical to irregular forms, while AlOOH S and AlOOH L have undefined particle shapes.

3.4.2 Brunauer-Emmett and Teller analysis (BET)

Specific surface areas, noted BET-SSA, were calculated using Brunauer-Emmett-Teller (BET) where relative pressure P/P0 method between 0 and 0.2.[116-117] Pore size distribution was obtained using a Barrett-Joyener-Halenda (BJH) model on the desorption isotherm. AlOOH L has the lowest specific surface area which is 41 m^2/g. $Al(OH)_3$ and AlOOH L specific areas were 268 and 111 m^2/g respectively.

3.4.3 Water sorption

3.4.4 Thermogravimetric analysis (TGA)

In order to explore the dehydratation behavior of AlOOH L, AlOOH S and $Al(OH)_3$, we carried out the thermogravimetric analysis (TGA) measurement. Figure 3.11 indicates the weight loss of the three samples as a function of temperature.

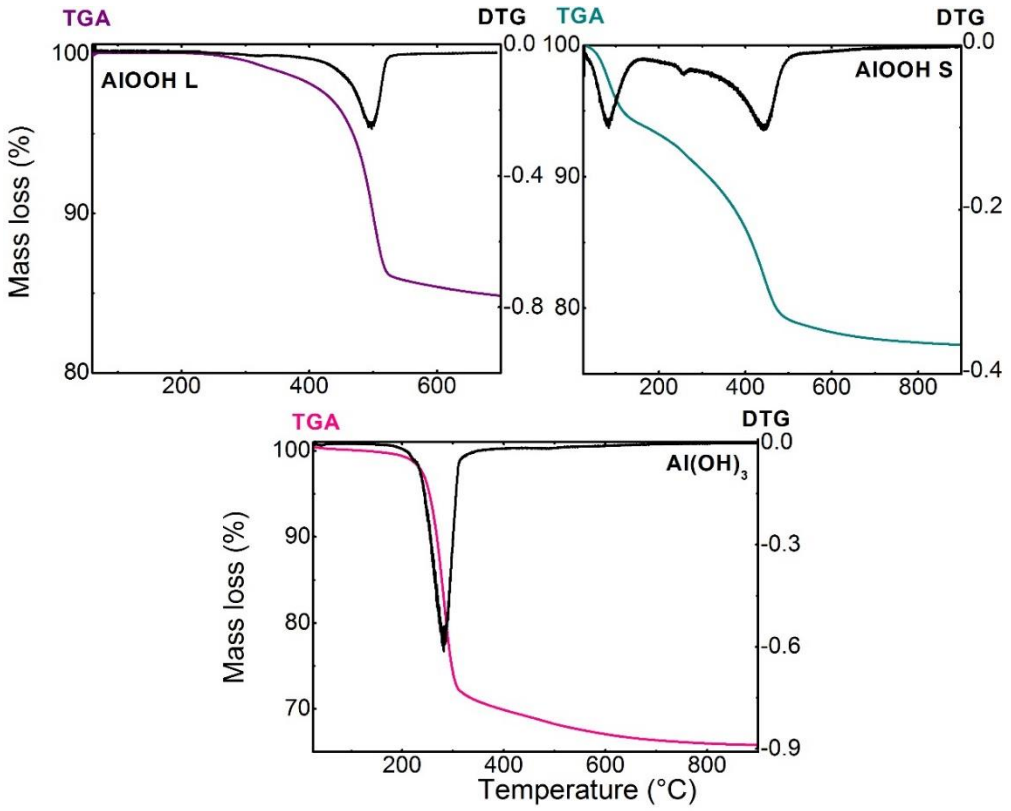

Figure 3.11. TGA and DTG of pristine AlOOH and $Al(OH)_3$ under N_2.

First Derivative thermogravimetric curve (DTG) peak that is due to loss of water that is not chemically bound (physisorbed water) is clearly observed for AlOOH S before 250°C. The total mass loss is 35 ± 3 % (450°C).

In AlOOH L case, the adsorbed water eliminated in the temperature range less than 250°C is difficult to observe in Figure 3.11 since water loss was only 1.2 ± 0.1 %) of the total mass and phase transformation occurs between 250°C and 600°C. After 600°C, Al_2O_3 is formed and the total mass loss is 18.5 ± 1.5 %.

As one can notice, the mass loss of AlOOH S after dehydroxylation was higher than that of AlOOH L and this is due to the higher content in adsorbed.

As for $Al(OH)_3$, two different mass losses occurs: in the temperature range less than 200°C which is weakly bound water, this was only 0.4 ± 0.1 % and is not clear from the

given graphs and the second mass loss between 250°C and 350°C assigned to the dehydroxylation of $Al(OH)_3$. The total mass loss is about 30 ± 5 %.

3.4.5 Drying

The drying conditions were determined in order to remove only adsorbed water. No weight loss until 150°C The elimination of the first derivative peak attributed to adsorbed water (between 20˚C and 150˚C) is not so clear in the case of AlOOH L and $Al(OH)_3$ since it was close to the detection limit. Dry AlOOH L was prepared by evacuating 1.2± 0.1 percent of water from its initial mass. Dry AlOOH S lost 6.8 ± 0.5 % and $Al(OH)_3$ 0.4 ± 0.1 %. As a first step, adsorbed water was verified to be removed by considering the weight loss between 20˚C and the temperature of the first Derivative thermogravimetric curve (DTG) peak that is due to loss of water that is not chemically bound (physisorbed water). Care was taken to not exceed the temperatures higher than that of the first DTG peak, where water loss is due to dehydration of the structure.

We verified that the thermal treatment did not change the structure and crystallites size of the materials.

3.4.6 Hydration

As mentioned in chapter 2, hydrated samples were prepared using desiccators and ampules. TGA was used for adsorption and desorption isotherm in order to predict water uptake for each imposed relative humidity Figure 3.12.

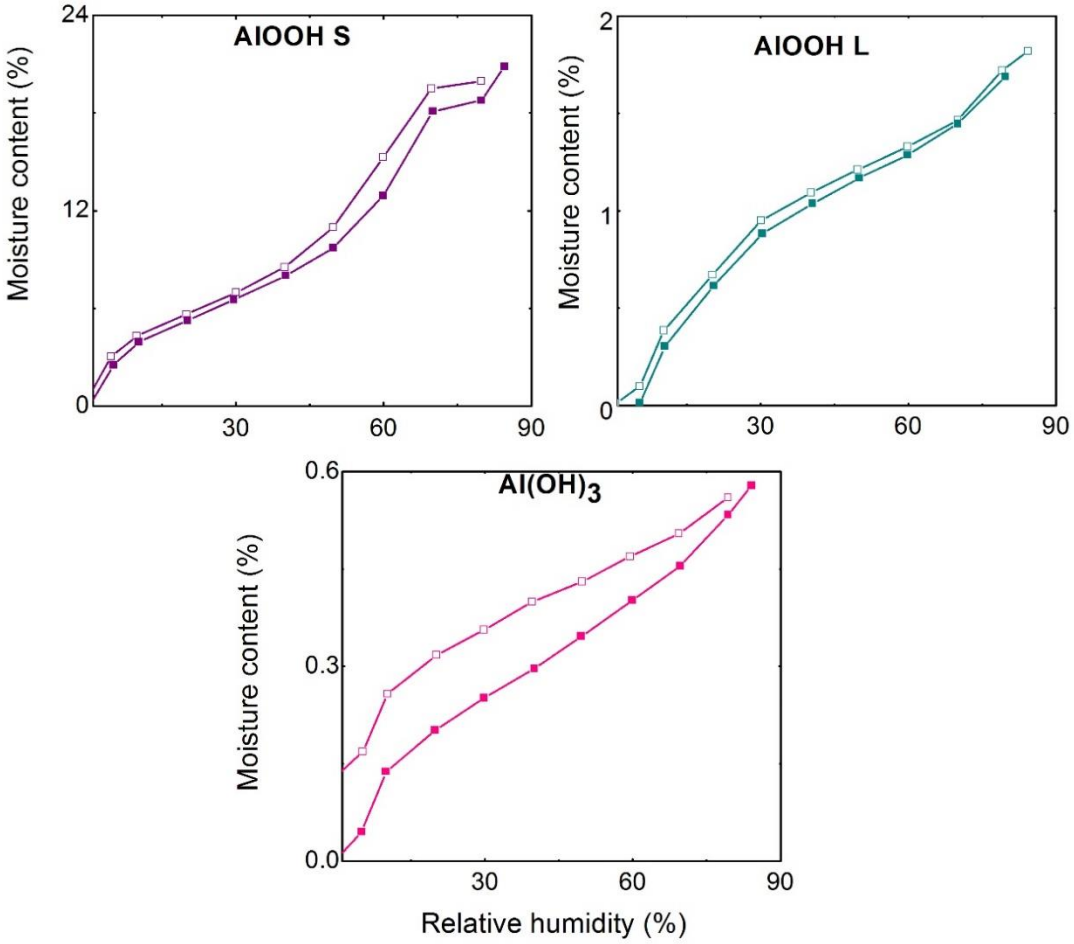

Figure 3.12. Water uptake isotherm using TGA with respect to relative humidity. Full squares are attributed to adsorption and empty ones to desorption.

From Figure 3.12, one can see that 0.5% is the maximum water uptake in the case of $Al(OH)_3$ and 0.05% is the minimum at 11%. As for AlOOH L, 0.9% was the minimum and 1.7 % the maximum. Water uptake was the highest in the case of AlOOH S where 18.4 % of water can be adsorbed at 76 % imposed relative humidity (RH).

Hydrated samples placed into desiccators or ampules were not dried before hydration. In the case of $Al(OH)_3$, a hysteresis is seen, this could be due to the resolution since we are talking about a maximum water uptake of 0.6%.

The use of ampules containing salt solutions was intended in the first place to avoid exposing our conditioned samples to air, but, when weighing ampules we noticed that water uptake was not the maximum in the ampules. For AlOOH L and $Al(OH)_3$ differences between water uptake in ampules and desiccators are not important but in the case of AlOOH S, water uptake at 76% was of 17% while it was 14% in ampules. Desiccator values were closer to that of the isotherm. It's true that the use of ampules avoids us from exposing samples to air but the hydration process was probably less efficient in this constrained environment.

Table 3.4 resumes water uptake comparing TGA isotherms, mass weighed from hydrated samples in ampules, and percentage deduced from dessicator samples using TGA. All in all, water uptake was so similar between 11%, 44% and 76% in the case of $Al(OH)_3$ and AlOOH L but in the case of AlOOH S bigger differences were observed. Thermal analysis can vary from a Boehmite to a Gibbsite or Diaspore and even for the same chemical formula different thermogram can be obtained this depends on the origin of the sample, its content in impurities, amorphous phases and particle-size.[71, 118-120]

Table 3.4. Summary of water uptake with respect to relative humidity imposed in the case of AlOOH L, AlOOH S and $Al(OH)_3$. Water uptake from TGA imposed relative humidity through isotherms, water uptake weighed in hydrated ampules and TGA measurements for water uptake into dessicators are shown.

Sample	RH imposed (%)	Water uptake from TGA isotherm (%)	Water uptake weighed from hydrated ampules (%)	Water uptake from TGA of desiccator hydrated samples (%)
AlOOH L	11	0.30 ± 0.02	0.05 ± 0.00	0.60 ± 0.05
	44	1.08 ± 0.08	0.38 ± 0.03	1.30 ± 0.10
	76	1.58 ± 0.01	1.58 ± 0.01	1.10 ± 0.08
AlOOH S	11	3.86 ± 0.35	1.30 ± 0.11	3.80 ± 0.34
	44	8.70 ± 0.78	4.50 ± 0.40	7.40 ± 0.66
	76	18.45 ± 1.66	14.16 ± 1.27	17.42 ± 1.56
$Al(OH)_3$	11	0.14 ± 0.02	0.17 ± 0.02	0.34 ± 0.05
	44	0.31 ± 0.05	0.36 ± 0.05	0.42 ± 0.06
	76	0.50 ± 0.07	0.78 ± 0.11	0.50 ± 0.07

3.5 Effect of irradiation

In this section irradiated samples presented are only those conducted using heavy ions. We suppose that these ions create more defects in the samples and if no changes are observed under these irradiations than no alterations would occur in electron beams used for the study of defects in the next section.

3.5.1 FTIR

FTIR was also conducted on irradiated samples. Red spectra in each of Figure 3.13 show the IR peaks of irradiated samples conducted at 500 kGy. The dose choice was based on having a significant dose and to see if any alterations occurred in the samples.

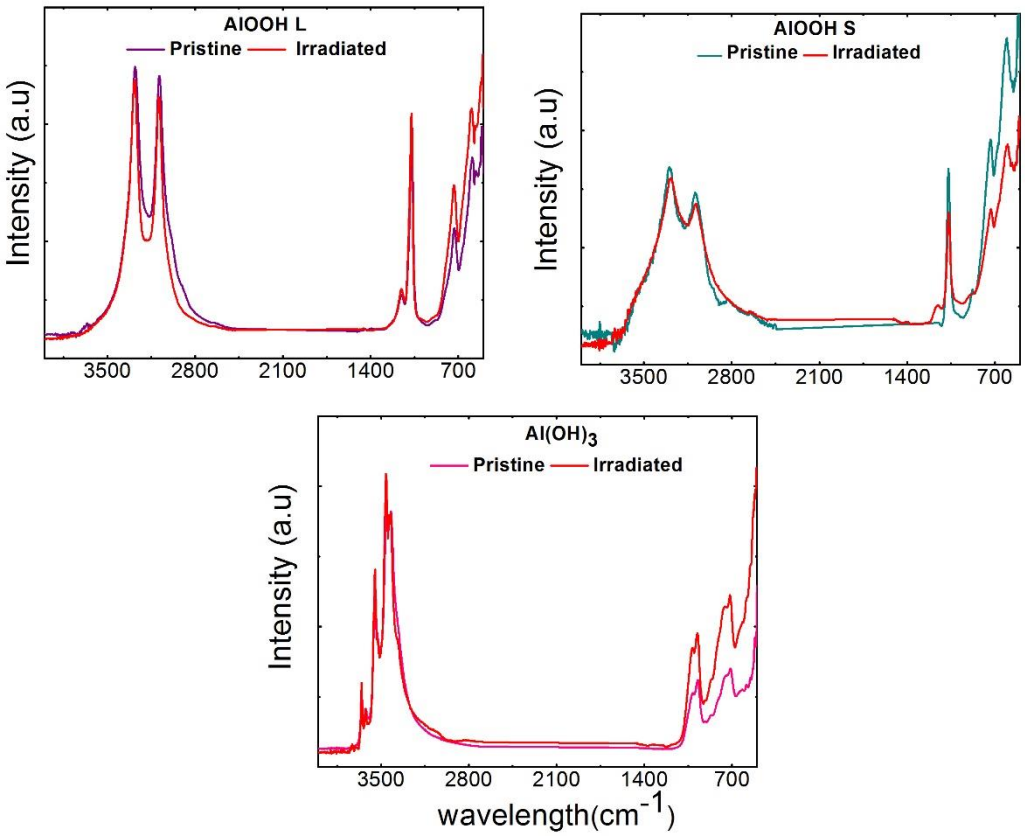

Figure 3.13. FTIR spectra of heavy ions irradiated at 500 kGy AlOOH L, AlOOH S and $Al(OH)_3$ compared to that of pristine ones.

No difference was seen between pristine and irradiated $Al(OH)_3$. Though, an asymmetric narrowing is noticed in the case of irradiated AlOOH L , this could be seen as a relatively weak OH bonding.

3.5.2 XRD

In order to check if any changes in phases occurred after irradiation, an XRD test was done on 200 kGy irradiated samples, Figure 3.14 .

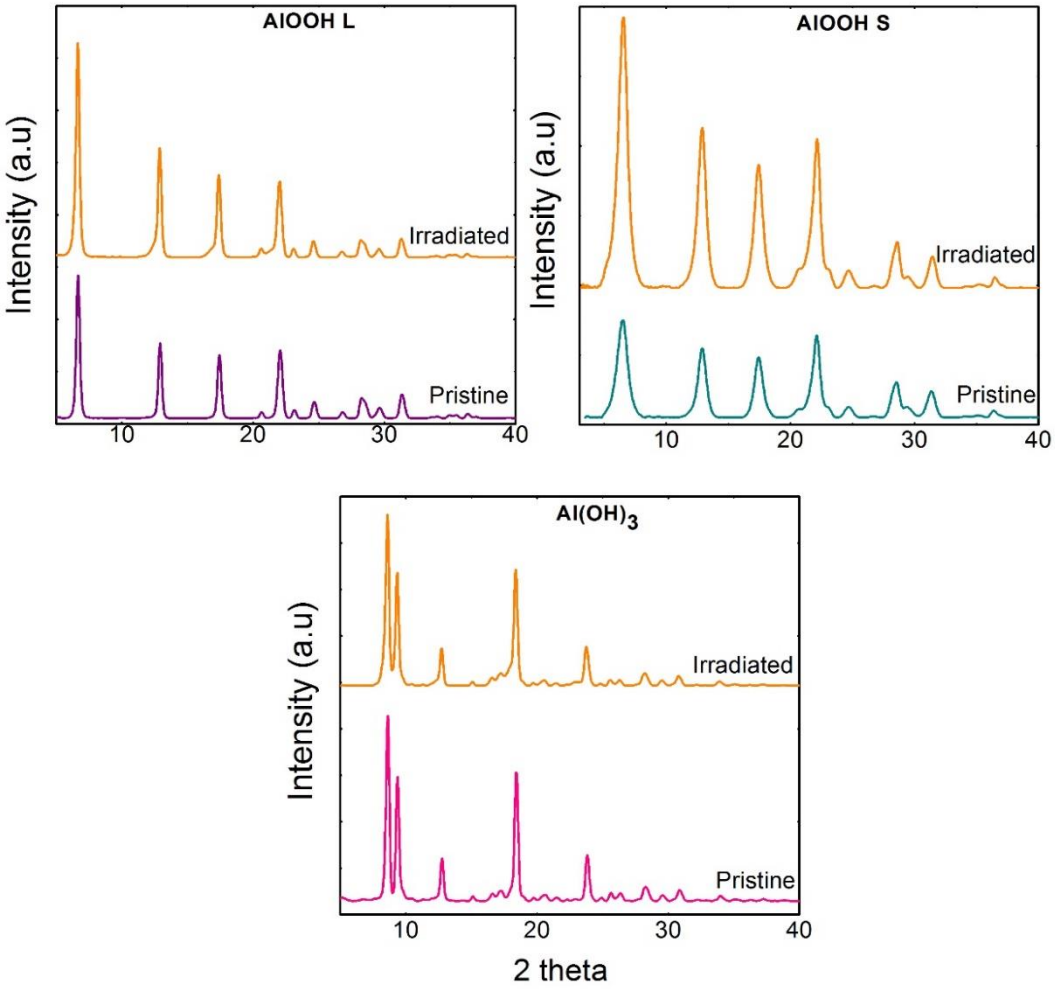

Figure 3.14. XRD spectra of irradiated at 200 kGy using heavy ions AlOOH L, AlOOH S and Al(OH)3 compared to that of pristine ones.

No differences in phases were seen when comparing pristine and irradiated samples.

3.5.3 XPS

In order to insure if irradiation occurred any alteration to functional groups on the surface, XPS on irradiated samples was conducted at 120 kGy using electron beams and was compared to that of pristine ones Figure 3.15. No difference was seen between pristine and irradiated samples. (Table 3.5).

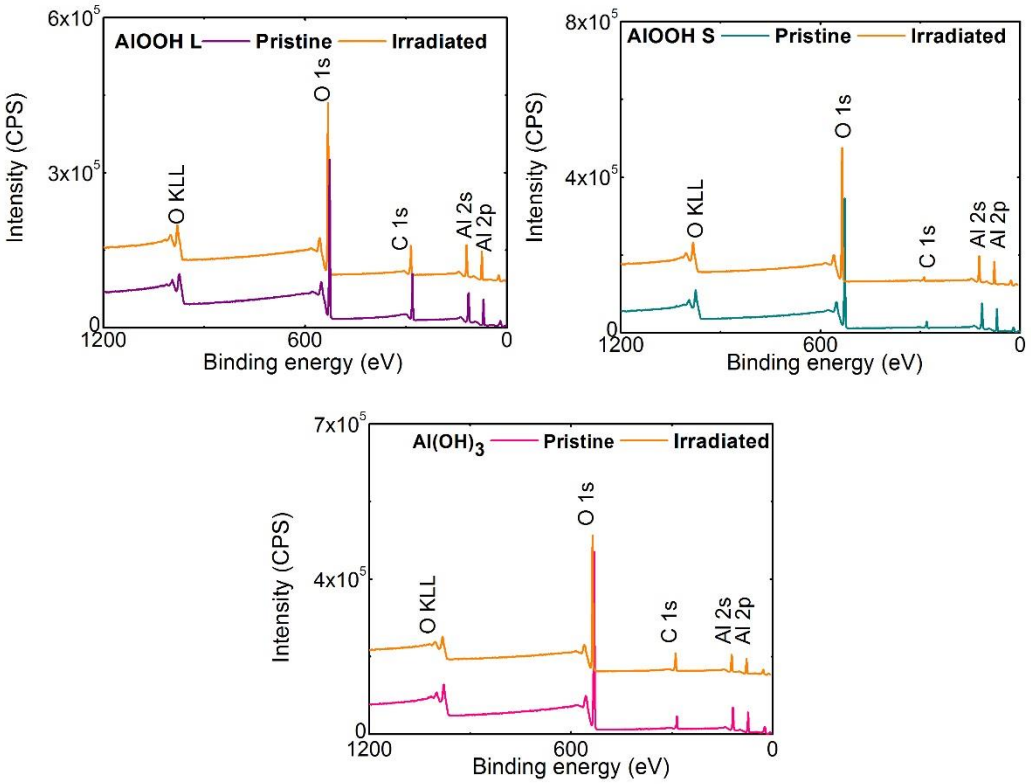

Figure 3.15. XPS spectra of irradiated AlOOH L, AlOOH S and $Al(OH)_3$ compared to that of pristine ones.

Table 3.5. XPS peak position and atomic concentration of each element after irradiation.

After Irradiation	Name	Position (eV)	FWHM	Area	Concentration (%)
AlOOH L	O 1s-1	530.69	1.420	21308.29	22.44
	O 1s-2	531.92	1.420	21320.62	22.46
	O 1s-3	532.90	1.916	8512.20	8.97
	Al 2p	74.11	1.374	5367.21	22.89
AlOOH S	O 1s-1	530.66	1.481	23357.70	28.69
	O 1s-2	531.98	1.481	23521.65	28.89
	O 1s-3	533.00	1.730	5488.91	6.74
	Al 2p	74.06	1.398	5523.98	27.47
$Al(OH)_3$	O 1s-1	531.70	1.620	39875.76	57.09
	O 1s-2	533.52	1.973	1830.42	2.62
	Al 2p	74.11	1.387	3455.63	20.03

3.5.4 EPR

To see if the intensity of impurities changed especially to detect if any reduction of Fe^{3+} occurred due to irradiation EPR spectrum was deduced from irradiated samples at 120 kGy using electron beams and was compared to that of pristine ones (Figure 3.16). No difference in intensity was seen between pristine and irradiated samples.

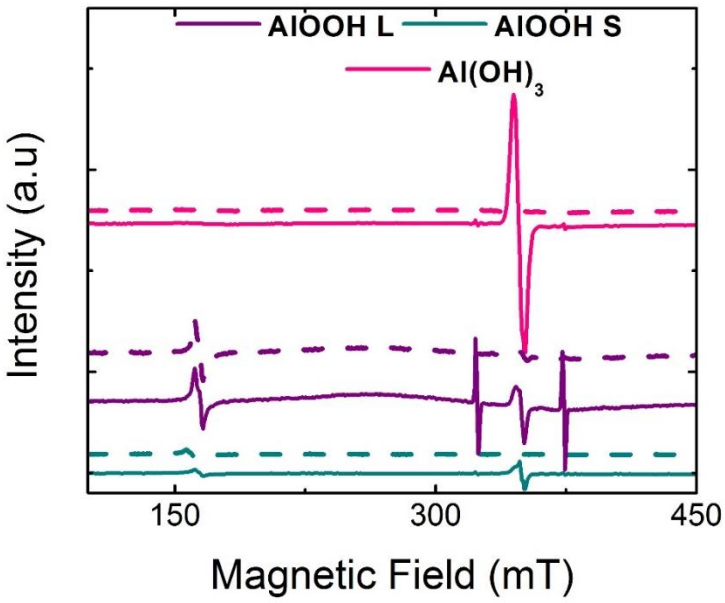

Figure 3.16. EPR spectra of irradiated AlOOH L, AlOOH S and $Al(OH)_3$ compared to that of pristine ones (dashed).

3.6 Summary

This section was dedicated to resume the differences and similarities between samples. No significant changes were induced in irradiation samples at 500 kG from heavy ions or at 120 kGy using electron beams which leads us to conclude that the reference dose used to study the defects and analyze gas did not alter the samples.

Table 3.6. Summary comparing the main characteristics after characterising each sample.

Structure	AlOOH L	AlOOH S	$Al(OH)_3$
Particle size (nm)	18	5	20
Particle shape	Irregular aggregated	Irregular separated by spaces	Irregular to spherical
Specific surface area (m^2/g)	41	268	111
Phase purity (%)	94	95	90
Chemical impurities	Fe>Cr>K>Zn	Fe>Ca>Mg>Ti>Cr>	Fe>Ca>Si>Na>Zn>Mg
Paramagnetic impurities	Fe^{3+} and Cr^{3+}	Fe^{3+} (less than AlOOH L)	0
Transition temperature (°C)	450	450	350
Water uptake at 76% RH (%)	1.60 ± 0.01	18.45 ± 1.66	0.50 ± 0.07
Physisorbed water at RT (%)	1.2 ± 0.1	6.8 ± 0.5	0.4 ± 0.1

4. Chapter 4. Molecular hydrogen production from dry aluminum hydroxide and oxyhydroxide

The objective of this chapter is to determine the molecular hydrogen yield for dry materials and its variation with the structure and particle size. In the first part, molecular hydrogen production from dry AlOOH L is compared to that of AlOOH S (Large and small-particle sizes respectively) and $Al(OH)_3$ Gamma irradiations were also conducted and are briefly described. Electron beam irradiation is treated in details. In the second part the study of Radiation induced defects (RID) by EPR spectroscopy is developed.

4.1 Hydrogen production

4.1.1 Gamma rays

Dry samples were irradiated by Gamma rays for 70 hours (22 kGy). Sealed ampules were used and gas released from irradiated samples was directly analyzed using GC-traces (see Chapter 2). Many tests were done on AlOOH L and $Al(OH)_3$ and it was impossible to obtain reproducible results.

As the production of hydrogen is very low, the measurements of the final H_2 concentration were highly dispersed. Even if Pyrex ampules were used, one may think about ampules contribution when seeing these dispersions. Values differed from more than one order of magnitude for the same sample mass and dose. It was concluded that higher doses are necessary to obtain reliable data. Moreover we cannot exclude back reactions leading to the consumption of H_2 released owing to long irradiation time.

In this chapter only the results obtained from electron irradiations are represented for dry materials.

4.1.2 Electron beam irradiation

4.1.2.1 Molecular hydrogen production at room temperature

In Figure 4.1, the production of molecular hydrogen as a function of the dose is shown using two types of experiments:

- The first one concerns the same sample irradiated at different doses (close squares).
- The second one concerns different samples irradiated at 120 kGy (open squares).

AlOOH L and $Al(OH)_3$ samples were irradiated from 7 kGy until 120 kGy. Dry AlOOH S did not release significant quantities of H_2 between 6 kGy and 91 kGy therefore a higher dose was applied, 390 kGy in order to determine the hydrogen produced. Even at this dose AlOOH S. H_2 concentration was very low and close to the detection limit.

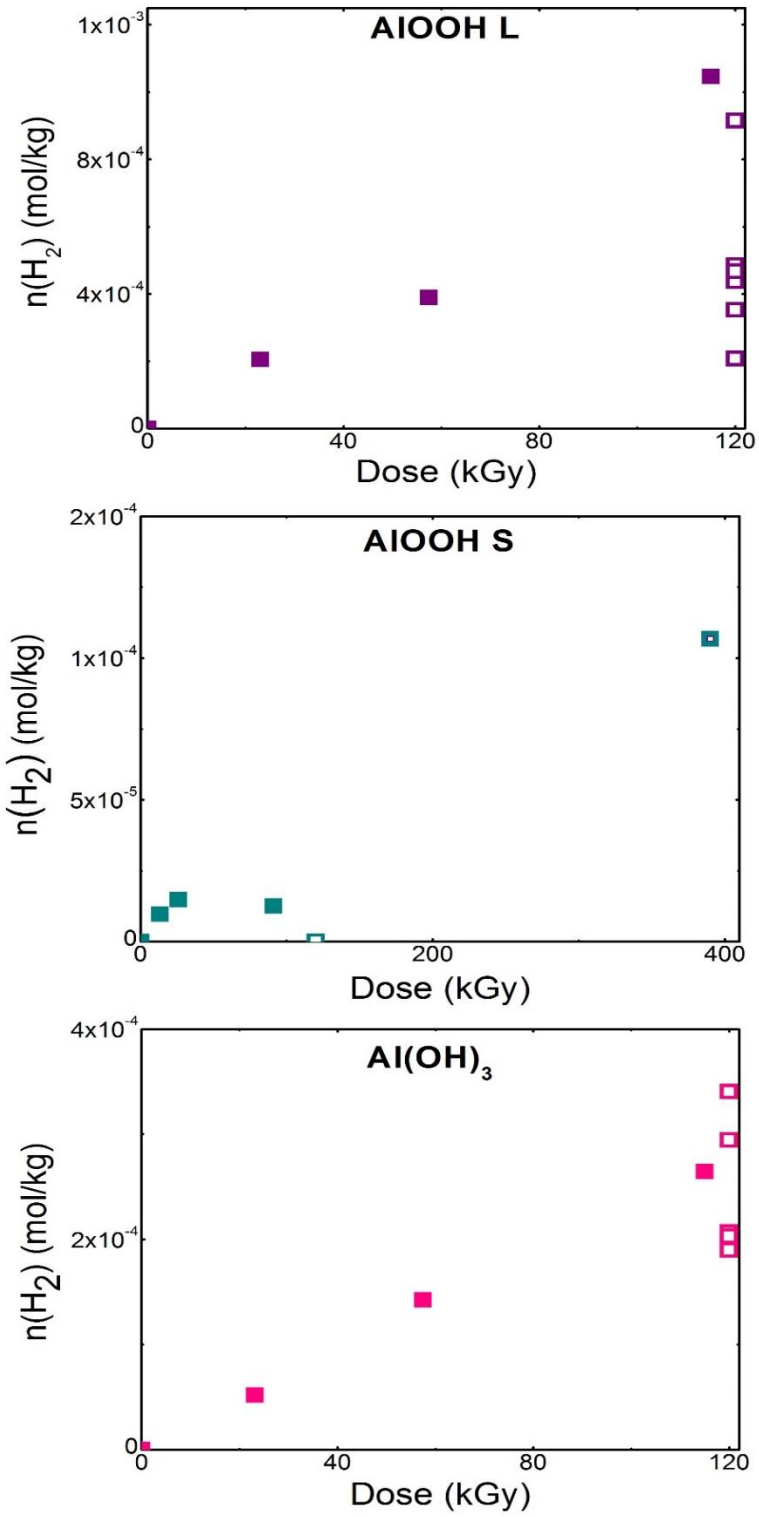

Figure 4.1. Hydrogen production as a function of the dose from dry AlOOH L, AlOOH S and $Al(OH)_3$ irradiated using electron beams. Close squares: same sample irradiated at different doses. Open squares: separated samples irradiated at 120 kGy.

In most cases, when the dose is cumulated on the same sample, H_2 production is proportional to the dose. Then H_2 radiolytic yields can be deduced from the slopes of the different curves. This is seen in the type of experiment applied on the same sample irradiated at different doses (close squares). Though, radiolytic yield given in Table 4.1 is the average of all the results obtained from both type of experiment since it is clear that these samples are really sensitive and results changed from an experiment to another despite all the care considered while preparing samples and irradiating in order to reproduce the same experimental conditions.
The results were relatively dispersed especially for AlOOH L.

The dispersion of the results can be attributed to the drying efficiency, or material aging in storage. In the next chapter it will be seen that H_2 production is very sensitive to adsorbed water. As the materials come from the same batch, we suppose that there is no difference in chemical composition, structure and particle size. Variations of the LINAC characteristics were tentatively corrected by dosimetry measurements.

Molecular hydrogen yields totally differ between AlOOH L and AlOOH S. Having the same chemical formula, these samples released different H_2 quantities. AlOOH L having the large particle-size released $(5 \pm 2) \times 10^{-9}$ mol/J while the maximal G value of AlOOH S was tentatively estimated to be 4×10^{-11}mol/J.
G (H_2) value obtained from irradiated $Al(OH)_3$ was $(2.1 \pm 0.5) \times 10^{-9}$ mol/J.
Two points emerge from these results:

- First, one can notice the important effect of particle size on hydrogen production: large-particle size of AlOOH samples produced more hydrogen than smaller ones. This result seems contradictory because one can imagine that hydrogen release should be easier in small particle size. Surface reactions are promoted in small particle size materials and H radicals were closer in the same particle which facilitates their recombination. [7] This was not the case of our samples where large particle size released more molecular hydrogen.

- Second, structure can affect molecular hydrogen production even if the constitutive atoms are the same. Moreover, in the case of the largest particle size AlOOH L even if it is less hydrogenated than $Al(OH)_3$ produces more H_2.

Concerning aluminum hydroxide and oxyhydroxide there is some discrepancy between $Al(OH)_3$ results and those obtained by Westbrook et al Table 4.1. [6] The difference can be attributed to particle size, sample purity, type of irradiations used and the efficiency of drying treatments. In their article the authors did not detail the characterization of the materials and the heat treatment conditions.

Table 4.1. H_2 radiolytic yields released at room temperature from AlOOH S, L and $Al(OH)_3$ and compared to the literature (Our results, resumed in this table were irradiated using electron beams while other hydroxides from literature were irradiated using Gamma rays).

Material	$G(H_2)$ (mol/J) x 10^{-8}	Reference
AlOOH L	0.57-1.3	[6]
AlOOH L	0.5 ± 0.2	Our results
$Al(OH)_3$	0.21 ± 0.05	Our results
AlOOH S	0.04 ± 0.02	Our results
$Al(OH)_3$	0	[6]

The mechanism of hydrogen production will be discussed later. At this time the formation of hydrogen in the solid is probable. Then its release can be limited by diffusion and a part of the hydrogen can be occluded in the structure of the materials. Dissolution and annealing experiments were conducted in order to see if any molecular hydrogen is trapped inside the structure after irradiation. A series of isochrones annealing till 250°C were also performed to accelerate hydrogen diffusion. In order to be sure if all molecular hydrogen potentially formed under irradiation was released, annealing experiments were conducted above the phase transition temperature (400˚C and 500˚C for $Al(OH)_3$ and AlOOH respectively) until total transformation into Al_2O_3 occurred. Results are detailed in section 4.1.2.3 and 4.1.2.4.

4.1.2.2 Trapped Molecular hydrogen

Barsova et al showed that a significant concentration of molecular hydrogen can be trapped inside strontium and barium hydroxides after gamma-irradiation. The fraction of hydrogen occluded varies between 10 to 60% of the total H_2 production.

In order to verify if the materials can store some hydrogen, dissolution tests have been conducted on $Al(OH)_3$ electron irradiated at 171 kGy (see section 2.3.5.1). Degassing

operation was repeated three times. The mix was heated for 2 hours at 130°C until complete dissolution.

After dissolution, H_2 concentration in the ampule was analyzed by mass spectrometry. It appears that this concentration is below the analytical detection limit (~5 ppm). Trace GC cannot be used since acidic conditions were used. Then it was concluded that the concentration of trapped hydrogen for $Al(OH)_3$ was inferior to 1.1×10^{-11} mol/kg.

4.1.2.3 Hydrogen production after annealing up to 250°C

Post irradiation annealing experiments were performed on electron-irradiated dry samples at 120 kGy or 240 kGy.

- The same sample was heated from 40°C up to 250°C in 40°C steps. The duration of the thermal treatment was one hour for each 40°C steps. At each step the molecular hydrogen released was measured.
- Hydrogen production was measured also directly after annealing at 250°C during one hour.

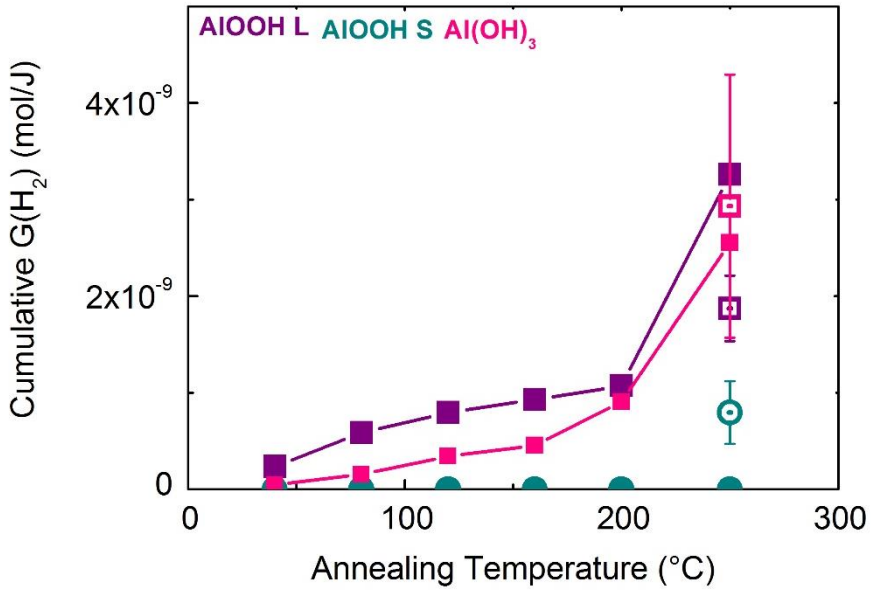

Figure 4.2. Effect of temperature (up to 250°C) on hydrogen released from samples irradiated using electron beams at 120 kGy.

Erreur ! Source du renvoi introuvable. shows the variation of the released hydrogen yield as a function of the annealing temperature. It reveals that significant amounts of hydrogen or hydrogen precursors were trapped in the irradiated materials.

Below 200°C, the quantities of released hydrogen from $Al(OH)_3$ and AlOOH L are small while **AlOOH S releases no hydrogen**. The process accelerates at 250°C. This temperature seems to be the threshold temperature for hydrogen diffusion or detrapping. The cumulative released maximum hydrogen yields measured at 250°C are resumed in Table 4.2. Room temperature radiolytic yields are also recalled. In order to see if any hydrogen still trapped inside the structure we tended to continue sample annealing until phase transition temperature.

4.1.2.4 Hydrogen production above transition phase temperature

As explained in chapter 2, in order to analyze gas released after the transition temperature, measurements were conducted using a water trap.

This thermal treatment was applied either directly without any previous annealing at lower temperatures or after a series of annealing at temperature inferior to 250°C. The cumulative hydrogen production measured after annealing for one hour at 400°C and 500°C for $Al(OH)_3$ and AlOOH respectively are resumed in Table 4.2. Like RT measurements the dispersion is important for AlOOH L. Despite this dispersion it is clear that a significant H_2 quantities release at elevated temperatures and that molecular hydrogen quantified before annealing represents only a small part of the total hydrogen formed under irradiation.

After annealing at the transition temperature, roughly similar amounts of H_2 were released from AlOOH L and $Al(OH)_3$. Although the quantities of trapped hydrogen is still inferior for AlOOH S compared to AlOOH L, the difference is far less pronounced than that observed at RT.

Table 4.2. Hydrogen yields at RT and after annealing at 250°C and above the phase transition. The yields at RT represent the mean of different doses measurements while high temperatures are conducted on 120 and 240 kGy.

$G(H_2)$ (mol/J) x 10^{-8}	**H_2 released at RT**	**H_2 occluded at 250°C**	**H_2 Total occluded 250°C + 500°C**
AlOOH L	0.51 ± 0.2	0.2 ± 0.05	1.2 ± 0.9
AlOOH S	(0-0.04) ± 0.02	0.08 ± 0.03	0.4 ± 0.1
$Al(OH)_3$	0.2 ± 0.05	0.3 ± 0.06	0.7 ± 0.1

From these annealing experiments, one can conclude that H_2 or its precursor are located inside the structure and its diffusion was harder in the case of AlOOH S and requires thermal activation.

4.1.3 Swift heavy ion irradiations

In order to precise the influence of LET, experiments were conducted. From Figure 4.3, we can deduce that unlike hydrogen radiolytic yields obtained using electron beams, $Al(OH)_3$ gives the lowest molecular hydrogen radiolytic yield, then comes AlOOH L with a highest value. Unfortunately, only one measurement is available for AlOOH S and H_2 quantified from heavy ion irradiations was 10 times greater than that from electron beam irradiations

Radiolytic yields of molecular hydrogen were barely similar in electron beam and heavy ion irradiated $Al(OH)_3$ (2×10^{-9} and 3×10^{-9} mol/J respectively). These yields were higher in AlOOH L and S irradiated using heavy ions, values are resumed in Table 4.3. This should be the opposite since heavy ion radiations can change substantially the H_2 yields by increasing locally the concentration of ionization sites, H_2 precursors tend to recombine with local defect than to form H_2 and an increase of H_2 has to be seen. The effect of structure is well noticed here where the production of molecular hydrogen is less efficient in AlOOH.

In order to see if samples irradiated using heavy ions trapped H_2 precursors. Annealing was done up to 200°C. Technical problems prevented us from going above this temperature. The corresponding radiolytic yields were calculated using the cumulated hydrogen released after the whole annealing process and are resumed in Table 4.3.

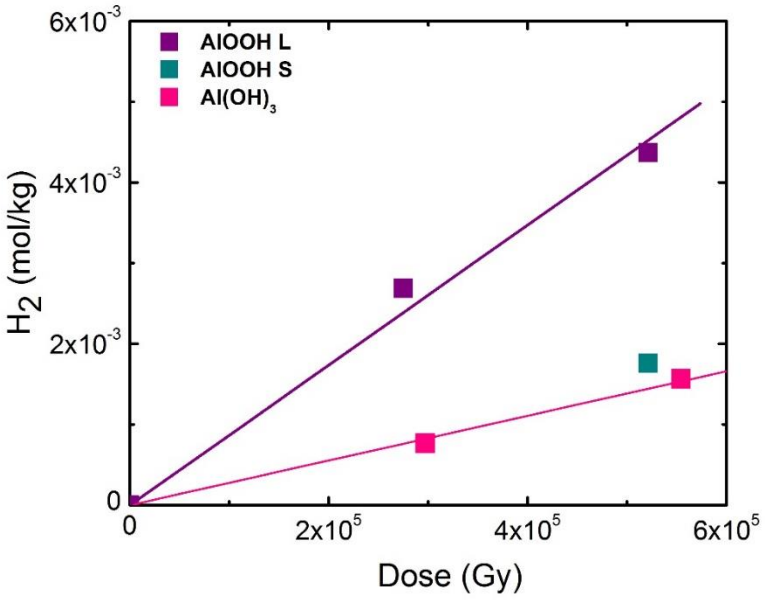

Figure 4.3. Hydrogen production at RT from dry AlOOH L, S and $Al(OH)_3$ irradiated with Ar^{18+} as a function of the dose.

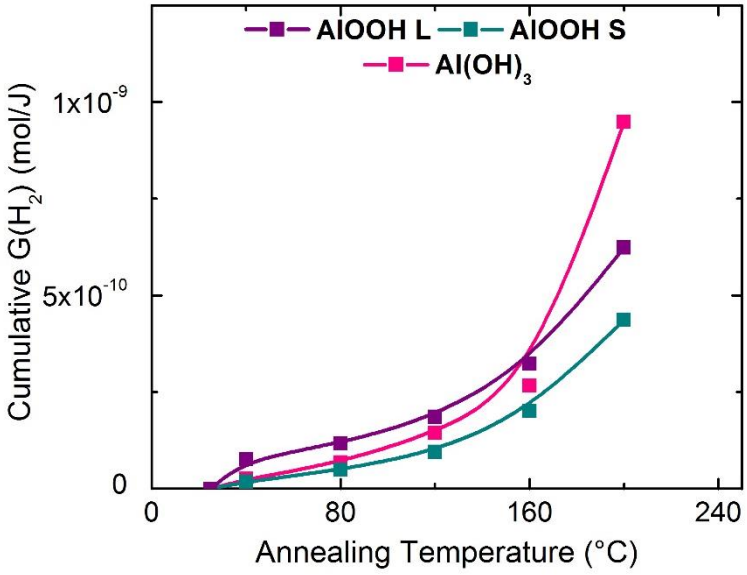

Figure 4.4.Effect of temperature (up to 200˚C) on hydrogen released from samples irradiated with heavy ions at 250 kGy (AlOOH L and $Al(OH)_3$) and 520 kGy (AlOOH S).

After annealing, results obtained from samples irradiated using heavy ions are not so significant comparing to that at room temperature, it was crucial to continue to the phase transition temperature to release all the molecular hydrogen. A significant

quantity may be occluded and didn't release before 250°C as seen in the annealed samples irradiated using electron beams.

AlOOH S released H_2 at 200°C under heavy ion irradiations while it didn't from electron beams. Further experiments should be done on irradiated samples using heavy ions in order to understand their different behavior.

Table 4.3. Radiolytic yields of irradiated samples using heavy ions before and after annealing

$G(H_2)$ (mol/J) x 10^{-8}	**H_2 released at RT**	**H_2 occluded at 250°C**
AlOOH L	0.8	0.03
AlOOH S	0.4	0.02
$Al(OH)_3$	0.3	0.07

In order to understand the process responsible of hydrogen production and release, radiation induced defects were studied using EPR spectroscopy. The aim of the work presented in the next part is to identify the defects and precise their thermal stability.

4.2 Radiation induced defects

EPR spectra of paramagnetic centers originating from electron beam irradiation of $Al(OH)_3$ and AlOOH S and L have been measured and will be discussed in this section. In order to give a general idea of paramagnetic centers formed at room temperature, EPR spectra of irradiated hydrates at 120 kGy, are shown in Figure 4.5. The spectra were normalized by the sample weight.

From Figure 4.5, an intense doublet separated by 50 mT identified in AlOOH L was assigned to H radicals (see Chapter 1). The stability of H radicals will be discussed in the next section. They were barely seen in the case of $Al(OH)_3$ and does not exist in the case of AlOOH S.

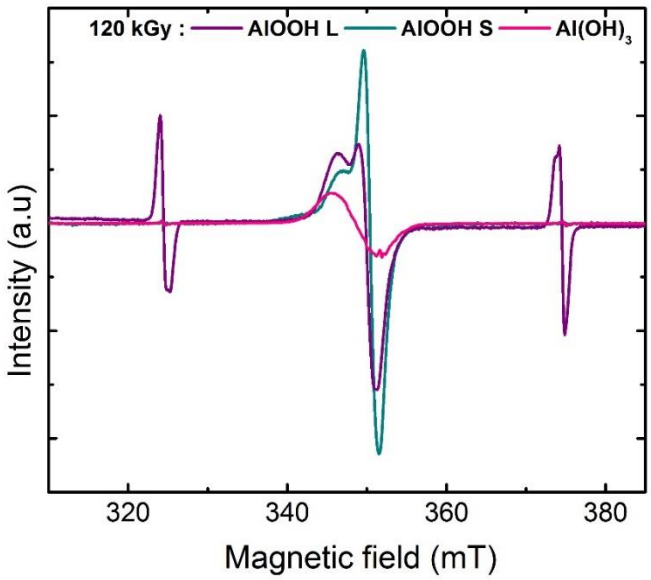

Figure 4.5. EPR Spectra of electron irradiated AlOOH L, S and $Al(OH)_3$ at 120 kGy.

Generally speaking Figure 4.5 shows that the RID of the two types of materials are different. Therefore we will present the results separately. For each material the effect of the dose and the thermal stability of the RID have been investigated.

4.2.1 Bohemite AlOOH

4.2.1.1 Dose effect at RT

Figure 4.6 presents the EPR spectra of electron irradiated AlOOH S at various doses comprised between 6.5 and 130 kGy. At the lower dose the EPR signal appears at a broad singlet of peak-to-peak line width ΔH_{pp} close to 5 mT. A signal centered at $g = 1.96$ independent from the dose is also observed (this signal is not present in non-irradiated samples). At high dose a narrower singlet superposes progressively. This new component can be isolated by subtraction (see the insert of Figure 4.6). Its spin parameters are: $g = 2.010 \pm 0.001$ and $\Delta H_{pp} \approx 1.7\ mT$. The subtraction reveals also the appearance of the broad feature at low fields.

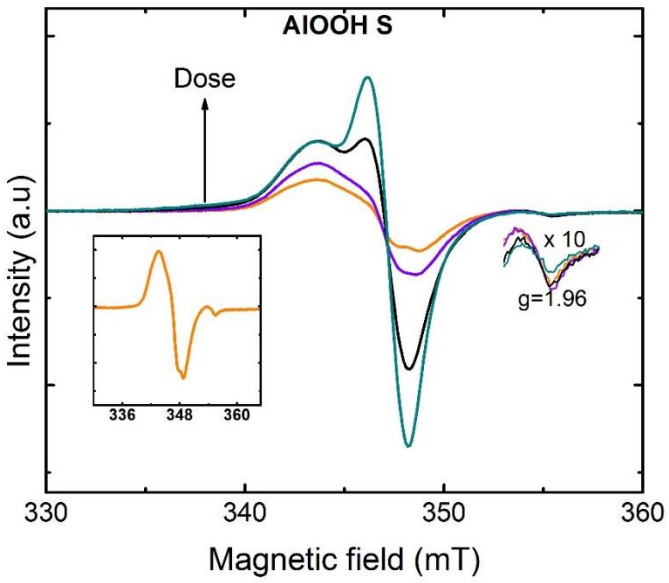

Figure 4.6. EPR spectra of electron irradiated AlOOH S at various doses at RT. Orange: 6.5 kGy, violet: 13 kGy, black: 52 kGy and dark cyan: 130 kGy. The insert presents the subtraction of the spectra recorded at 130 kGy and 52 kGy.

The simulation of the EPR spectra corresponding to the lower dose is presented in Figure 4.7. The characteristics of the broad component are: $g_x = g_y = 2.024$, $g_z = 2.0034$ and $\Delta H_{pp}^x = \Delta H_{pp}^y = 4.8\, mT$, $\Delta H_{pp}^z = 3.09\, mT$. In the following the broad component is called RID I and the narrow RID II.

Concerning AlOOH L the observations are qualitatively the same except two differences:

- An intense doublet assigned to The EPR spectra of H radicals whose intensity remains almost constant. The concentration of H radicals does not depend on the dose and is estimated to be 3.3 10^{-4} mol/kg approximately,
- A new singlet ($g = 1.998, \Delta H_{pp} = 0.2\, mT$) is observed at high field (see Figure 4.8). This new signal is called RID III in the following.

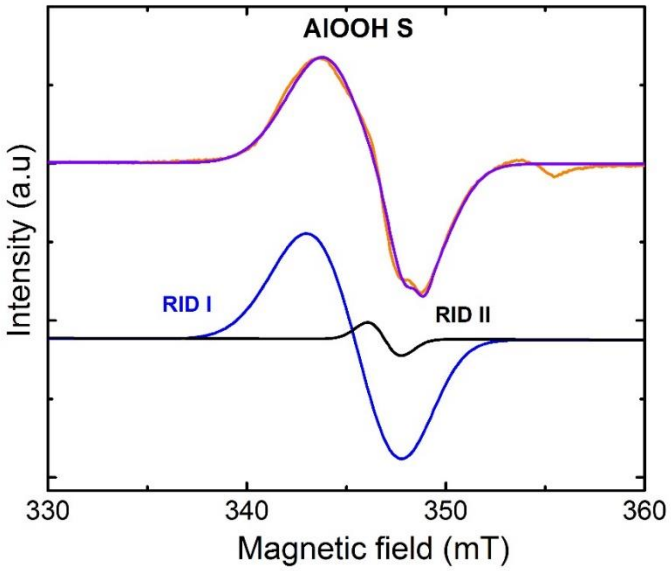

Figure 4.7: Simulation of EPR spectra of electron irradiated AlOOH S at 6.5 kGy. Orange: experimental line, violet: theoretical simulated line, blue line and black line representing RID I and RID II, respectively.

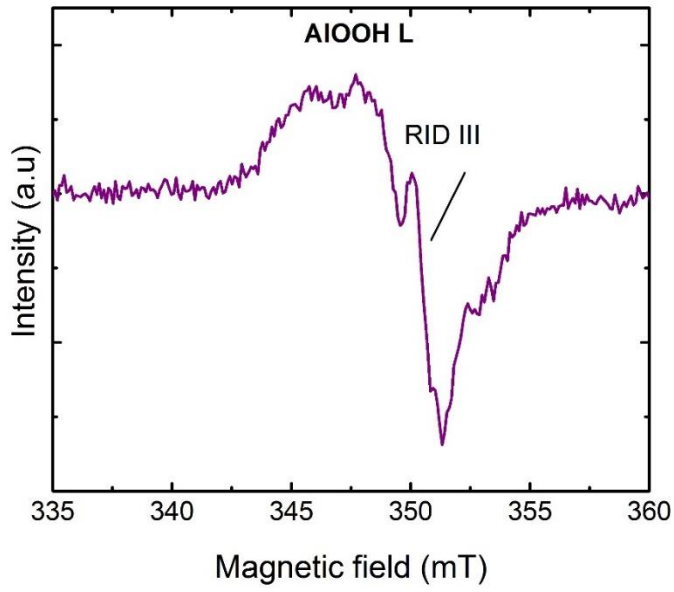

Figure 4.8: EPR of AlOOH L electron irradiated at 6.5 kGy at room temperature. A new defect RID III appears at high field with $g = 1.998, \Delta H_{pp} = 0.2\ mT$.

For both materials the evolution with the dose can be satisfactory described supposing that the spectra are the superposition of the three components defined above. Figure 4.9 and Figure 4.10 represent the evolution of the concentration of RID I, RID II and H

radicals as a function of the dose. A clear difference between these two types of defects is observed: RID I saturates quickly with the dose when RID II accumulates.

The yields of formation of these defects are estimated using the slope at the origin or the data obtained at the lowest dose:

- AlOOH L: $G(RID\ I) = 2.3 \text{ x } 10^{-7}\ mol/J$ and $G(RID\ II) = (7\ \ 0.5) \text{ x } 10^{-9}\ mol\ J$
- AlOOH S: $G(RID\ I) = 1.3 \text{ x } 10^{-7}\ mol/J$ and $G(RID\ II) = 4 \text{ x } 10^{-9}\ mol/J$

In AlOOH L the concentration of RID III is almost constant and equal to 1.7 10^{-4} mol.kg^{-1}.

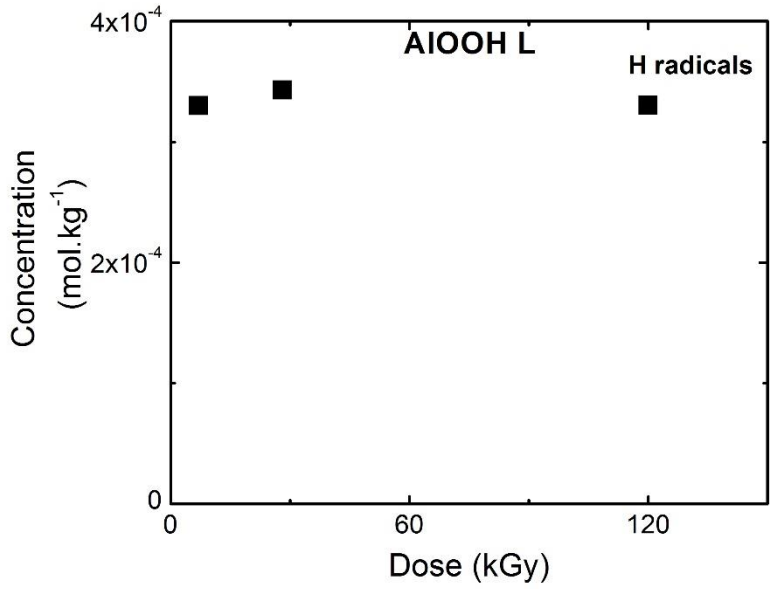

Figure 4.9. Evolution of the concentration of H radicals in electron irradiated AlOOH L as a function of the dose.

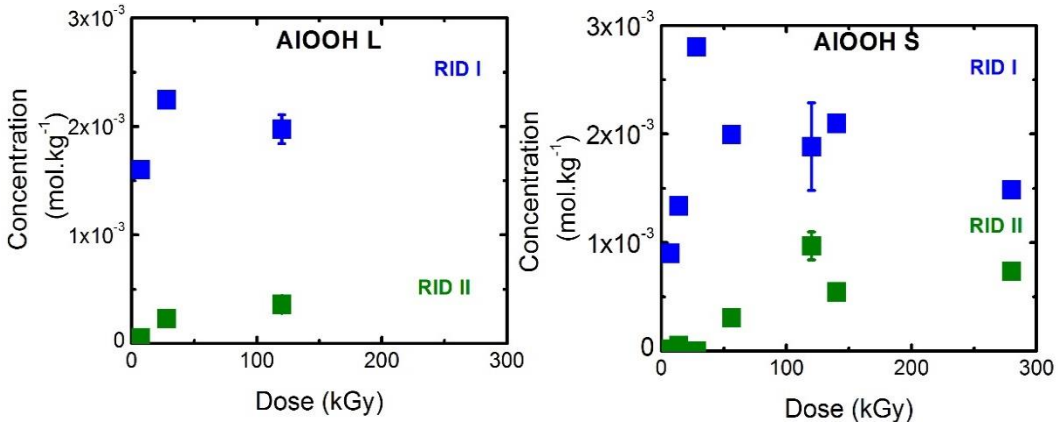

Figure 4.10.Evolution of the concentration of RID I (blue), and RID II (green) in electron irradiated AlOOH L and S as a function of the dose.

4.2.1.2 Room temperature stability

Kinetics were conducted under vacuum in order to study the stability of H radicals and other induced defects as a function of the time. The results are represented in Figure 4.11 and Figure 4.12 for AlOOH L and AlOOH S, respectively. The main difference between these two materials is the stability of H radicals. AlOOH L can stabilize an important concentration of H radicals, after 24 hours the initial H radical concentration decreased by only 22.5% while as mentioned before, no H radicals are seen in the case of irradiated AlOOH S above 10 kGy. View their reactivity, the stability at room temperature of H radicals in AlOOH L are remarkable.

Although all components decreased as a function of time, radiation induced defects were seen to be stable at room temperature.

In Figure 4.11 (left) the spectra of low field H radicals appear to be asymmetric. The high field spectrum is the symmetric point of the low field one. This result suggests either the presence of different components or a hyperfine anisotropy. The hyperfine structure constant is close to that of free H atom, this indicates that the interaction of H with the cation is weak. This result is in accordance with the model proposed by Yurik and al which supposes that H is stabilized near the cation and the hyperfine interaction is determined by the polarizability of the cation. [56]

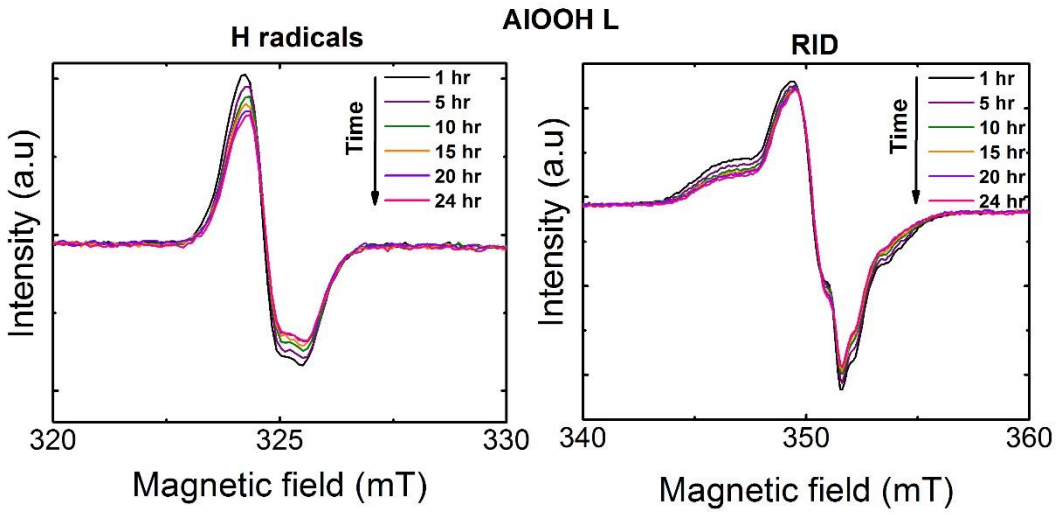

Figure 4.11. Evolution at RT of EPR spectra of electron irradiated AlOOH L at 120 kGy. The evolution of H radicals (on the left) and RID (on the left) are shown as a function of time from one hour until 24 hours.

RID I (broad peak) decreased by 38% after 24 hours at RT in the case of AlOOH L and by 30% in AlOOH S. RID II (narrow peak) was more stable and diminishes by 9.5 % in AlOOH L and by 20 % in AlOOH S.

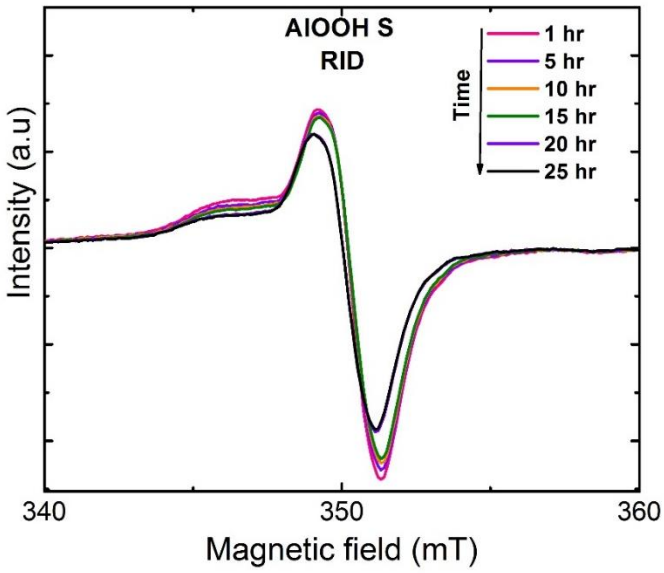

Figure 4.12. Evolution at RT of EPR spectra of electron irradiated AlOOH S at 120 kGy. The evolution of RID is shown as a function of time from one hour until 25 hours.

4.2.1.3 Annealing of defects

Annealing of EPR defects originating from electron irradiated AlOOH S and L at 120 kGy, is shown and discussed in this section.

The evolution of EPR spectra of AlOOH S as a function of temperature is presented in Figure 4.13. On the right, Y scale has been magnified in order to highlight the evolution at the highest temperature. Both defects RID I and RID II decrease in a similar way with temperature. At 200°C, RID II is still observed and disappears above this temperature. RID IV is stable as a function of temperature. Annealing at 200°C and above reveals the presence of an anisotropic signal with $g_z = 2.063$. It is likely that this signal is not created upon annealing. but is only observable when the intensity of other signals has decreased.

Concerning AlOOH L (see Figure 4.14) some differences can be observed: RID I disappeared above 120°C while RID II is more stable. Finally the defect RID III is more difficult to detect at 200°C.

Figure 4.15 shows the EPR spectra of electron irradiated AlOOH S and AlOOH L at 120 kGy after annealing for 1 hour at 300°C. This plot shows the appearance of a new defect (called RID IV) which intensity is close for both materials. The simulation gives the following spin parameters for this new signal: $g_x = g_y = 2.0043$, $g_z = 2.064$ and $\Delta H_{pp}^x = \Delta H_{pp}^y = 2.06\ mT$, $\Delta H_{pp}^z = 4.63\ mT$.

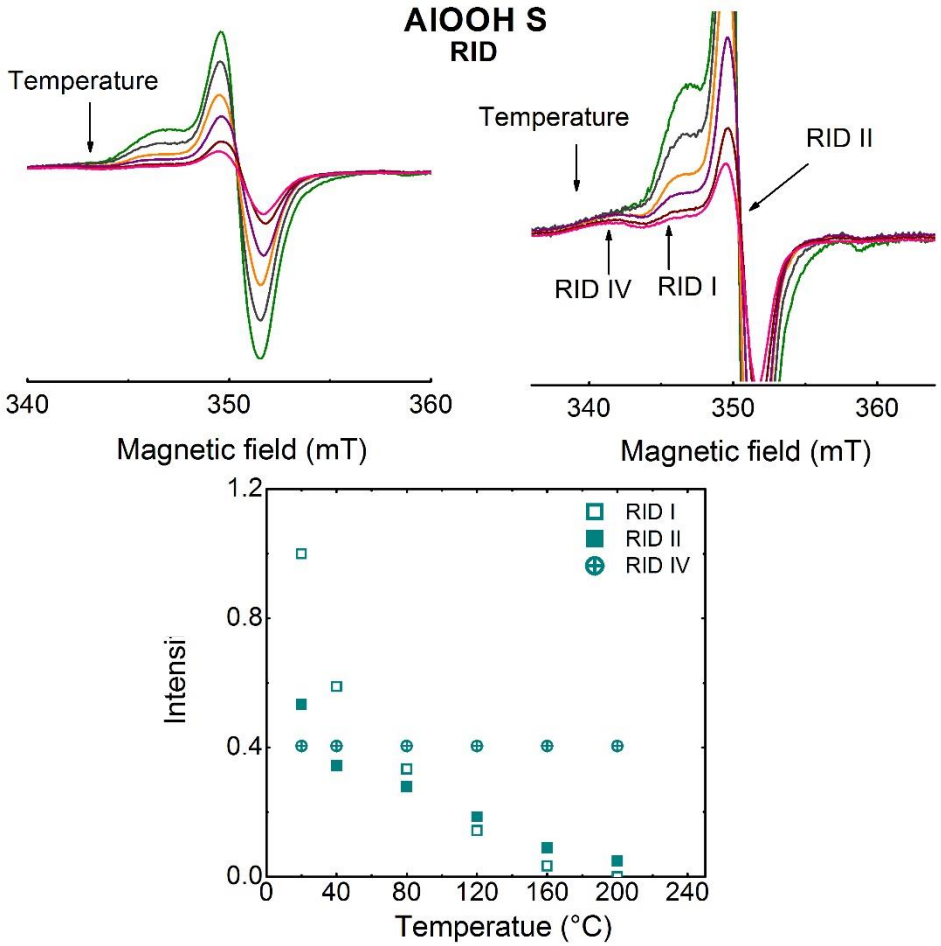

Figure 4.13. EPR spectra (top right and left) and relative intensity (bottom) of electron irradiated AlOOH S at 120 kGy after annealing at different temperatures. EPR are represented as follows: Olive: RT, black: 40°C, orange: 80°C, purple: 120°C, wine: 160°C and pink 200°C.

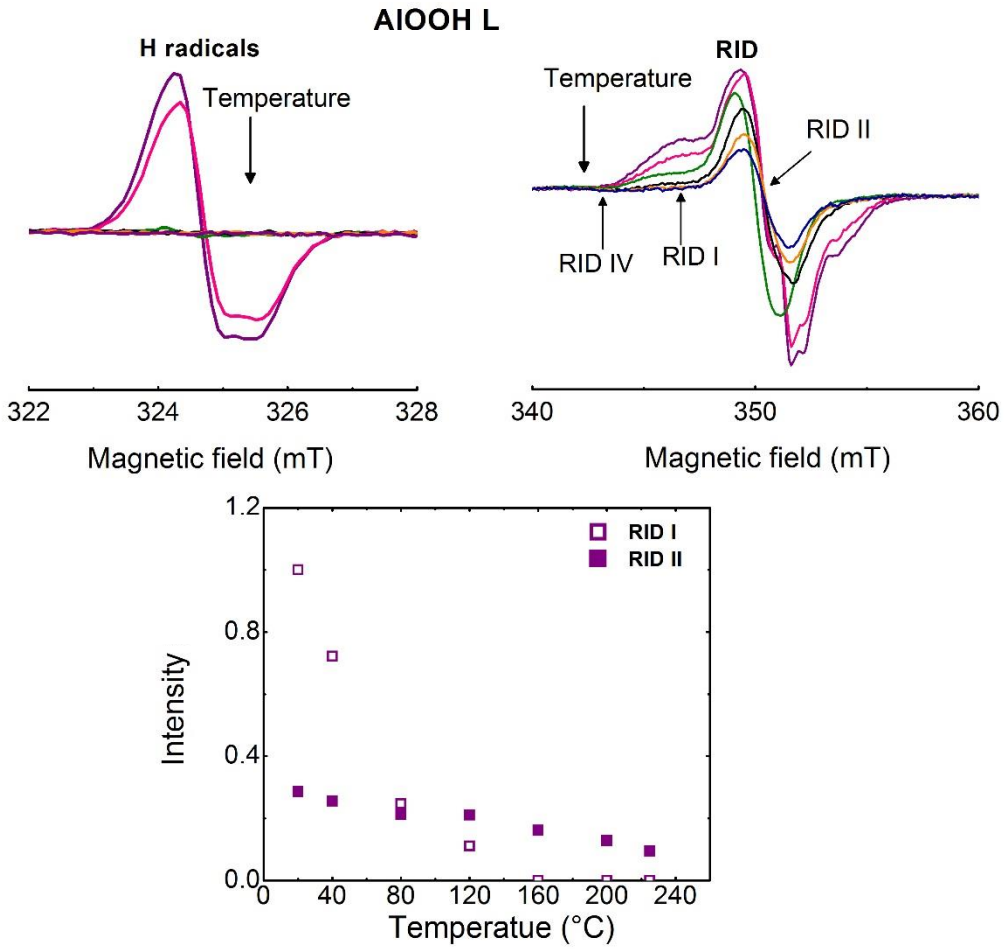

Figure 4.14. EPR spectra (top right and left) and relative intensity (bottom) of electron irradiated AlOOH L at 120 kGy after annealing at different temperatures. EPR spectra are represented as follows: Violet: RT, pink: 40°C, olive: 80°C, black: 120°C, orange: 160°C and purple 200°C.

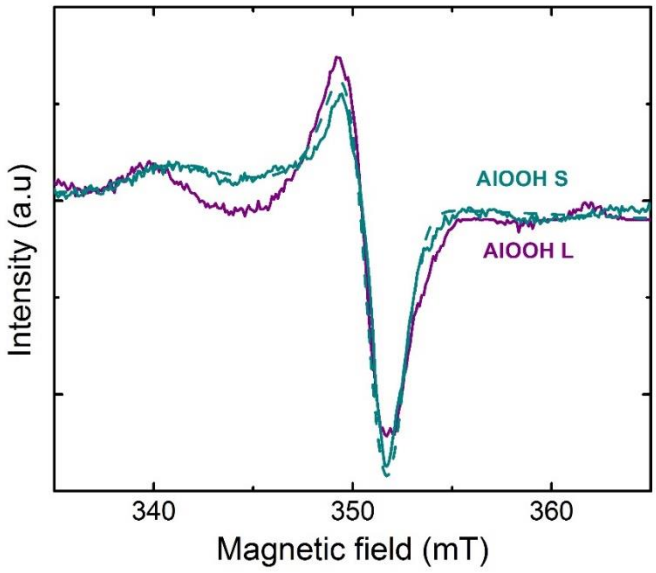

Figure 4.15. Comparison of EPR spectra of AlOOH S (cyan blue) and AlOOH L (purple) after one hour annealing at 300°C. The fit of the annealing spectra of irradiated AlOOH S is shown in dotted cyan blue line.

Next section will be treating in the same way radiation induced defects in $Al(OH)_3$.

4.2.2 Bayerite $Al(OH)_3$

4.2.2.1 Dose effect

Figure 4.16 represents the experimental (full lines) and simulated (dashed lines) EPR spectra of $Al(OH)_3$ irradiated at different doses. Globally the signal remains unchanged whatever the dose is. It is a broad slightly asymmetric singlet. Its spin parameters are:

$g_x = g_y = 2.0030$,

$g_z = 2.0026$ and $\Delta H_{pp}^x = \Delta H_{pp}^y = 4.72\ mT$, $\Delta H_{pp}^z = 3.88\ mT$.

In the first instance we suppose that this defect is related to RID I so it will be called RID I' in the following.

Some very small signals are superimposed on this signal:

- A narrow peak (called RID III') visible only at the lowest dose (7 kGy) has characteristics close to those of RID III: *g* factor of 1.998 and a width of 0.2 mT,
- Above 28 kGy, a signal with a hyperfine interaction called RID VI'.

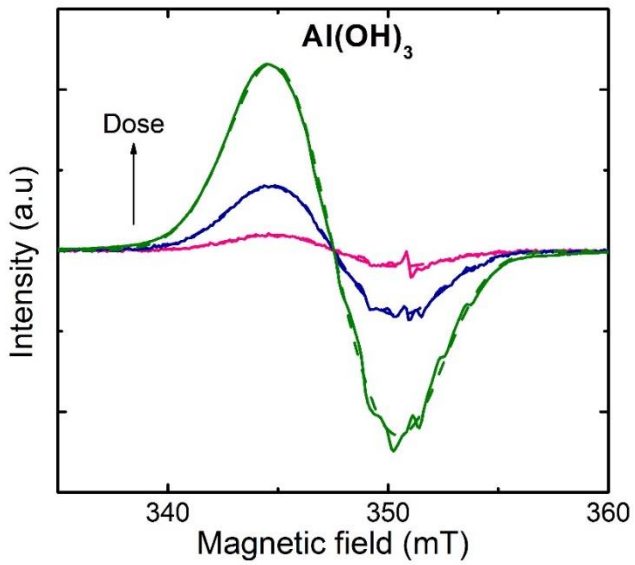

Figure 4.16: Evolution of EPR spectra of electron irradiated $Al(OH)_3$ as a function of the dose. Straight lines represent the experimental data and dotted ones the simulations. Green, blue and pink colors are attributed to 7, 28 and 120 kGy.

Figure 4.17 represents the evolution of the concentration of RID I' and H radicals as a function of the dose in irradiated $Al(OH)_3$. RID I' accumulates with the dose, the estimated radiolytic yield is 3.1 10^{-7} $mol.kg^{-1}$.

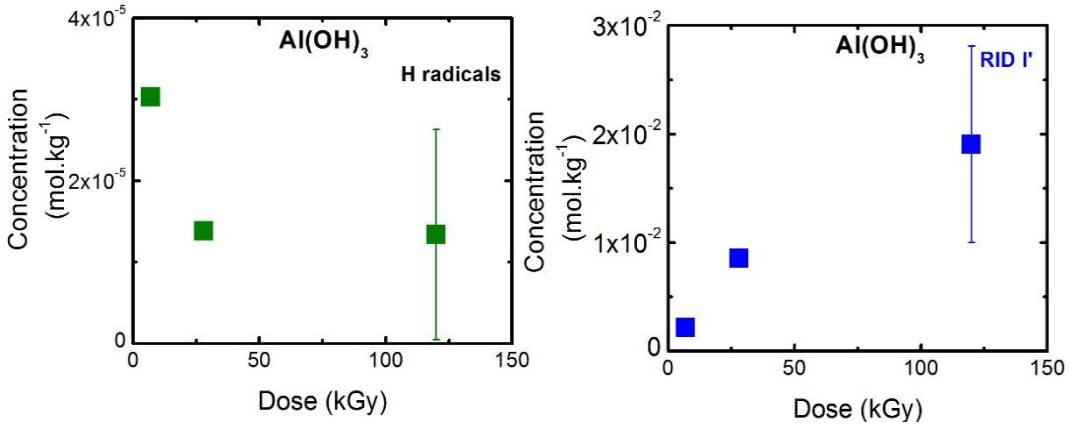

Figure 4.17. Evolution of the concentration of RID I' (right), and H radicals (black) in irradiated $Al(OH)_3$ as a function of the dose.

4.2.2.2 Room temperature stability

The evolution of the EPR spectra as a function of time at room temperature is presented in Figure 4.18.

In $Al(OH)_3$ H radicals are clearly less stable compared to AlOOH L. After 12 hours the signal is hardly detectable. RID I' lost 28.2 % of its initial concentration after 25 hours at room temperature, this value is comparable to that of signal RID I in AlOOH S and AlOOH L. The decrease of the signal is attended by an increase of the hyperfine signal (RID VI').

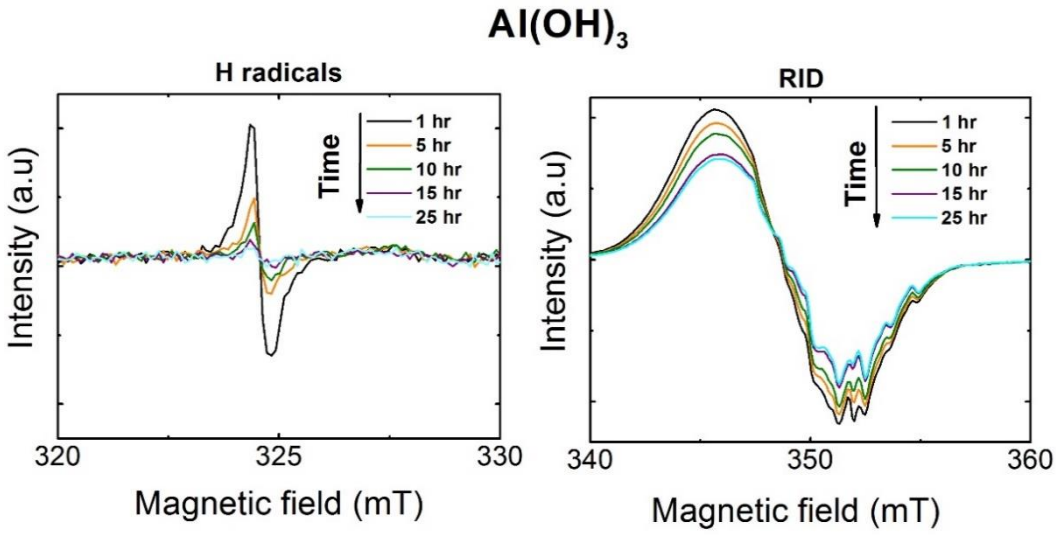

Figure 4.18. Evolution at RT of EPR spectra of radiation induced defects in electron irradiated $Al(OH)_3$ at 120 kGy. The evolution of H radicals (on the left) and RID (on the left) are shown as a function of time from one hour until 25 hours.

4.2.2.3 Annealing of defects

Annealing of EPR defects originating from electron irradiated $Al(OH)_3$ at 120 kGy, is shown and discussed in this section.

Unlike AlOOH, the progressive disappearance of the EPR spectrum assigned to RID is not observed. Above 80°C the signal of RID I' is converted to an axially anisotropic signal (RID V') (Figure 4.19). The conversion is total above 100°C. The hyperfine signal (RID VI') increases until 120°C then it decreases and almost disappears above 200°C. RID I' and the sum of RID II' and V' are plotted as a function of temperature.

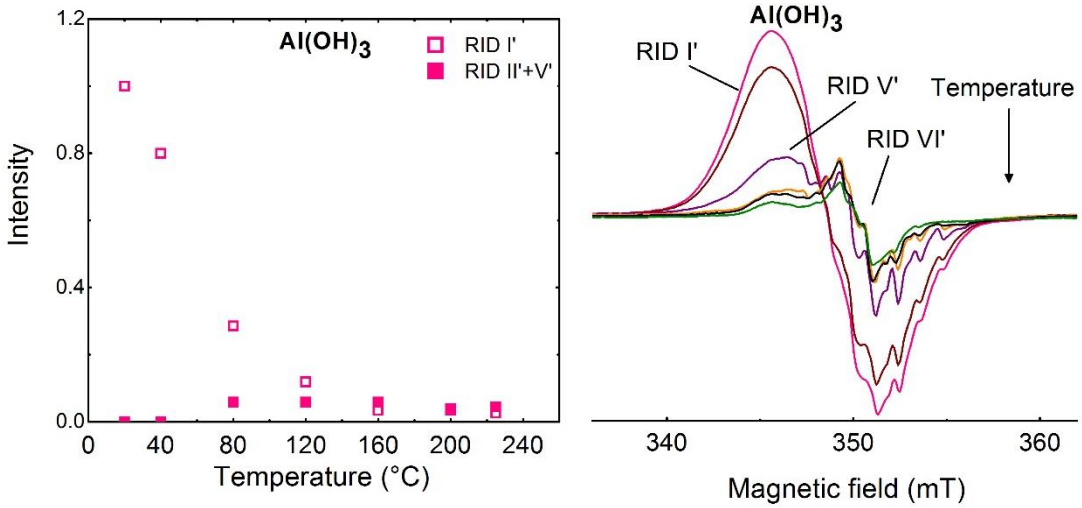

Figure 4.19. EPR spectra (right) and relative intensity (left) of electron irradiated $Al(OH)_3$ at 120 kGy after annealing at different temperatures. EPR spectra are represented as follows: Pink: RT, wine: 40°C, purple: 80°C, orange: 120°C, black: 160°C and olive 200°C.

Figure 4.20 presents the EPR spectrum of electron irradiated $Al(OH)_3$ annealing at 250°C. The simulation reveals besides the signal assigned to RID VI' the presence of narrow singlet with spin parameters close to RID II (see Figure 4.20).

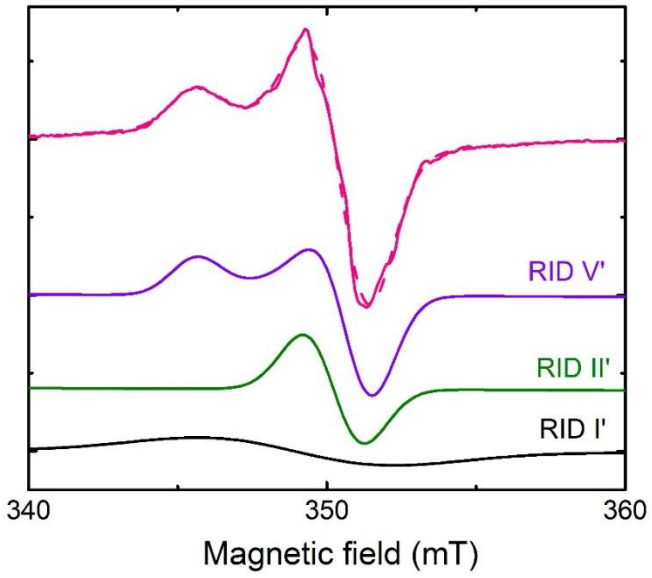

Figure 4.20. EPR spectra of electron irradiated $Al(OH)_3$ at 120 kGy and annealed one hour at 225°C. Straight lines represent the experimental data and dotted ones the simulations. RID I' (black), RID II' (green), and RID V' (violet).

It is noted RID II' in the following. A broad signal was added to fit the wings of the spectrum. This contribution could be attributed to a remaining fraction of RID I'.

Table 4.4 gives the spin parameters of the different components determined by the simulation.

At 300°C, no more defects exist, they were all annealed.

Table 4.4. Spin parameters of RID II' and RID V' determined from the simulation of irradiated $Al(OH)_3$.

	g_x	g_z	ΔH_{pp}^x (mT)	ΔH_{pp}^z (mT)
RID II'	2.009		2.07	
RID V'	2.0037	2.036	1.84	1.66

4.2.3 Defects localization

All the preceding experiments were performed in vacuum. The samples were placed and stored in glass sealed EPR tubes. In order to determine if the defects are located on the surface or not, EPR spectra were recorded after irradiation in controlled atmosphere and after opening the ampules and exposing them to the air. Oxygen can have two effects, firstly it can react with the paramagnetic centers, and secondly it can modify the spin relaxation of nearby paramagnetic centers through a cross relaxation process. The presence of oxygen is generally characterized by an increase of the signal broadening.

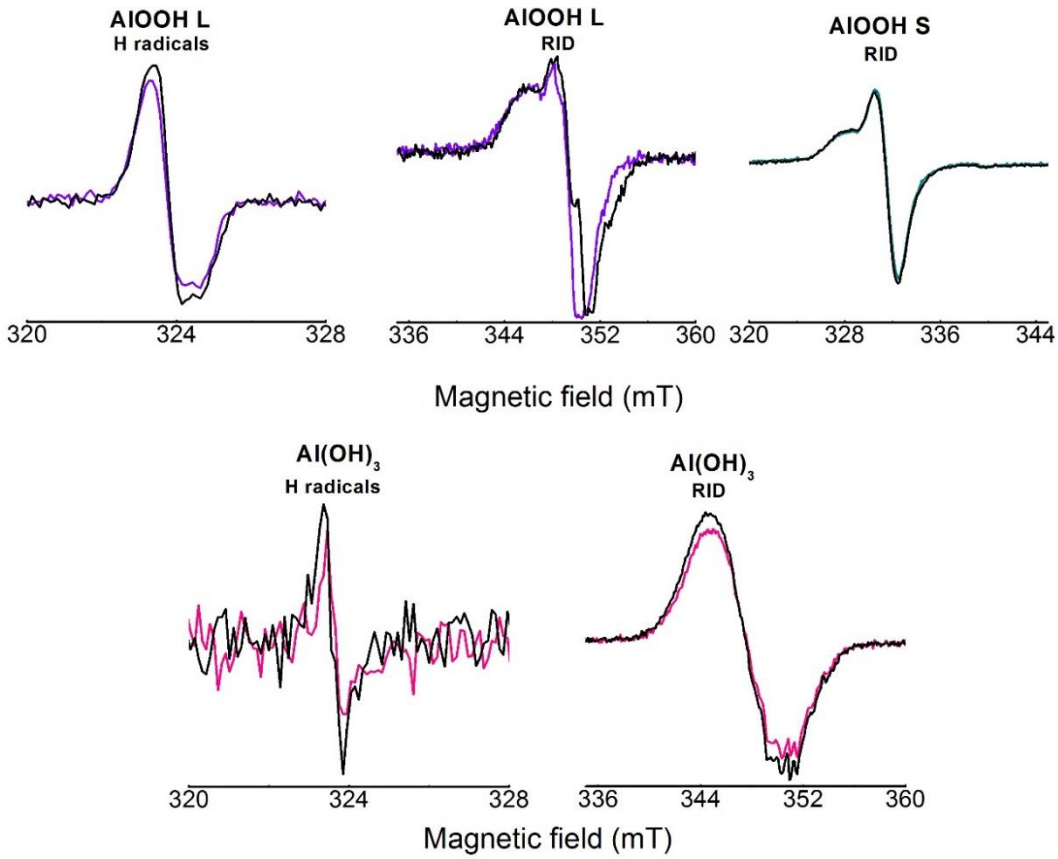

Figure 4.21. EPR spectra of electron irradiated AlOOH S (30 kGy), ALOOH L (30 kGy) and $Al(OH)_3$ (30 kGy) after exposition to air. Black lines represent the spectra under vacuum while colorful lines represent the one exposed to air.

Figure 4.21 compares the stability of H radicals and other radiations induced defects after exposition to air for one hour. The concentration of H radicals remains unchanged when samples were exposed to air. This result leads us to suppose that H radicals reside in the bulk. This was in agreement with the findings of Vedrine and al, where oxygen was introduced over Boehmite, Bayerite and Gibbsite, before and after irradiation and no variation in shape, intensity or behavior of H atoms signals was observed. D_2O exchange experiments were led by this group and no exchange was seen.[64] H atoms were stabilized in the bulk rather in a superficial layer and were inaccessible to any molecules.

Concerning RID, in the case of AlOOH S and $Al(OH)_3$ a slight decrease of the intensities of RID I and RID I' can be observed. One can conclude that the majority of the RID are located in the bulk. The major evolution is the disappearance of RID III in AlOOH L which proves that this center is located at the surface.

4.3 Identification of RID

In this section we discuss the identification of RID on the basis of the spin parameters and thermal stability.

4.3.1 H radicals

The stability of H radicals was distinct from one material to another. In the case of AlOOH S, H radicals were not observed at room temperature. Whereas an important quantity of H radicals remains trapped in AlOOH L after irradiation. In this material H radicals are stable up to 80°C. For $Al(OH)_3$, a much smaller quantity of H radicals is detected and its annealing occurs slightly above room temperature (40°C).

Scholz and Stösser show that the stability of H radicals depends on the existence of symmetrical cages. [67] Moreover trapped species decrease when the disorder increases. Therefore, we conclude that the disorder in AlOOH S (see chapter 2.4.2) explains its lower stabilization of H atom.

4.3.2 RID I

The spin parameters of RID I spectrum are in the range found for oxygen centers observed in irradiated Al_2O_3 or $Al(OH)_3$ (see Chapter 1). It corresponds to O^- ions.
In hydroxides, O^- centers can be formed from the homolytic dissociation of the O-H bond:

(37)

$$Al \cdots OH^- \rightarrow Al \cdots O^- + H$$

It could also be produced by reaction of OH :

(38)

$$OH^- \rightarrow OH + e^-$$

(39)

$$OH^- + OH \rightarrow O^- + H_2O$$

We don't have an evidence of the presence of OH since it is not observable by EPR. In Boehmite O^- center can also be associated to O^{2-}. The proposed formation mechanisms are:

(40)

$$Al \cdots O^{2-} \cdots Al + hole \rightarrow Al \cdots O^-$$

In this case the defect needs a cationic defect (vacancy or impurity) as a charge compensator (to maintain a charge balance in the lattice). Iron impurity can be a good candidate. Using Kröger-Vink notation, the possible reactions can be written as:

(41)

$$Fe_{Al}^x + O_O^x \rightarrow \left(Fe_{Al}O_O\right)^x$$

The defect $\left(Fe_{Al}O_O\right)^x$ can be also written [O^- Fe^{2+}] following Stoneham notation.

This hypothesis could appliy to AlOOH L. Actually, in this material, the maximal concentration of RID I centers (2 x 10^{-3} mol/kg) is close to the iron concentration measured by ICP-MS (section 3.3.1) which has been estimated to be 1.2 x 10^{-3} mol/kg. Moreover EPR spectrum of pristine AlOOH L demonstrates an intense signal of Fe^{3+} ions.

This attribution is ruled out by different observations:

- Iron concentration is lower in AlOOH S while the maximum concentration of RID I centers is close to those measured in AlOOH L,
- The concentration of Fe^{3+} ions is much weaker in AlOOH S,
- The disappearance of the Fe^{3+} EPR signal at high dose in AlOOH was not observed, with only a 30% loss for a dose of 140 kGy for AlOOH L is observed.

In summary, it is concluded that RID I corresponds to O^- centers resulting from the homolytic dissociation of OH^- ion.

4.3.3 RID I'

The spin parameters of RID I' are close to those found for RID I. The anisotropy is slightly more important for RID I'. Table 4.5 compares the g-factor and the splitting Δ for both centers. The spin-orbit coupling λ of O^- is supposed to be equal to -0.017 eV.

Table 4.5. Comparison of g-factors and splitting Δ in irradiated AlOOH and $Al(OH)_3$.

	g_z	g_x	**Δ** (eV)
AlOOH	2.0034	2.024	1.57
$Al(OH)_3$	2.0026	2.030	1.23

In $Al(OH)_3$, the concentration of O^- center at room temperature is almost one order of magnitude higher than in AlOOH. This difference suggests that defects are more stable in the hydroxide.

The formation yield of defects in $Al(OH)_3$ is surprisingly high ($>2.10^{-7}$ mol/J) which proves that the cleavage of the O-H bond is the major radiolytic event.

4.3.4 RID II

It is tempting to assign RID II to another O^- center in another site of stabilization. Then it could be attributed to a hole center stabilized on an oxygen O^{2-} adjacent to an impurity. As the RID II concentration is much weaker than the RID I concentration, the preceding arguments used to demonstrate that RID I center is not associated with an iron impurity, no longer apply.

Nevertheless the characteristic of the signal seems incompatible with an O^- center. Indeed the signal should have an axially symmetry g factor (see Chapter 1). An isotropic signal is not excluded if $\Delta \gg \lambda$. But in this case, the average g factor should be close to 2.0023. Then it is concluded that **RID II is not an O^- center.**

Steinike and al. reported the formation of a singlet with $g = 2.012$ in mechanical treated hydrargilite, a polymorph of $Al(OH)_3$.[54] Although the poor quality of the Figures, some similarities can be founnd between RID II signal and the signal reported by Steinike et al. The authors assigned this center to ozonide radical O_3^- formed by reaction of O_2 with O^-:

(42)

$$O_2 + O^- \rightarrow O_3^-$$

Ozonide radical was also observed in Barium hydroxides[59] and in different oxides such as quartz.[121]

The following reactions have been also proposed:

(43)

$$O_2^- + O^- \rightarrow O_3^- + e$$

(44)

$$O_2^{2-} + O_2^- \rightarrow O_3^- + O^{2-}$$

This radical can be produced by dissociation of O_2:

(45)

$$O_2 \rightarrow O + O$$

(46)

$$O + O_2 \rightarrow O_3$$

(47)

$$O_3 + e \rightarrow O_3^-$$

The attribution of RID II to an ozonide radical, is questionable because the spin parameters of the radicals depend little on the host matrix (see Chapter1). Then the signal should appears as asymmetric singlet with $g_z = 2{,}015 - 2{,}017$. The isotropic character and the narrowness of the signal seem incompatible with the attended anisotropic g-factor for O_3^- except if we suppose an averaging by motion, for example, a rapid rotation inside a cage. This hypothesis should be investigated, for example, by comparing EPR spectrum at 77 K or at 4.2 K with the spectrum recorded at room temperature.

4.3.5 RID III and RID III'

Classically, g factors smaller than that of the free electron are attributed to electrons centers [122-123,124]. The adsorption of O_2 from air leads to the decrease of RID III signal. These observations enable us to attribute the spectra to electrons captured by surface anionic vacancies (an F_S center).

There is a major difference between AlOOH L and the others materials. The concentration of RID III centers in AlOOH L is almost constant whatever the dose is while they are only observed at the lowest dose as a very weak singlet in the case of $Al(OH)_3$ and AlOOH S. The lack of F_S centers in these materials can be attributed either

to a low concentration of anionic vacancies or to the presence of efficient electron scavengers.

4.3.6 RID IV

This signal is observed after the thermal decay of RID I and RID II centers ion AlOOH. In the case of AlOOH S where RID IV is clearly visible from 80°C. The large anisotropy of the RID IV signal permits to assign this signal to O_2^- centers which is generally associated with the recombination of O^- centers followed by hole trapping:

(48)

$$Al \cdots O^- + Al \cdots O^- \rightarrow Al \cdots O_2^{2-} \cdots Al$$

(49)

$$Al \cdots O_2^{2-} \cdots Al + \ hole \rightarrow Al \cdots O_2^- \cdots Al$$

The observation of O_2^- centers supports the formation of ozonide radicals because it is a precursor of this radical (see section 4.3.4).

4.3.7 RID V'

RID V' replaces RID I' above 80°C. Although the anisotropy is different from those of RID IV it is compatible with an O_2^- center. The decrease of its anisotropy demonstrates an increase of the splitting δ and as a consequence an increase of the crystalline field (see Chapter 1).

4.3.8 RID VI'

RID VI' is characterized by its 11 lines resulting from a hyperfine structure from two Al^{3+} nuclei and is supposed to be $Al \ldots O^- \ldots Al$ described by Kuruc et al in aluminum hydroxide samples described in section 1.5.4.

4.4 Discussion

On the basis of the previous results, the mechanisms of hydrogen production are discussed in this section. The main results are summarized in Table 4.6

In situ FTIR were conducted from 25°C to 220°C, the last temperature we could attend using our annealing system. No differences in peak widths were seen so we can assume that no significant structural evolution could be detected.

From the discussion above, O^- radical ions with a different immediate environement and atomic hydrogen are pronominally formed from the radiolysis of AlOOH and $Al(OH)_3$.

As seen in this chapter, two types of H_2 were quantified: H_2 released at room temperature will be called $H_{2\ released}$ and H_2 quantified above RT after annealing will be called $H_{2\ detrapped}$.

The ratio of $H_{2\ detrapped}$ to $H_{2\ released}$ and the quasi absence of hydrogen production at RT for AlOOH S points out that the diffusion of H_2 cannot explain our results. This led us to think that the two types of H_2 don't have the same formation site or pathway. The yields of formation of O^- centers suggest that the H_2 (RT) can be formed from the general mechanism of homolytic dissociation of OH considered as the dominant radiolytic event:

$$Al\ldots OH^- \rightarrow Al\ldots O^- + H \quad \textbf{(50)}$$

Then H° is certainly the precursor of H_2. This radical can react with $Al\ldots O^-$, recombines with another H radical or be trapped at the structure:

$$Al\ldots O^- + H \rightarrow Al\ldots OH^- \quad \textbf{(51)}$$

$$H + H \rightarrow H_2 \quad \textbf{(52)}$$

$$H \rightarrow H_{trapped} \quad \textbf{(53)}$$

Even in AlOOH L where the trapping is efficient, only a small fraction of the primary H radicals are trapped. Taking into account the relative high concentration of O^- center measured at RT, we suppose the recombination with $Al\ldots O^-$ is limited.

Molecular H_2 released at room temperature may be the result of the recombination of unstable H radicals that are formed and recombined during the irradiation or directly before.

$$H + H \rightarrow H_{2\ released} \quad \textbf{(54)}$$

This molecular hydrogen shows a dependence on particle size: in the small sized sample almost no H_2 was released at RT and one can suppose that in this case H radicals are formed in separate particles or crystals and can't encounter.

We suppose also that $H_{2\,released}$ is formed near the surface. Mobile H° are produced in the bulk and diffuse to the surface where they react to produce hydrogen which enters in the gas phase.

Though not all the H° formed recombine and are quantified as $H_{2\,released}$. Some H radicals may be also trapped in the system and needs thermal activation to recombine with other species or to diffuse to the surface. Therefore one can suppose this mechanism:

(55)

$$2H_{trapped} \xrightarrow{heat} H_{2\,detrapped}$$

This mechanism could not be the only one producing $H_{2\,detrapped}$ in AlOOH S and $Al(OH)_3$ because the concentration of trapped H radicals in these materials is zero or close to zero while the quantity of hydrogen released is significant. Even in the case of AlOOH L, this mechanism is not efficient. Indeed by comparing the quantity of H_2 occluded and H radicals (see Table 4.6) it is clear that **trapped H radicals can't be the only precursor of $H_{2\,detrapped}$.**

A third reaction may be occurring analogous to the recombination of hydrated electron in liquid water:

(56)

$$F_S + F_S \rightarrow H_2$$

The concentration of F_S centers (RID III and RID III') is not sufficient to take account of the production of $H_{2\,detrapped}$.

Finally we suppose that hydrogen is trapped in its molecular form. Schematically we can propose the following reaction:

(57)

$$H + H \rightarrow H_{2\,trapped} \xrightarrow{heat} H_{2\,detrapped}$$

It has to be considered also that not all species formed were detectable using EPR, unfortunately no direct proof of $H_{2\,trapped}$ inside the material has been determined since it has a low concentration (we tried to conduct RAMAN spectroscopy and

dissolution)as well as neutron diffraction (this latter was not achieved until the end and it may give interesting information).

Previously the absence of $H_{2\ released}$ for AlOOH S was attributed to crystallites size that is too small and hinders the recombination of H radicals created in different crystallites. Finally this leads us to suppose that another mechanism exists:

$$H \quad + Al \cdots OH^- \rightarrow Al \cdots O^- + H_{2\ trapped} \tag{58}$$

$$H_{2\ trapped} \xrightarrow{heat} H_{2\ detrapped} \tag{59}$$

This mechanism is seen in organic systems where H radical attacks the organic molecule and forms H_2 :[125]

In liquid water, this reaction was not described to occur at room temperature, though it has been described in gas phases and in water at high temperature.

The next interrogation is to understand if the quantity of $H_{2\ detrapped} + H_{2\ trapped}$ represent the totality of the hydrogen formed by irradiation.

Our overall observations lead us to propose that hydrogen comes mainly from the dissociation of OH^-:

$$2\ OH^- = 2\ O^- + H_{2\ trapped} \tag{60}$$

The balance of the reaction suggests that $G(O^-)$ should be close to $G(H_{2\ detrapped})\ G(H_{2\ trapped})$. This is far from being the case. Then we suppose that the above reaction is reversible. Thus upon heating O^- centers can react with $H_{2\ trapped}$. Then $H_{2\ detrapped}$ represents the fraction of trapped H_2 that did not react with O^- centers. If we suppose that 1 molecule of H_2 if formed for 2 O^- centers, then the detrapped hydrogen accounts only for 5 or 10% of the trapped hydrogen. Moreover, the release of H_2 visible above 200°C proves that H_2 resulted from the fractions that didn't react reversibly with O- dince above this temperature these O^- have disappeared.

Table 4.6. Radiolytic yields of molecular hydrogen and radiation induced defects in irradiated samples at low doses. Molecular yields of radicals are also presented and are attributed to each radical introduced in the paragraph before.

	Molecular hydrogen yield (mol/J)		Radicals yield at RT (mol/J)		Concentration (µmol/kg)	
	Gaseous RT x 10^{-8}	**Occluded x 10^{-8}**	**G (O^-) x 10^{-8}**	**G (O_3^-) x 10^{-8}**	**H**	**F center**
AlOOH L	0.5 ± 0.2	1.2 ± 0.9	23	0.7	330	100-170
AlOOH S	(0-0.04) ± 0.02	0.4 ± 0.1	13	0.4	0-3	0-2
$Al(OH)_3$	0.21 ± 0.05	0.7 ± 0.1	31	-	4-30	0-3

5. Chapter 5: Molecular hydrogen production from hydrated aluminum hydroxide and oxyhydroxide

This chapter aims to clarify the effect of adsorbed water on molecular hydrogen production. Similarly to what have been done in the previous chapter, this section takes into consideration the effect of structure and particle size on the molecular hydrogen production. Radiolytic yields as a function of water uptake (see hydration section 2.1.2) are determined. The study of electron paramagnetic defects by EPR spectroscopy will be detailed in section 5.2.

5.1.1 H_2 production

As explained in Chapter 2 (Chapter 2), samples of AlOOH and $Al(OH)_3$ were hydrated into desiccators where relative humidities of 11, 44 and 76% at room temperature were maintained using saturated salt solutions. Ampules were also used to hydrate samples without exposing them to air. The samples have been irradiated using gamma rays at low dose rate and high energy electron at high rate. The results will be presented and discussed with respect to the amount of sorbed water.

5.1.2 Gamma rays

The production of H_2 from samples hydrated at 11, 44 and 76% RH and irradiated using gamma rays at a dose ranging between 6 and 26 kGy is proportional to the dose except for $Al(OH)_3$ at 44% RH. New experiments are in progress to verify this specific point meanwhile the data have been ignored. The radiolytic yields deduced from the slope of the different curves are resumed in Table 5.1. Each gamma test was done on a separate sample, no cumulated H_2 was measured here, and the uncertainties considered are that related to experimental errors.

At 76% RH hydrogen production increases in the order:

$$AlOOH\ S > AlOOH\ L > Al(OH)_3.$$

Table 5.1. Hydrogen radiolytic yields released from Gamma irradiated samples hydrated at 11, 44 and 76% at room temperature.

		11% RH	44% RH	76% RH
AlOOH L	**$G(H_2)$ mol/J x10^{-8}**	1.3 ± 0.4	2.1 ± 0.1	3.5 ± 0.8
AlOOH S		2.2 ± 0.2	2.6 ± 0.4	4.5 ± 0.3
$Al(OH)_3$		1.2 ± 0.7	-	1.3 ± 0.6

5.1.3 Electron beam irradiation

5.1.3.1 Molecular hydrogen production at room temperature

For all materials, a linear production of H_2 is observed with the dose for 11, 44% and 76%. Figure 5.1 gives an example of molecular hydrogen production from hydrated AlOOH S. Radiolytic yields are presented in Table 5.2.

The water uptakes and the corresponding number of water layers (WL) are also recalled in Table 5.2 considering 0.28 g/m^2 as one water molecule surface (see section 2.1.2).

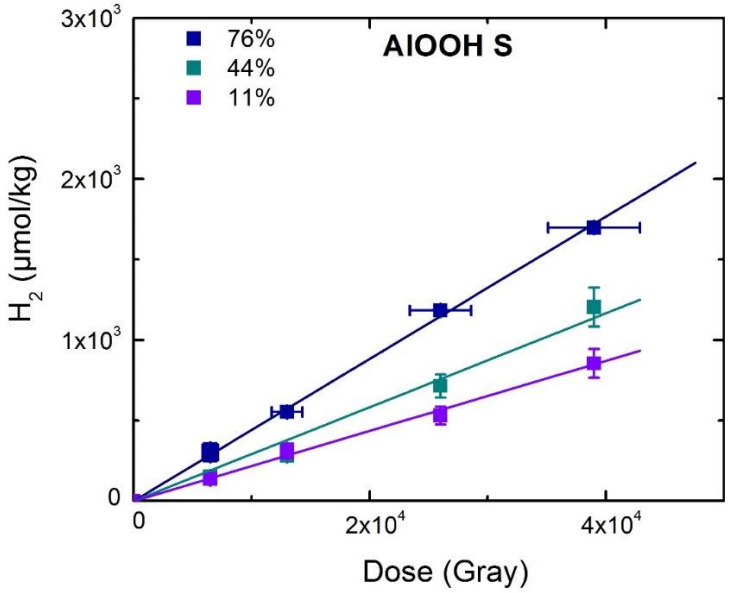

Figure 5.1. Dose dependence of H_2 production for hydrated AlOOH S equilibrated in different relative humidity at room temperature (11, 44 and 76 % RH).

Table 5.2. Hydrogen radiolytic yields with respect to percent water loading from hydrated AlOOH L, S and $Al(OH)_3$ under electron irradiation.

Error bars on water uptake ranged between 8% for AlOOH L, 9% for AlOOH S and 15% for $Al(OH)_3$.

		Desiccator			Ampules		
		11% RH	44% RH	76% RH	11% RH	44% RH	76% RH
AlOOH L	**Water uptake**	0.60 ± 0.05	1.30 ± 0.10	1.10 ± 0.08	0.050 ± 0.004	0.38 ± 0.03	1.58 ± 0.13
	WL	0.52	1.13	0.96	0.04	0.33	1.38
	$G(H_2)$ mol/J x 10^{-8}	8 ± 1.0	8.2 ± 1.0	7.6 ± 0.2	5.9 ± 0.06	7.2 ± 0.4	7.0 ± 0.6
AlOOH S	**Water uptake**	3.80 ± 0.34	7.40 ± 0.66	17.42 ± 1.56	1.3 ± 0.1	4.5 ± 0.4	14.2 ± 1.3
	WL	0.51	0.99	2.32	0.17	0.60	1.90
	$G(H_2)$ mol/J x 10^{-8}	2.2 ± 0.1	2.6 ± 0.4	4.5 ± 0.3	2.7 ± 0.1	3.6 ± 0.2	6.7 ± 1.2
$Al(OH)_3$	**Water uptake**	0.34 ± 0.05	0.42 ± 0.06	0.50 ± 0.07	0.17 ± 0.02	0.36 ± 0.05	0.78 ± 0.12
	WL	0.11	0.14	0.16	0.05	0.11	0.25
	$G(H_2)$ mol/J x 10^{-8}	1.0 ± 0.1	1.1 ± 0.8	2.6 ± 0.8	0.51 ± 0.09	0.41 ± 0.01	0.55 ± 0.02

Concerning hydrogen production, no big differences were seen between the three hydrated AlOOH L.

The variation of $G(H_2)$ as a function of the water loading is presented in Figure 5.2, Figure 5.3 and Figure 5.4 for the different materials. For comparison, the primary yield for liquid water $G^{water}(H_2)(= 4.5\ 10^{-8}\ mol/J)$ is indicated as well as the expected variation of $G(H_2)$ following the additive law if there was no interaction between water and the material. The additive law is given by the relation:

$$G^{hydrated} = (1 - \omega_{water}).G^{dry} + \omega_{water}.G^{water}(H_2)$$

ω_{water} is the weight fraction of water and G^{dry} is the yield of the dry material.

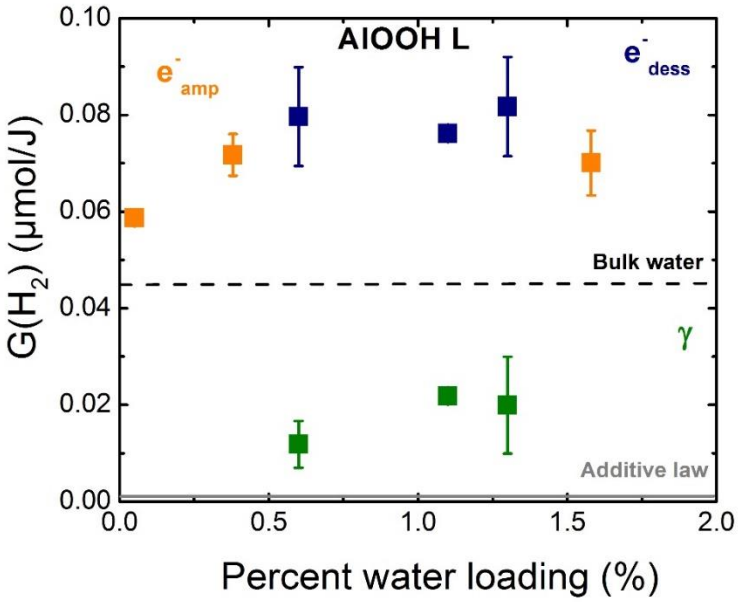

Figure 5.2. Hydrogen production from AlOOH L with respect to water loading. Blue squares (electron irradiations of desiccator hydrated samples), orange dots (electron irradiations of ampule hydrated samples), green squares (gamma irradiations of desiccator hydrated samples). Black dotted line (primary radiolytic yield of liquid water) and gray continuous line (additive law see text).

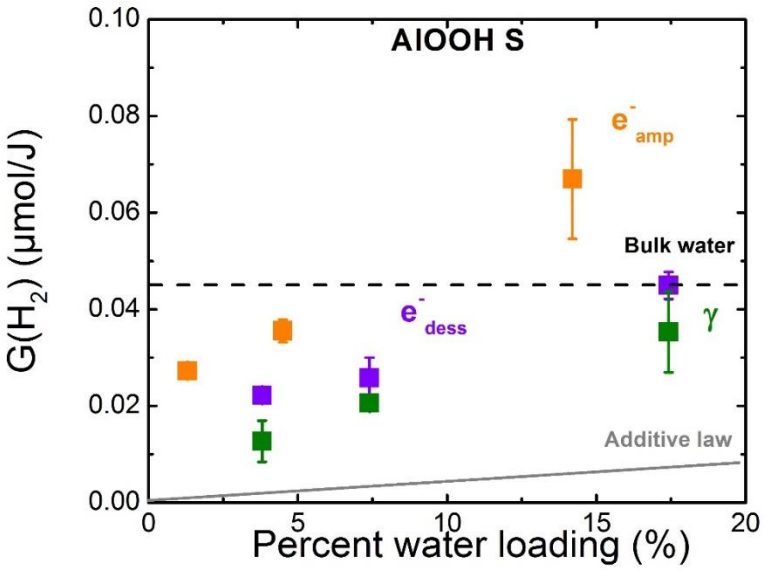

Figure 5.3. Hydrogen production from AlOOH S with respect to water loading. Purple dots (electron irradiations of desiccator hydrated samples), orange dots (electron irradiations of ampule hydrated samples), green dots (gamma irradiations of desiccator hydrated samples). Black dotted line (primary radiolytic yield of liquid water) and gray continuous line (additive law see text).

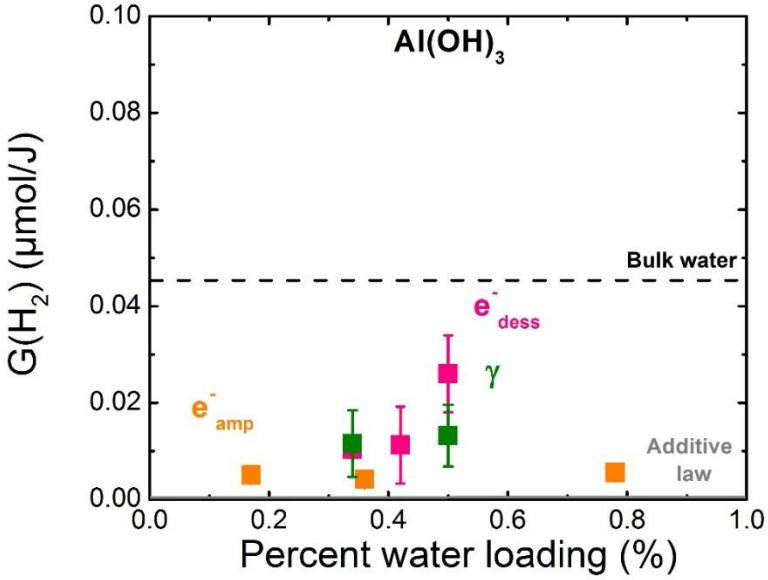

Figure 5.4. Hydrogen production from $Al(OH)_3$ with respect to water loading. Pink dots (electron irradiations of desiccator hydrated samples), orange dots (electron irradiations of ampule hydrated samples), green dots (gamma irradiations of desiccator hydrated samples). Black dotted line (primary radiolytic yield of liquid water) and gray continuous line (additive law see text).

From Figure 5.2, it is noticeable that for AlOOH L, $G(H_2)$ is constant whatever the water uptake is and that a big difference exists between results obtained from electron and gamma irradiations. This latter irradiation type shows lower values by a factor

ranging between 3 and 8. This may be due to back reactions during the long irradiation periods. The yields achieved in electron irradiations are surprisingly high.

From Figure 5.3, a linear dependence of $G(H_2)$ as a function of water uptake is seen for ALOOH S. Moreover there is almost no difference between electron and gamma results.

Comparing AlOOH L and AlOOH S irradiated with electrons, it is obvious that hydrogen production is not directly related to the amount of adsorbed water. In fact, although the water uptake is almost one order of magnitude higher for AlOOH S compared to AlOOH L, $G(H_2)$ is lower for this material.

Concerning $Al(OH)_3$ the dispersion is higher especially for gamma irradiation. Whatever the irradiation or hydration conditions are, this material presents always the lower yields.

Radiolytic yield of H_2 from AlOOH L was higher than that of water. Whatever the material is, $G(H_2)$ is greater than the additive law. Both components interact deeply.

5.1.3.2 Trapped Molecular hydrogen

Annealing was conducted on hydrated samples in order to see if any molecular hydrogen is released.

The protocol was analogous to those used for dry samples (annealing samples from 25 to 500˚C), though hydrated samples were more complicated to anneal since care should be taking while preparing the vacuum. In fact, annealing adsorbed nanoparticles may be dispersed which avoid a tight sealing when analyzing.

The results were that no H_2 was released from hydrated AlOOH L and $Al(OH)_3$. These experiments could not be performed on AlOOH S since dispersion of the powder could not be avoided during annealing.

To sum up, unlike dry samples, **gas released at room temperature from hydrated samples represents apparently the whole H_2 formed under irradiation.**

5.1.4 Swift heavy ion irradiations

The effect of adsorbed water on samples irradiated using heavy ions is discussed in this section. Only 76 % hydrated samples were irradiated with Ar^{18+} heavy ions (see Chapter 2.3.3). The results are presented in Figure 5.5. The radiolytic yields deduced from these data are:

- AlOOH S released the highest H_2 quantities and had a radiolytic yield of $(7.3 \pm 0.2) \times 10^{8}$ mol/J, AlOOH L released $(4.3 \pm 0.4) \times 10^{-8}$ mol/J

- $Al(OH)_3$ released the lowest quantities (0.80 ± 0.04) $x10^{-8}$ mol/J. Care should be taken to all the molecular hydrogen quantified under heavy ions irradiations. Samples were held few months before being analyzed in order to be deactivated.

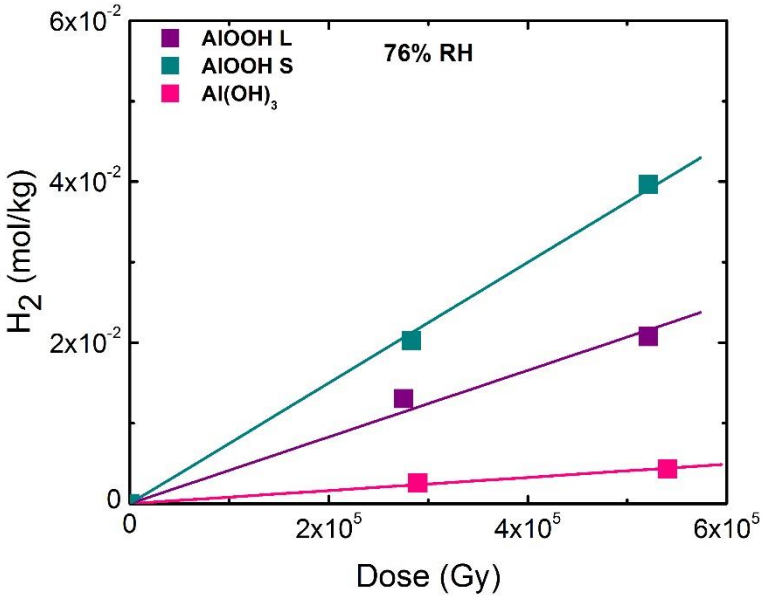

Figure 5.5. Hydrogen production from 76% hydrated Ar^{18+} irradiated aluminum hydroxides and oxyhydroxides as a function of the dose.

At 76% RH, AlOOH L released 5 times more hydrogen and $Al(OH)_3$ three times than dry samples, these quantities were due to energy transfer between the solid and adsorbed water.

These experiments have to be repeated in order to verify these values but time was not enough to book another irradiation session.

A study as a function of time is essential as well as a function of the dose to understand the mechanism of hydrogen production under heavy ions from our samples.

In the next section, radiation induced defects are studied.

5.2 Radiation induced defects

5.2.1 Bohemite AlOOH

5.2.1.1 Trapped defects in Boehmite at 77 K

In order to reduce the reactions of recombination of defects created by irradiation, the materials were irradiated at 77 K. The EPR spectra of irradiated AlOOH S and AlOOH L using electron beams at 46 kGy are given in Figure 5.6. For both material RID I, RID II and H radicals are identified.

In order to reduce the reactions of recombination of defects created by irradiation the materials were irradiated at 77 K. The EPR spectrum of AlOOH S and AlOOH L electron irradiated at 46kGy are given in Figure 5.6. For both materials RID I, RID II and H radicals are identified. Only the relative intensities of the signals are different. We must also notice that No F centers were observable in both samples.

RID signals are proportional to the dose within experimental uncertainties whereas the concentration of H radicals is stationary. This result shows that H radicals are not stable and react even at 77 K. The yields of defects formation are resumed in Table 5.3. As the yields of defects creation are very close in both materials, we can conclude that particle size and impurities have little impact on primary defects production. The RID yields are also very high close to the maximum yield of electron-hole pair formation (see Chapter 2).

No F centers were seen at 77 K. Check Appendix B.

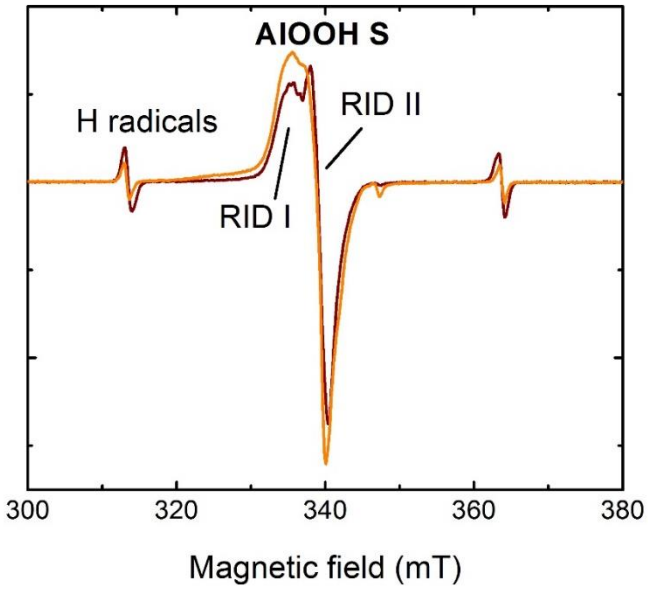

Figure 5.6. EPR spectra of electron irradiated AlOOH L (wine line) and AlOOH S (orange line) at 77 K at 46 kGy.

Table 5.3. Radiolytic yields of radiation induced defects in electron irradiated samples at 77 K.

	RID yield at 77 K		
	G (O^-) mol/J x 10^{-8}	**G (O_3^-) mol/J x 10^{-8}**	**H µmol/kg**
AlOOH L	70 ± 10	17 ± 4	1000 ± 100
AlOOH S	80 ± 20	18 ± 5	68-220

The annealing at room temperature of irradiated samples at 77 K reveals an important decrease of the RID signals by a factor comprised between 5 and 10. A major difference is observed between the materials concerning H radicals: in AlOOH L their concentration remains unchanged while in AlOOH S almost no H radicals can be detected at RT.

To conclude, low temperature irradiation confirms that the primary creation of defects does not depend on the particle size. Differences between the materials with different crystallite sizes are only observed at room temperature where remaining centers represent only 10 or 20% of the initial transient defects particles. We conclude that the particle size or the specific surface influence only secondary reactions once the migration of the defects is efficient.

5.2.1.2 Dose effect in Boehmite at RT

Qualitatively EPR spectra of hydrated and dry materials at room temperature are similar. Some EPR spectra are presented in Appendix 8. The evolutions with the dose of different defects from irradiated samples hydrated at 76% RH and dry samples are shown in Figure 5.7, Figure 5.8, Figure 5.9 and Figure 5.10. In order to compare, results obtained from dry materials are also plotted.

In the case of AlOOH L, there is no big difference between hydrated and dry samples except a slight decrease of H radical concentration in presence of sorbed water. The remarkable difference is the quasi absence of F_S centers in hydrated materials (RID III). These electron centers are located on the surface and can react with sorbed water molecules. Therefore one may wonder if these centers are an evidence of the energy transfer between the solid and the surface. In Chapter 4, the minimal yield of formation of F_S centers was estimated to be close to 2×10^{-8} mol/J. Although this value is lower than $G(H_2)$ measured for hydrated AlOOH L, the order of magnitude may allow us to think that a fraction of the electron transfer to the surface formed transient F_S centers that react with water molecules present at the surface.

To confirm this hypothesis experiments at lower dose on dry samples are needed. Likewise, the potential effect of drying treatment on trapping properties of electron centers has to be analyzed.

Concerning AlOOH S it should be emphasized that in hydrated materials a significant concentration of H radicals and RID III' is observed even at 300 kGy while these paramagnetic centers were only detectable at the lowest doses in dry samples.

It is tempting to assign these differences to the important fraction of water present in AlOOH S (14- 18 % by weight). Electron and H radicals can come from the radiolysis of water. Experiments using D_2O are proposed to clarify this point.

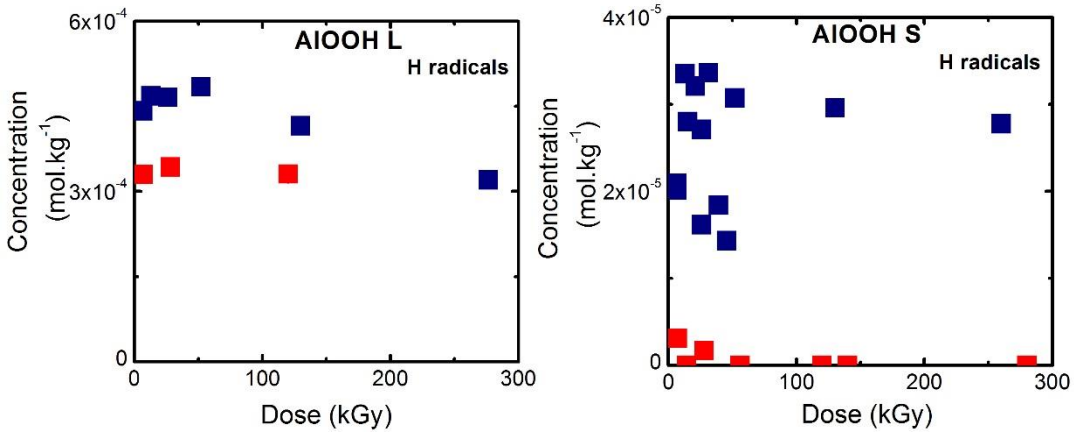

Figure 5.7. Evolution of the concentration of H radicals in hydrated at 76 % RH (blue dots) and dry (red dots) AlOOH L (left) and AlOOH S (right) as a function of the dose.

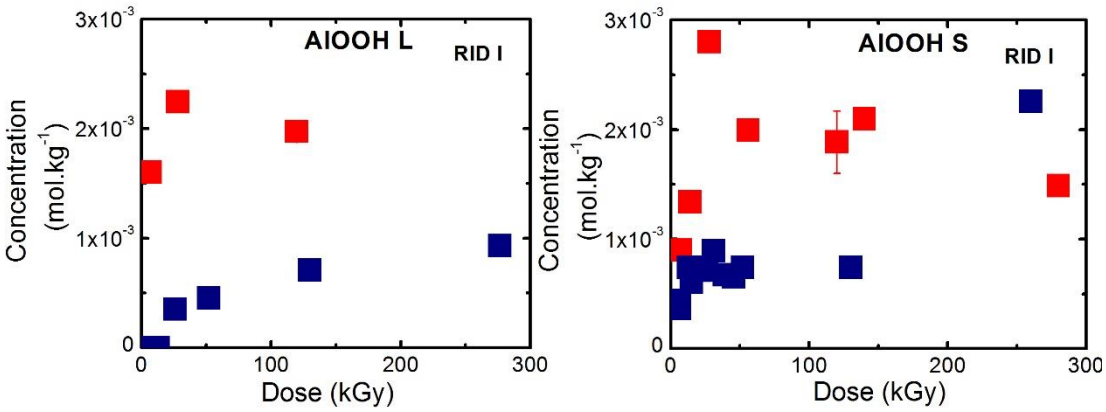

Figure 5.8. Evolution of the concentration of RID I in hydrated at 76 % RH (blue dots) and dry (red dots) AlOOH L (left) and AlOOH S (right) as a function of the dose.

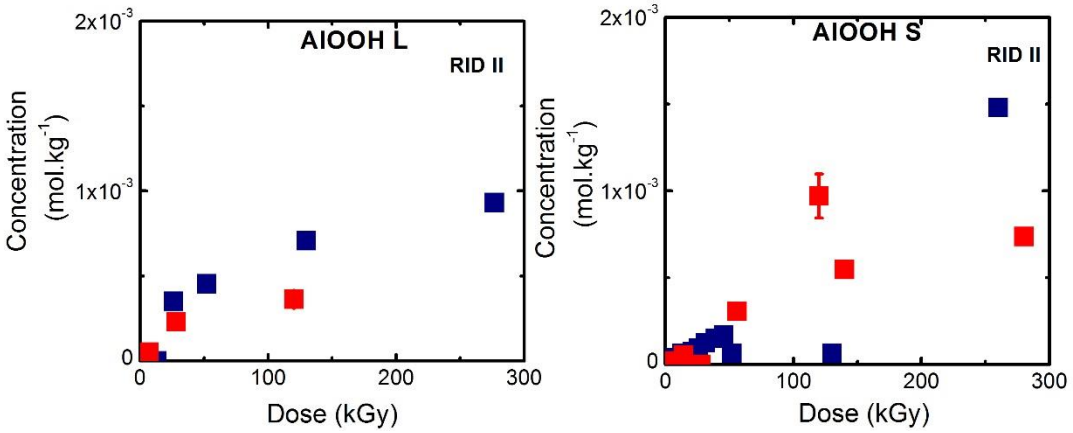

Figure 5.9. Evolution of the concentration of RID II in hydrated at 76 % RH (blue dots) and dry (red dots) AlOOH L (left) and AlOOH S (right) as a function of the dose.

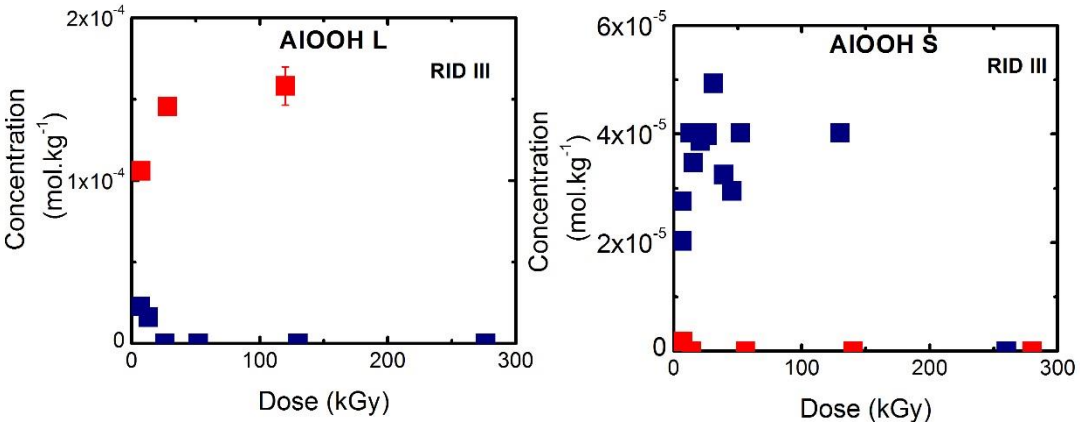

Figure 5.10. Evolution of the concentration of RID III in hydrated at 76 % RH (blue dots) and dry (red dots) AlOOH L (left) and AlOOH S (right) with respect to dose.

5.2.1.3 Room temperature stability

Figure 5.11and Figure 5.12 present the evolution of the EPR spectra with respect to time at RT.

Concerning AlOOH L, H radicals shows a decrease of 38% after 24 hours, RID I lost 63% of its initial intensity and RID II 36% after 24 hours. These defects are less stable in hydrated samples compared to dry materials.

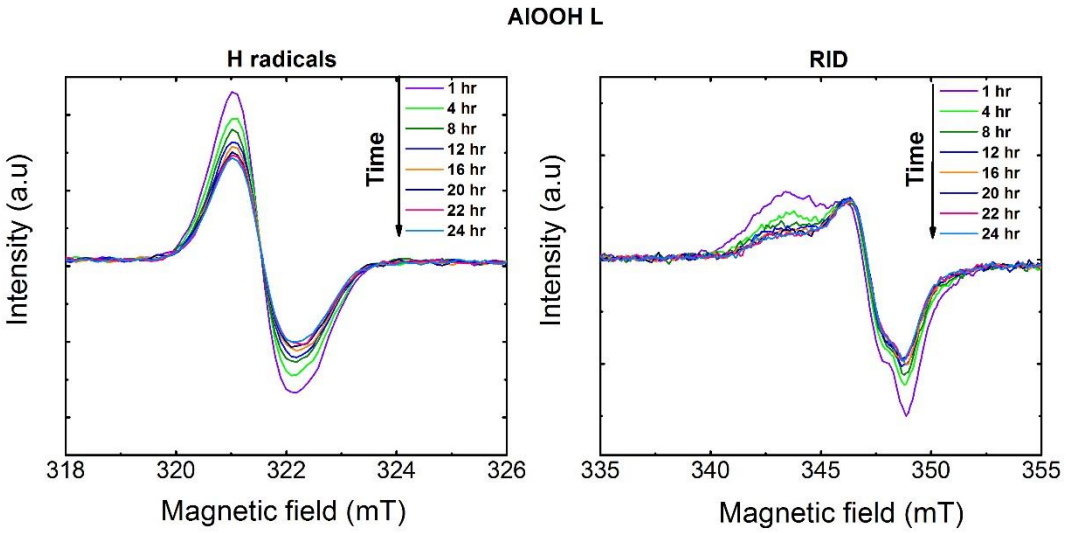

Figure 5.11. Evolution at RT of EPR spectra of radiation induced defects in electron irradiated AlOOH L at 30 kGy. The evolution of H radicals (on the left) and RID (on the left) is shown as a function of time from one hour until 24 hours.

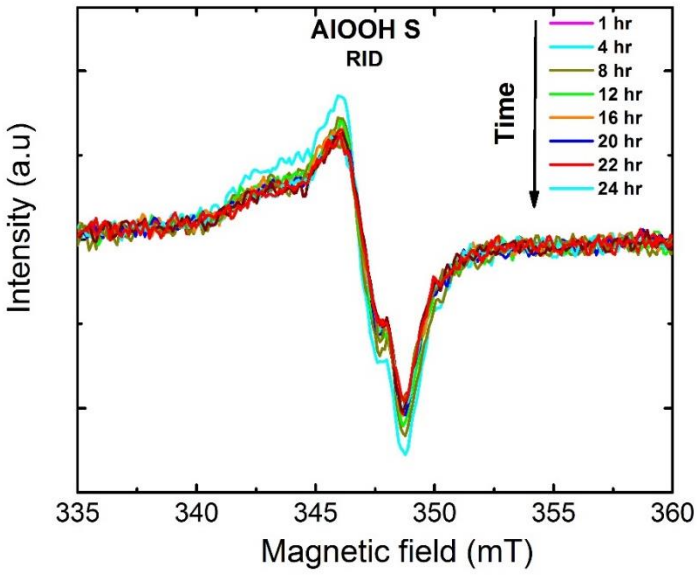

Figure 5.12. Evolution at RT of EPR spectra of radiation induced defects in electron irradiated AlOOH S at 30 kGy. The evolution of RID is shown as a function of time from one hour until 24 hours.

5.2.1.4 Annealing above room temperature

Annealing of EPR defects originating from electron irradiation of AlOOH S and L at 30 kGy, is shown in Figure 5.13 and Figure 5.14.

In AlOOH L, H radicals lost 61% of the initial intensity at 74°C and disappears at 110°C. At 74°C, RID I has 30% of its initial intensity and RID II has 77%. RID I disappears at 140°C while RID II is at 45% at 185°C.
At 74°C, for AlOOH S the RID I attends 31% approximately and disappears at 185°C. RID II is at 60 % of the initial intensity at 74°C and at 33% at 185°C.

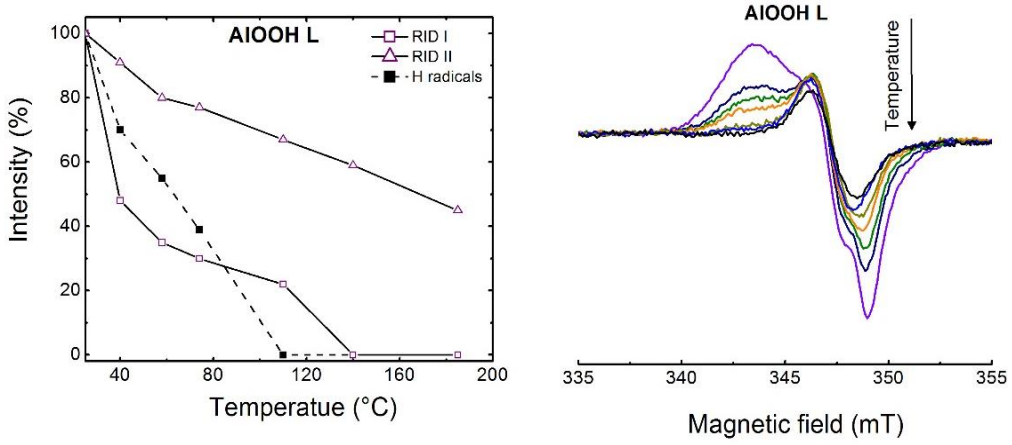

Figure 5.13. Evolution of H radicals and radiation induced defects as a function of temperature in electron irradiated AlOOH L at 30 kGy.

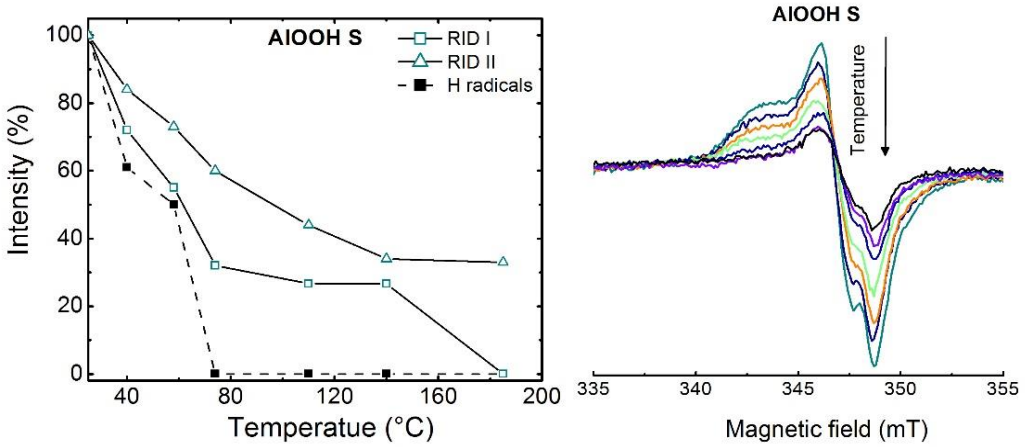

Figure 5.14. Evolution of H radicals and radiation induced defects as a function of temperature in electron irradiated AlOOH S at 30 kGy.

In order to study the effect of structure, the same analyses were conducted on $Al(OH)_3$ and are presented in the next section.

5.2.2 Bayerite $Al(OH)_3$

5.2.2.1 Trapped defects in Bayerite at 77 K

Figure 5.15 presents the EPR spectrum of hydrated $Al(OH)_3$ electron-irradiated at 77 K at 46 kGy. It is very close to that observed for AlOOH. In particular it reveals the presence of a singlet which has spin parameters close to those of RID II'. This signal was not observed in dry $Al(OH)_3$ at room temperature. Annealing at room temperature causes the disappearance of both H radicals and RID II', the intensity of RID I' increases and the signal assigned to RID VI' emerges.

The loss of RID II' attributed to ozonide radicals can be due to the formation of O_3:

By a reaction with O^- for example:

$$O_3^- + Al\cdots O^- \rightarrow O_3 + Al\cdots O^{2-}\cdots Al \quad \textbf{(61)}$$

The formation of oxide in interaction with two aluminums is highly probable and is evidenced by the formation of RID VI'.

Another mechanism is the reverse reaction of ozonide radicals:

$$O_3^- \rightarrow O_2 + O^- \quad \textbf{(62)}$$

The increase of the concentration of O^- centers after annealing at RT supports this mechanism.

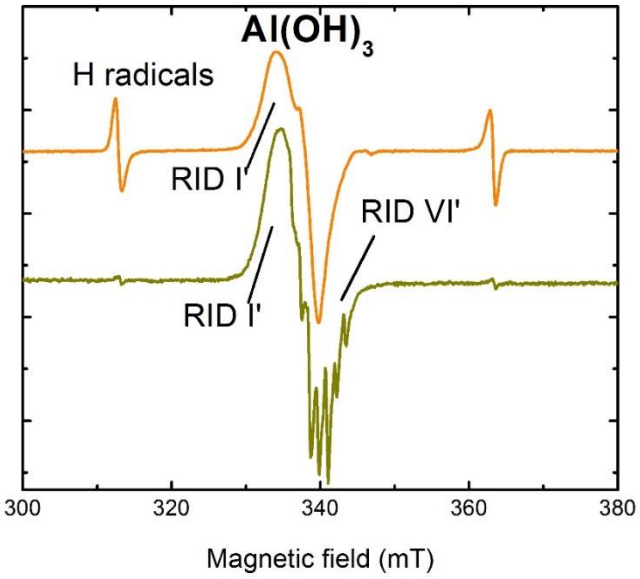

Figure 5.15. EPR spectra of electron irradiated $Al(OH)_3$ at 77 K, at 46 kGy (orange) and annealed at RT (olive) (76 % RH).

Table 5.4. Radiolytic yields of radiation induced defects in $Al(OH)_3$ irradiated using electron beams at 77 K.

RID yield at 77 K		Concentration
G (O^-) mol/J x 10^{-8}	G (O_3^-) mol/J x 10^{-8}	H µmol/kg
43 ± 6	54 ± 9	725

5.2.2.2 Dose effect at room temperature

Figure 5.16 shows the evolution of the concentration of radiation induced defect RID I' and H radicals with respect to the dose received in $Al(OH)_3$. EPR spectra are presented in Appendix 8. The comparison with the results obtained for dry $Al(OH)_3$ shows that unlike AlOOH L and S, the behavior of defects with respect to the dose is cery close in hydrated and dry $Al(OH)_3$.

RID III' was formed at 7, 15 and 30 kGy Appendix 8.

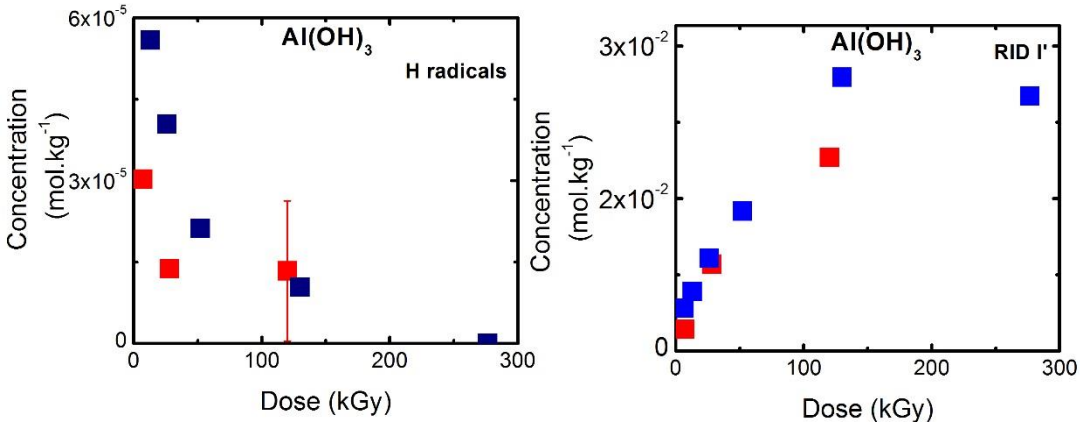

Figure 5.16. Evolution of the concentration of H radicals in hydrated at 76 % RH (blue dots) and dry (red dots) $Al(OH)_3$ as a function of the dose

5.2.2.3 Room temperature stability

$Al(OH)_3$ stabilization at room temperature is shown in Figure 5.17, after 24 hours the initial H radical concentration decreased by 85%, as mentioned before H radicals were not stable in hydrated $Al(OH)_3$. RID III' increased by 35%. The stability of H radicals and RID III' were comparable between dry and hydrated $Al(OH)_3$.

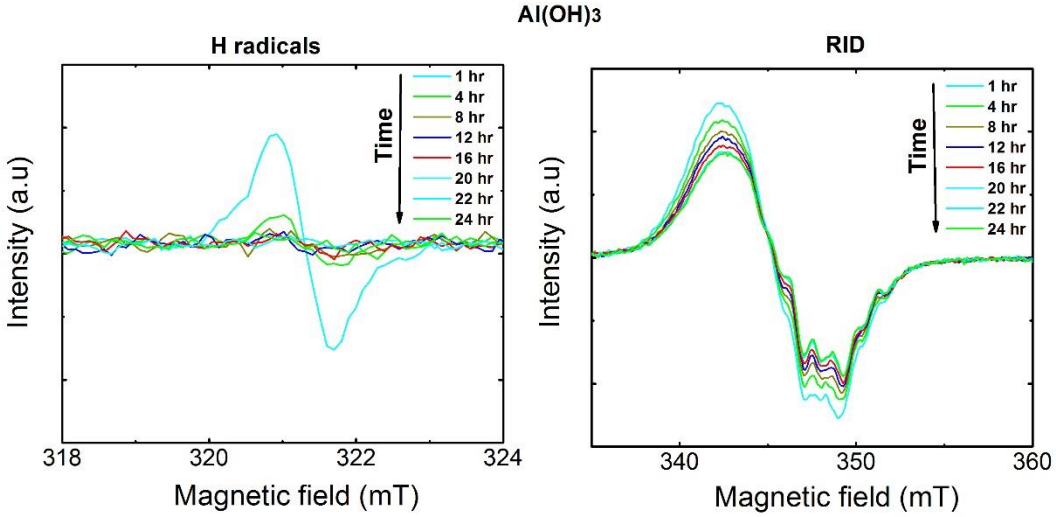

Figure 5.17. Evolution at RT of EPR spectra of radiation induced defects in electron irradiated $Al(OH)_3$ at 30 kGy. The evolution of H radicals (on the left) and RID (on the left) is shown as a function of time from one hour until 24 hours.

5.2.2.4 Annealing above room temperature

Annealing of EPR defects originating from the irradiation of $Al(OH)_3$ using electron beams at 30 kGy is shown and discussed in this section. In Figure 5.18, thermal evolution of the relative intensity of H radical and RID I' spectra is also plotted. H radicals lost 70% of the initial intensity at 40°C, and disappears above 58°C. The stability of H radicals regarding temperature was higher in dry $Al(OH)_3$, at 40°C H radical intensity was almost the double in dry samples. As for dry $Al(OH)_3$ above 80°C RID I' is replaced by a new defect RID V'.

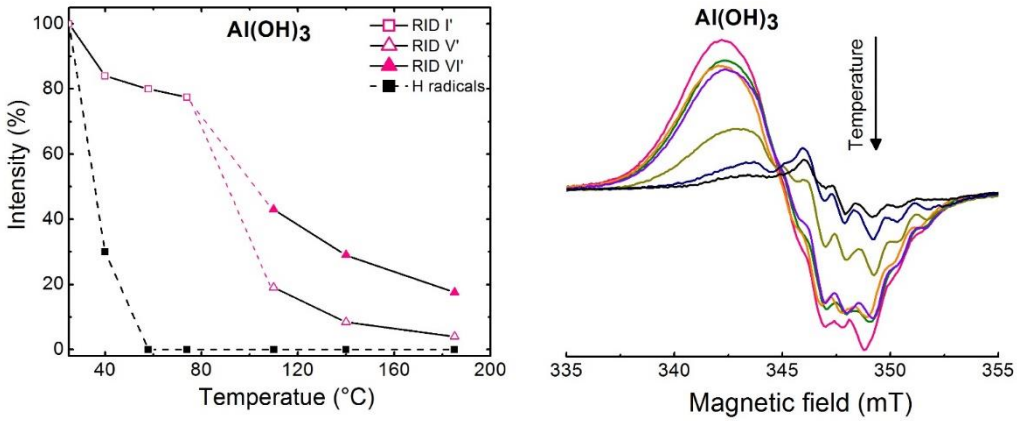

Figure 5.18. $Al(OH)_3$ annealing showing radiation induced defect shapes a temperature and the disappearance in intensity. Black dotted line represents H radicals while the two pink dotted lines are used to show the disappearance of the square (RID I') and the appearance of two new defects symbolized with a close and an open triangle and which are related to RID V' and RID VI' respectively.

5.3 Discussion

The main results concerning hydrated materials are given in Table 5.5, Table 5.6 and Table 5.7.

Table 5.5. Defect radiolytic yields from irradiated samples at 77 K, RT using electron beams.

	Radiolytic yield (mol/J) x 10^{-8}					
	AlOOH L		**AlOOH S**		**$Al(OH)_3$**	
	RT	*77K*	*RT*	*77K*	*RT*	*77K*
RID I	16	70 ± 10	4 ± 1	80 ± 20	65 ± 10	54 ± 9
RID II	0.3-1.9	17 ± 4	0.3	18 ± 5		

Table 5.6. Concentrations of H radicals from irradiated samples at 77 K, RT using electron beams.

	(µmol/kg)	
	H	
	RT	*77K*
AlOOH L	450	1000
AlOOH S	28 ± 5	144
$Al(OH)_3$	60 ± 5	725

While discussing H_2 production in hydrated AlOOH and $Al(OH)_3$, we must keep in mind its analogies and differences with the behavior of dry materials:

- The H_2 production is 15-20 times higher in hydrated materials,
- Hydrated materials do not present H_2 detrapping upon heating,
- Same defects and almost same quantities are produced in dry and hydrated materials.

The very important hydration effect on H_2 production can be explained by different mechanisms:

- Energy/electron transfer to the water layer,
- Activation of H diffusion that prevent its back reaction,

In AlOOH L and in a lesser extent in AlOOH S the global $G(H_2)$ (the yield calculated with respect to the total energy received by the system) exceeds the primary yield of liquid water. This result demonstrates that, if there is an energy transfer, it is ultra efficient between the solid and sorbed water.

In order to highlight the energy transfer, radiolytic yields were calculated with respect to energy received only by the adsorbed water (see section 2.1.2). This energy is supposed to be almost proportional to the weight fraction of water. The results are presented in Table 5.7.

The higher $G(H_2)$ is 134 x 10^{-7} mol/J or 129 molecules/100 eV. This value means that each one molecule H_2 needs 0.78 eV to be formed which is energetically impossible because this energy is too small to break bonds and rearrange atoms. The energy deposited directly in adsorbed water by the electron or gamma rays is not sufficient to produce the measured hydrogen quantities. The presence of the solid enhances the efficiency of water radiolysis. This process is well documented for oxides in suspensions. [126]

An energy transfer process can also explain why very low amounts of water is necessary to activate H_2 production. In fact, a strong increase in H_2 production upon minute solid hydration has already been observed in other systems such as in SBA 15. [127] The interpretation was therefore, H_2O molecules and not surface hydroxyls, are efficient energy acceptors.

Table 5.7. Radiolytic yield of H_2 calculated with respect to the energy received by adsorbed water.

		11% RH	**44% RH**	**76% RH**
AlOOH L	**$G(H_2)$ mol/J x10^{-8}**	1230-1450	580-680	650-750
AlOOH S		54-64	32-38	24-28
$Al(OH)_3$		27-36	23-31	46-60

Unlike energy transfer processes in radiation chemistry of adsorbed water, the activation of diffusive processes by water is not well documented.

Concerning O^- centers, there is no remarkable difference between dry and hydrated materials. So we suppose that these centers are produced at the same place in the structure, therefore it is their reductive counterpart that migrates preferentially to the hydrated surface.

In the following, the four possibilities (exciton, electron, H radicals and molecular hydrogen) are discussed separately.

Exciton

By analogy with what was observed for silica glasses where the activation of energy transfer by surface hydration leads to a strong decrease of defect production,[7] a decrease of the O^- centers is expected in our systems. A significant reduction is detected for AlOOH but the opposite effect is observed for $Al(OH)_3$.

Electron

The transfer of electron and their trapping at the surface has been evidenced in dry AlOOH L by the formation of F_S center. Unfortunately these centers are not detected in the others materials.

H radical

Our experiments do not provide quantitative information about the diffusion of H radicals. It was only observed that trapped H radicals are more stable in hydrated AlOOH L. This result is in contradiction with the proposal of an increase of the migration in presence of water but it should not be over interpreted as we do not know if trapped and mobile H radicals have the same properties.

H_2

The absence of detrapped hydrogen in hydrated materials could be attributed to an enhancement of H_2 diffusion in the solid. This proposition is questionable because, as discussed in Chapter 4, the quantity of hydrogen released after annealing results from two competitive processes – the reaction of trapped hydrogen with O^- centers and the recombination of O^- centers. Detrapped hydrogen represents only 5 or 10%. Finally we could consider that the variation of the O^- centers concentration or of the recombination rate can inhibit the release of hydrogen.

The phenomena occurring in hydrated samples are concluded to be similar to that in dry samples but with energy transfer effect. This last point has to be developed by conducting time resolved experiments.

6. Chapter 6: Molecular hydrogen production from Brucites

This section presented preliminary results related to the effect of impurities and particle size on hydrogen production from another hydroxide chosen as a model compound which is $Mg(OH)_2$ (Brucite). This is only a perspective test and experiments were not taken further as far as with AlOOH and $Al(OH)_3$. This was intended in order to see if we can generalize the effect of impurities and nanometric particle size on hydrogen production in other hydroxides.

$Mg(OH)_2$ was elaborated in the laboratory following the method of Sutto et al.[76] Some parameters were adjusted regarding the article and were described in section 2.2.

A brief characterization was achieved and is described in section 6.1. In a first step the effect of particle size on hydrogen production is briefly described and in a second one the effect of impurity is presented. Materials were irradiated in the same way described for dry AlOOH and $Al(OH)_3$ using electron beams (section 2.3.1.1).

6.1 Characterization

Synthesized $Mg(OH)_2$ with varied impurities types and amounts (KNO_3 and K_2SO_4), were analyzed with XRD in order to determine phase composition as well as crystallite sizes (see Figure 6.1). They are compared to a commercial industrial $Mg(OH)_2$ (containing 2 % of various impurities) and has 19 nm as a particle size (blue line Figure 6.1).

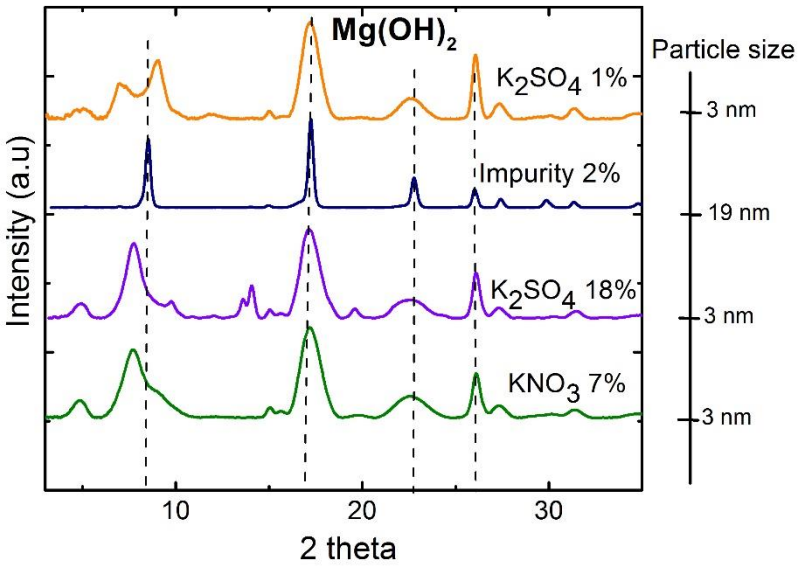

Figure 6.1. X-ray spectra of two sized $Mg(OH)_2$.

In Figure 6.1 1shows a 19 nm particle sized sample (blue line with various impurities). Smaller particle sizes are represented (3 nm) with 1% and 18% K_2SO_4 (orange and violet respectively) and a fourth sample is used having a 3 nm particle size and containing 7% KNO_3 (green line).

Synthetized samples contained more phases than the commercial one (blue line Figure 6.1). Particle size was calculated using Debye Scherer as explained in section 2.4.1

In this section, the effect of impurity and particle size are the only parameters studied, therefore dry samples were used and were prepared after evacuation at 170°C for 5 hours under secondary vacuum. Figure 6.2. shows the thermogram of commercial $Mg(OH)_2$, phase transformation occurs at 400˚C and heat treatment applied at 170˚C before irradiating samples assures that structural water is not altered.

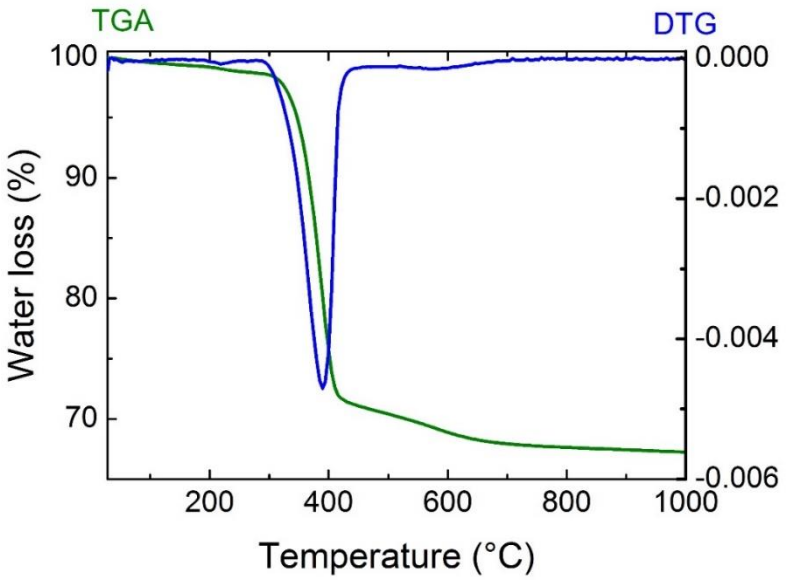

Figure 6.2.TGA and DTG characterization of pristine $Mg(OH)_2$ under N_2.

Parameters were as follows:

- Particle size: 2 sizes, 3 nm (synthetized) and 19 nm (purchased used as a reference, blue line)
- Impurity: 2% pure (commercial, blue line), synthetized one with 1% K_2SO_4, 18% K_2SO_4 and 7% KNO_3 (orange violet and green lines respectively, Figure 6.1).

After a brief characterization of the samples, the next sections describe the hydrogen production at room temperature from irradiated samples.

6.2 H_2 production from different particle sized samples

In this section we chose to compare the purest materials with different particle sizes. Figure 6.3 shows the production of H_2 from 3 and 19 nm $Mg(OH)_2$.

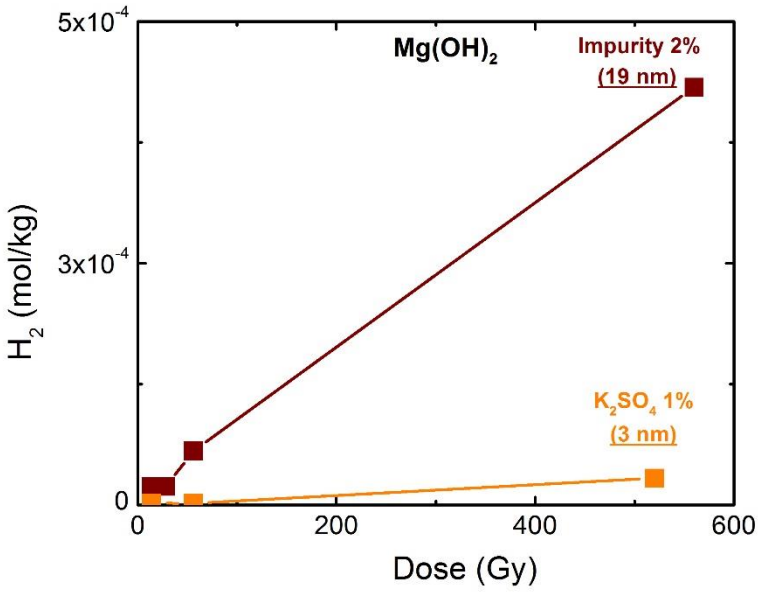

Figure 6.3. H_2 production from 19 nm and 3 nm irradiated $Mg(OH)_2$ (purity is 98% and 99% respectively).

$Mg(OH)_2$ having 19 nm as particle size released more hydrogen than the 3 nm ones, radiolytic yields are resumed in Table 6.1. Values are smaller than the published one and this could be due to the difference in particle size or drying processes before irradiation. [70]

This behavior was also seen in irradiated samples described in the previous sections: AlOOH L (large-particle size) released more hydrogen than AlOOH S (small-particle size). $Mg(OH)_2$ small-particle size released less hydrogen and this could be due to H radicals or H_2 precursors formed in separated crystallites which forbid their encounter and their recombination to form molecular hydrogen. Though radiolytic yields obtained from $Mg(OH)_2$ were smaller than that obtained from AlOOH and $Al(OH)_3$.

The next section describes the effect of impurity on molecular hydrogen production.

6.3 H_2 production from different impurity rates

The effect of impurity on small particle size is studied in this section. Three synthetized $Mg(OH)_2$ with the same particle size are used here (3nm). The parameter varying is considered to be impurity. KNO_3 (7%) and K_2SO_4 (1% and 18%) are present in the chosen samples represented by green, orange and purple lines respectively in Figure 6.4. Figure 6.4 shows the production of H_2 from different impurity levels in $Mg(OH)_2$.

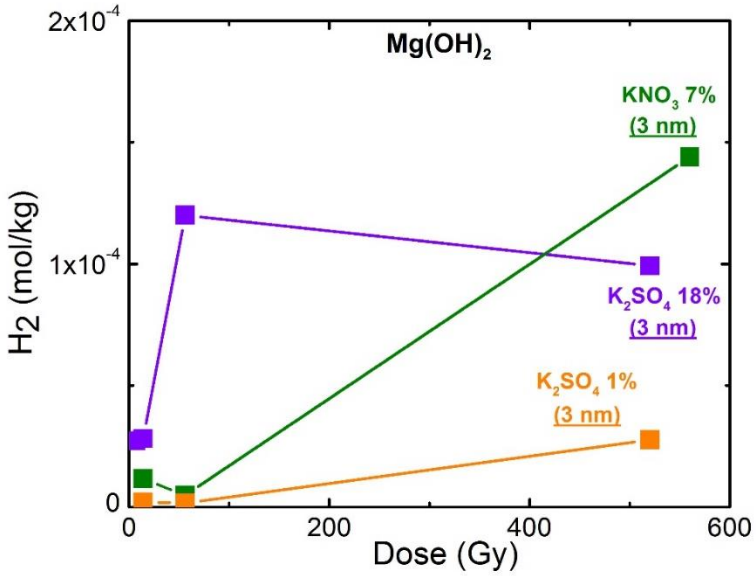

Figure 6.4. H_2 production from 3 nm irradiated $Mg(OH)_2$ with different impurity levels.

At low doses $Mg(OH)_2$ containing 18% K_2SO_4 released more hydrogen than that containing 1% K_2SO_4 and 7% KNO_3 released more hydrogen than that containing 18% K_2SO_4.. At higher doses, $Mg(OH)_2$ containing 18% K_2SO_4 saturates (the test at 520 kGy was repeated two times and results indicate a saturation).

Two factors may be affecting the production of H_2:

- The amount of impurities, $Mg(OH)_2$ containing more impurities released less hydrogen, more impurities may be associated to defects which lead the H radicals to react together and form H_2 instead of reacting with impurities or anionic defects.
- The type of impurities, NO_3^- and SO_4^{2-} may have different behavior concerning trapping H radicals or other H_2 precursor species. These species play an important role in the radiolytic decomposition: SO_4^{2-} is a hole trap and NO_3^- an electron trap, hydrogen produced from the sample containing nitrates were supposed to produce less hydrogen but results obtained have to be more developed. [46, 128]

Table 6.1. Radiolytic yield of irradiated samples as a function of impurity and particle size.

Irradiation source	Impurity	Particle size (nm)	Radiolytic yield (mol/J) x 10^{-8}	
e-	2 % impurity (commercial)	19	0.07-0.13	Our results
	1% K_2SO_4	3	0.003-0.014	
	18% K_2SO_4	3	0.019-0.4	
	7% KNO_3	3	0.0087-0.082	
60Co	-	-	0.53	[70]
He 5 MeV	-	-	0.38	

6.4 Summary

Considering these preliminary results, we can conclude as follows:

- Impurity tends to favor secondary reactions. As a consequence, a decrease in hydrogen production is likely to occur. The extent of this reduction depends certainly on the type and amount of impurities.
- Particle size influences hydrogen production and for nanometric particles we can see that small particles release less hydrogen, this result could be generalized for other hydroxides having nanometric sizes but more investigations has to be conducted on other nanomeric samples and on larger particle sizes.
- This test shows that by synthetizing hydroxides one can impose important parameters affecting hydrogen production such as particle size, impurity type and amount. A mix of impurities would be interesting in order to mimic phases encountered in the metal casks

« Regardez les oiseaux du ciel : ils ne sèment ni ne moissonnent, et ils n'amassent rien dans des greniers; et votre père céleste les nourrit. Ne valez-vous pas beaucoup plus qu'eux? » Matthieu 6:26

7. Conclusion

This study elucidated the behavior of two hydrates acting as model compounds in the nuclear industry. The behaviors of AlOOH and $Al(OH)_3$ were studied under different irradiation sources.

Many preexistent studies treated the radiolysis of liquid water in most cases or the physical water adsorbed on a solid surface. This thesis not only studies the radiolysis of adsorbed water on aluminum hydroxide and oxyhydroxide but also that of structural water in carefully very dry samples.

Molecular hydrogen was quantified considering many factors such as particle size, structure, water forms, temperature and impurities. These hydrates are so sensible to radiolysis.

In order to understand the mechanisms of molecular hydrogen production from the concerned irradiated samples we conducted electron paramagnetic resonance at 77K, room temperature and above.

The main results are resumed as follows:

Sample structure and surface

Surface and structural characterizations were conducted on samples before and after heat treatment and irradiation. To serve the purpose, XRD, IR, RAMAN, SEM, BET, TGA, EPR, ICP and XPS were used.

AlOOH and $Al(OH)_3$ studied showed different characteristics. Two particle sizes were used: 5 nm for AlOOH and (18-20) nm for AlOOH and $Al(OH)_3$.

These samples have different behaviors with respect to water adsorption and have different degrees of internal ordering. The small particle size (AlOOH S) is more disordered than AlOOH L.

Hydrogen production

Molecular hydrogen production was quantified in irradiated dry and hydrated samples. For dry samples, AlOOH L showed the highest radiolytic yields $(5.1 \pm 2.4) \times 10^{-9}$ mol/J while AlOOH S the lowest ones $(0\text{-}0.42 \pm 0.02) \times 10^{-9}$ mol/J. $Al(OH)_3$ values ranged between the first ones described and was $(2.1 \pm 0.5) \times 10^{-9}$ mol/J.

The effect of particle size was obvious in dry samples, where the formation of H_2 was more efficient in large-particle size. This effect was suppressed under high LET irradiation. An additional H_2 production was observed at higher temperature. This occluded H_2 production is 10 times greater than at RT $(4.6 \pm 1.1) \times 10^{-9}$ mol/J) in

AlOOH S. In AlOOH L, the highest H_2 occluded (12 ± 9.1) x 10^{-9} mol/J. As for $Al(OH)_3$ occluded yields were (7.6 ± 1.3) x 10^{-9} mol/J).

These yields can be compared to that from irradiated hydroxides in the literature but one has to put in mind that quantified hydrogen published is only a small quantity of the real one formed. As seen here a huge quantity is still trapped in the material and is subject to sensible variations.

As for hydrated samples the production of H_2 was very high, they released minimum 10 times more hydrogen than dry ones and, for example in AlOOH L, this release was triggered by very low amounts of water. This indicates the efficiency of radiolysis and that energy transfer occurs between solid and water on the surface.

To sum up three H_2 sources may exist:

- H_2 released at room temperature resulting from irradiated dry samples where H radicals migrate and recombine on the surface.
- H_2 released at room temperature resulting from irradiated hydrated samples due to energy transfer between the solid and its surface.
- H_2 is mainly produced by the homolytic reaction of OH that is trapped in the material.

Radiation induced defects

The stability of radiation induced defects was studied and they were quantified using electron paramagnetic resonance. Trapped electron and H radicals, which did not accumulate, and different anionic oxygen radicals were formed in irradiated samples defect and their spin characterizations are resumed in Table 7.1. In all AlOOH, same behavior was observed with respect to temperature. Three main oxygen centered defects were identified O^-, O_2^- and O_3^-.

O^- was produced in greater number and supposed to be formed as follows:

$$2OH^- = 2O^- + H_2 \quad \textbf{(63)}$$

The reducing equivalent would be H_2 in this case.

Practical point of view

Particle size, structure, impurities don't influence the primary processes in concerned irradiated materials but influence well the processes related to the migration of the radiation-induced species. This is why these parameters play a major role in the production of H_2 at room temperature.

The disorder and presence of impurities tend to reduce H_2 production which is reassuring from a practical point of view where perfect materials are rarely encountered.

Further work

The study of the effect of impurity on H_2 production were initiated in Mg $(OH)_2$. Same experiments done on AlOOH and $Al(OH)_3$ would be interesting to be conducted on brucite in order to generalize the hydrogen production in hydroxides with respect to structure, particle size and impurity. Varying more impurity types as well as crystallite sizes going to micrometric sizes is of prime importance to confirm and generalize our hypotheses. Annealing of samples to see if there is any trapped gas (especially H_2) would be the most important to conduct in these materials.

The study of structure and the placement of H atoms was started using neutron diffraction, data has to be treated in order to detect the maximum differences between samples. Polarized neutron diffraction would eventually allow to localize defect sites. However, the major challenge remains in the occluded H_2 localization, an isotopic labelling would be essential in this case.

Other Interesting experiments would be the following of reactions induced in irradiated samples in the real time in order to detect the unstable species that might be formed and recombine into H_2 that was seen as trapped.

Owing to the high intensity of the EPR signals, time resolved EPR may be envisioned as well as studying defects by annealing at low temperature.

The exposition of irradiated samples to air and different gas would be started in further works. A pulse radiolysis of suspensions is water in one of the future objectives.

The effect of heavy ions on the creation of defects are essential in order to understand the obtained radiolytic yields quantified during this thesis.

Table 7.1. Summary of RID with their spin characterizations and attribution.

Name	Material	Spin parameters	Center
RID I	AlOOH	$g_x = g_y = 2.024$; $g_z = 2.0034$ $\Delta H_{pp}^x = \Delta H_{pp}^y = 4.8\ mT$; $\Delta H_{pp}^z = 3.09\ mT$	O^-
RID I'	$Al(OH)_3$	$g_x = g_y = 2.030$; $g_z = 2.0026$ $\Delta H_{pp}^x = \Delta H_{pp}^y = 4.72\ mT$; $\Delta H_{pp}^z = 3.88\ mT$	O^-
RID II	AlOOH	$g_z = 2.010$; $\Delta H_{pp}^z = 1.7\ mT$	O_3^-
RID II'	$Al(OH)_3$	$g_z = 2.009$; $\Delta H_{pp}^z = 2.07\ mT$	O_3^-
RID III	AlOOH	$g_z = 1.998$; $\Delta H_{pp}^z = 0.2\ mT$	F_S
RID III'	$Al(OH)_3$	$g_z = 1.998$; $\Delta H_{pp}^z = 0.2\ mT$	F_S
RID IV	AlOOH	$g_x = g_y = 2.0043$; $g_z = 2.064$ $\Delta H_{pp}^x = \Delta H_{pp}^y = 2.06\ mT$; $\Delta H_{pp}^z = 4.63\ mT$	O_2^-
RID V'	$Al(OH)_3$	$g_x = g_y = 2.0037$; $g_z = 2.036$ $\Delta H_{pp}^x = \Delta H_{pp}^y = 1.84\ mT$; $\Delta H_{pp}^z = 1.66\ mT$	O_2^-
RID VI'	$Al(OH)_3$		$Al \cdots O^- \cdots Al$

Reference

1. Bonin, B.; Colin, M.; Dutfoy, A., Pressure Building During the Early Stages of Gas Production in a Radioactive Waste Repository. *Journal of Nuclear Materials* **2000**, *281*, 1-14.
2. Lewis, B.; von Elbe, G., Combustion, Flames and Explosion of Gases,(Esp. Chapter V, 15, Combustion Waves in Closed Vessels, Pp. 381-395). *Academic Press, Inc., Orlando, Florida (Revised edition of text published in 1951) the end of the detonation cell. Gasdynamics of detonations and explosions. Prog. Astronaut. Aeronaut AIAA, Washington, DC* **1987**, *75*, 358-369.
3. Drell, I. L.; Belles, F. E., Survey of Hydrogen Combustion Properties. **1958**.
4. Hu, T. A., Improved Model for Hydrogen Generation Rate of Radioactive Waste at the Hanford Site. *Nuclear Technology* **2012**, *178*, 39-54.
5. Andes, T. *Characterization of Corrosion Damage on Aluminum Fuel Assemblies in Basin Storage*; Savannah River Site (US): 2002.
6. Westbrook, M. L.; Sindelar, R. L.; Fisher, D. L., Radiolytic Hydrogen Generation from Aluminum Oxyhydroxide Solids: Theory and Experiment. *Journal of Radioanalytical and Nuclear Chemistry* **2015**, *303*, 81-86.
7. Le Caër, S.; Rotureau, P.; Brunet, F.; Charpentier, T.; Blain, G.; Renault, J. P.; Mialocq, J.-C., Radiolysis of Confined Water: Hydrogen Production at a High Dose Rate. *ChemPhysChem* **2005**, *6*, 2585-2596.
8. Rotureau, P.; Renault, J.; Lebeau, B.; Patarin, J.; Mialocq, J. C., Radiolysis of Confined Water: Molecular Hydrogen Formation. *ChemPhysChem* **2005**, *6*, 1316-1323.
9. Jonah, C. D.; Rao, B. M., *Radiation Chemistry: Present Status and Future Trends*; Elsevier, 2001; Vol. 87.
10. Ziegler, J. F.; Ziegler, M. D.; Biersack, J. P., Srim – the Stopping and Range of Ions in Matter (2010). *Nuclear Instruments and Methods in Physics Research Section B: Beam Interactions with Materials and Atoms* **2010**, *268*, 1818-1823.
11. Ziegler, J.; Biersack, J., The Stopping and Range of Ions in Matter. In *Treatise on Heavy-Ion Science*, Bromley, D. A., Ed. Springer US: 1985; pp 93-129.
12. LaVerne, J. A., Track Effects of Heavy Ions in Liquid Water. *Radiation research* **2000**, *153*, 487-496.
13. Woods, R. J.; Pikaev, A. K., *Applied Radiation Chemistry: Radiation Processing*; John Wiley & Sons, 1994.
14. Han, B.; Kim, J.; Kim, Y.; Jeong, K.-Y., Industrial Application of E-Beam Accelerators in Korea. *Journal of the Korean Physical Society* **2012**, *61*, 180-184.
15. Rotureau, P. Etude De La Radiolyse De L'eau En Milieu Poreux. Université d'Evry-Val d'Essonne, 2004.
16. Leroy, C.; Rancoita, P.-G., *Principles of Radiation Interaction in Matter and Detection*; World Scientific, 2009; Vol. 2.
17. Hatano, Y.; Katsumura, Y.; Mozumder, A., *Charged Particle and Photon Interactions with Matter: Recent Advances, Applications, and Interfaces*; CRC Press, **2010**.
18. Kotomin, E.; Popov, A., Radiation-Induced Point Defects in Simple Oxides. *Nuclear Instruments and Methods in Physics Research Section B: Beam Interactions with Materials and Atoms* **1998**, *141*, 1-15.

19. Nakamoto, K., *Infrared and Raman Spectra of Inorganic and Coordination Compounds*; Wiley Online Library, **1986**.
20. Lund, A.; Shiotani, M., *Epr of Free Radicals in Solids I: Trends in Methods and Applications*; Springer Science & Business Media, **2012**; Vol. 24.
21. Burton, M., Symposium on Radiation Chemistry Introduction. *The Journal of Physical Chemistry* **1952**, *56*, 545-545.
22. Hayes, W.; Stoneham, A. M., *Defects and Defect Processes in Nonmetallic Solids*; Courier Corporation, **2004**.
23. El Omar, A. K. Études Des Réactions Primaires En Solutions Par La Radiolyse Pulsée Picoseconde. 2013.
24. Caffrey Jr, J. M.; Allen, A. O., Radiolysis of Pentane Adsorbed on Mineral Solids. *The Journal of Physical Chemistry* **1958**, *62*, 33-37.
25. Reiff, S. C.; LaVerne, J. A., Radiation-Induced Chemical Changes to Iron Oxides. *The Journal of Physical Chemistry B* **2015**, *119*, 7358-7365.
26. Emmett, P.; Livingston, R.; Zeldes, H.; Kokes, R., Formation of Hydrogen Atoms in Irradiated Catalysts. *The Journal of Physical Chemistry* **1962**, *66*, 921-923.
27. Weeks, R. A.; Abraham, M., Electron Spin Resonance of Irradiated Quartz: Atomic Hydrogen. *The Journal of Chemical Physics* **1965**, *42*, 68-71.
28. Le CaÃ«r, S.; Rotureau, P.; Brunet, F.; Charpentier, T.; Blain, G.; Renault, J. P.; Mialocq, J. C., Radiolysis of Confined Water: Hydrogen Production at a High Dose Rate. *ChemPhysChem* **2005**, *6*, 2585-2596.
29. Kulis, P.; Springis, M.; Tale, I.; Vainer, V.; Valbis, J., Impurity-Associated Colour Centres in Mg-and Ca-Doped Al2o3 Single Crystals. *physica status solidi (b)* **1981**, *104*, 719-725.
30. Lee, K.-H.; Holmberg, G.; Crawford, J., Optical and Esr Studies of Hole Centers in Γ-Irradiated Al2o3. *physica status solidi (a)* **1977**, *39*, 669-674.
31. Nakazato, C.; Masuda, T., Reactivity of Electrons Produced in Gamma-Irradiated Zeolite toward Several Electron Scavengers. *Bulletin of the Chemical Society of Japan* **1986**, *59*, 2237-2239.
32. Teolis, B. D.; Shi, J.; Baragiola, R. A., Formation, Trapping, and Ejection of Radiolytic O2 from Ion-Irradiated Water Ice Studied by Sputter Depth Profiling. *The Journal of Chemical Physics* **2009**, *130*, 134704.
33. Laffon, C.; Lacombe, S.; Bournel, F.; Parent, P., Radiation Effects in Water Ice: A near-Edge X-Ray Absorption Fine Structure Study. *J Chem Phys* **2006**, *125*, 204714.
34. Ghormley, J. A.; Stewart, A. C., Effects of Γ-Radiation on Ice1. *Journal of the American Chemical Society* **1956**, *78*, 2934-2939.
35. Bednarek, J.; Plonka, A., Single-Crystal Electron Spin Resonance Studies on Radiation-Produced Species in Ice I H. Part 1.—the O–Radicals. *Journal of the Chemical Society, Faraday Transactions 1: Physical Chemistry in Condensed Phases* **1987**, *83*, 3725-3735.
36. Parent, P.; Laffon, C., Adsorption of Hcl on the Water Ice Surface Studied by X-Ray Absorption Spectroscopy. *The Journal of Physical Chemistry B* **2005**, *109*, 1547-1553.
37. Rosenberg, R. A. L., P. R. Rehn, Victor Stöhr, J. Jaeger, R. Parks, C. C., K -Shell Excitation of D 2 O and H 2 O Ice: Photoion and Photoelectron Yields. *Physical Review B* **1983**, *28*, 3026-3030.
38. Lefort, M. C. a. M., Sur Le Mécanisme Chimique Primaire De Radiolyse De L'eau. *Journal de chimie physique* **1955**, *52*, 545-555.

39. J.A. Ghormley, a. A. O. A., A. E. C, In *115th American Chemical Society Meeting* San Franciscom California, 1949.
40. Scheuer, W. D. a. O., Décomposition De L'eau Par Les Rayons. *Compt. Rend* **1913**, *156*, 466-467.
41. P. Gunther, a. L. H., Quantum Yields of Gas Reactions Induced by Shortwave Ultra-Violet Light. *Z. Physik. Chem* **1939**, 374.
42. Alig, R.; Bloom, S., Electron-Hole-Pair Creation Energies in Semiconductors. *Physical review letters* **1975**, *35*, 1522.
43. Ranby, B.; Rabek, J. F., *Esr Spectroscopy in Polymer Research*; Springer Science & Business Media, **2012**; Vol. 1.
44. Crawford, J. H.; Slifkin, L. M., *Point Defects in Solids: General and Ionic Crystals*; Springer Science & Business Media, 2013.
45. Gamble, F. T.; Bartram, R. H.; Young, C. G.; Gilliam, O. R.; Levy, P. W., Electron-Spin Resonances in Gamma-Ray-Irradiated Aluminum Oxide. *Physical Review* **1964**, *134*, A589-A595.
46. Joshi, N.; Garg, A., Energy Transfer in the Gamma Radiolytic Decomposition of Sodium and Potassium Nitrates Dispersed in Phosphate, Sulfate and Carbonate Matrices in Solid State. *Radiation effects and defects in solids* **1994**, *132*, 281-291.
47. La, S. Y.; Bartram, R. H.; Cox, R. T., The F+ Center in Reactor-Irradiated Aluminum Oxide. *Journal of Physics and Chemistry of Solids* **1973**, *34*, 1079-1086.
48. Kiiko, V. S.; Zabolotskaya, E. V.; Zolotukhina, L. V.; Frolov, N. M.; Dmitriev, I. A.; Makurin, Y. N., Paramagnetic Defects in Aluminum Oxide Nanopowders and Ceramics Based on These Powders. *Glass and Ceramics* **2001**, *58*, 111-114.
49. Ollier, N.; Rizza, G.; Boizot, B.; Petite, G., Effects of Temperature and Flux on Oxygen Bubble Formation in Li Borosilicate Glass under Electron Beam Irradiation. *Journal of applied physics* **2006**, *99*, 073511.
50. Kuruc, J., Paramagnetic Centers by X-Ray-Irradiation of Aluminium Hydroxide. *Journal of Radioanalytical and Nuclear Chemistry* **1991**, *154*, 61-72.
51. De Las Cuevas, C.; Miralles, L.; Pueyo, J. J., The Effect of Geological Parameters on Radiation Damage in Rock Salt: Application to Rock Salt Repositories. *Nuclear technology* **1996**, *114*, 325-336.
52. Shiyan, I. N.; Serikov, L. V.; Smekalina, T. V.; Vasiliev, A. A., Epr Studies of Aluminium Oxide Phase Compositions. *Reaction Kinetics and Catalysis Letters* **1990**, *41*, 291-294.
53. Blaginina, L.; Zatsepin, A.; Dmitriev, I., Paramagnetic Centers at Tricoordinated Oxygen in Beryllium Alumosilicate Glasses. **1987**.
54. Steinike, U.; Barsova, L. I.; Jurik, T. K.; Kretchmar, U.; Hennig, H. P.; Bol'mann, U., Nature of Mechanically Induced Defects in Polycrystalline Hydrargillite and Al2o3-A1(Oh)3 Studied by Radiation Methods. *Bulletin of the Academy of Sciences of the USSR, Division of chemical science* **1990**, *39*, 1321-1324.
55. L. I. Barsova, T. K. Y., and V. I. Spitsyn, Formation of Vacancies in the Thermal Decomposition of Hydroxides of Alikaline-Earth Metals. *Izvestiya Akademii Nauk SSSR, Seriya Khimicheskaya* **1985**, 12223-1227.
56. Barsova, L. I.; Yurik, T. K.; Spitsyn, V. I., Radiation Centers in Alkaline-Earth Hydroxides. *Bulletin of the Academy of Sciences of the USSR, Division of chemical science* **1984**.
57. Spitsyn, V. I.; Yurik, T. K.; Barsova, L. I., Atomic Hydrogen In. Gamma. - Irradiated Hydroxides of Alkaline-Earth Elements. *Journal Name: Bull. Acad. Sci. USSR, Div. Chem. Sci. (Engl. Transl.); (United States); Journal Volume: 31:4; Other*

Information: Translated from Izv. Akad. Nauk SSSR; No. 4, 762-768(Apr 1982) **1982**, Medium: X; Size: Pages: 672-677.
58. L.I.Barsova, T. K. Y., S. L. Orlov, and M. B. Zubareva, Radiolytic Conversions of Strontium and Barium Hydroxides and Their Crystal Hydrates. *Khimiya Vysokikh Energii* **1990**, *24*, 329-334.
59. Yurik, T. K., Ionova, G.V., Barsova, L.I., & Spitsyn, Esr Investigation of Hydrogen Atoms Stabilized in Γ-Irradiated Alkaline Earth Hydroxides. *Radiation Effects* **1988**, *106*, 87-98. .
60. Barsova, L. I.; Yurik, T. K.; Spitsyn, V. I., Radiation Centers in Alkaline-Earth Hydroxides. *Journal Name: Bull. Acad. Sci. USSR, Div. Chem. Sci. (Engl. Transl.); (United States); Journal Volume: 35:5; Other Information: Translated from Izvestiya Akademii Nauk SSSR, Seriya Khimicheskaya; 35: No.5, 969-974(May 1986)* **1986**, Medium: X; Size: Pages: 879-883.
61. Symons, M. C., Electron Spin Resonance Studies of· Oh and· O–Radicals in Irradiated Ice. Journal of the Chemical Society, Faraday Transactions 1: Physical Chemistry in Condensed Phases. *Journal of the Chemical Society, Faraday Transactions 1: Physical Chemistry in Condensed Phases* **1982**, *78*, 1953-1959.
62. Marks, J.; Wenckebach, W. T.; Poulis, N. J., Properties of Electron-Irradiation-Produced O 2 - in Ca(Oh) 2. *Journal of Physics C: Solid State Physics* **1980**, *13*, 5481.
63. Praliaud, H.; Coluccia, S.; Deane, A.; Tench, A., Oxidising Properties of Mgo Formed by Thermal Decomposition of Mg (Oh) 2. *Chemical Physics Letters* **1979**, *66*, 44-47.
64. Vedrine, J. C.; Imelik, B.; Derouane, E. G., Influence of the Physical State of Three Different Aluminum Hydroxides on the Interaction between Trapped H Atom and Lattice Protons: An Epr and Endor Study. *Journal of Magnetic Resonance (1969)* **1974**, *16*, 95-109.
65. Box, H. C.; Budzinski, E. E.; Lilga, K. T.; Freund, H. G., Endor Study of X-Irradiated Single Crystals of Ice. *The Journal of Chemical Physics* **1970**, *53*, 1059-1065.
66. Johnson, J. E.; Moulton, G. C., Esr Study of Ice Irradiated at 4.2 K, a Thermally Reversible Radical. *The Journal of Chemical Physics* **1978**, *69*, 3108-3111.
67. Scholz, G., & Stösser, R. , Atomic Hydrogen as Spin Probe in Thermally and Mechanically Activated Materials. *Physical Chemistry Chemical Physics* **2002**, *4*, 5448-5457.
68. LaVerne, J. A., H2 Formation from the Radiolysis of Liquid Water with Zirconia. *The Journal of Physical Chemistry B* **2005**, *109*, 5395-5397.
69. Jiang, N.; Spence, J. C., In Situ Eels Study of Dehydration of Al (Oh) 3 by Electron Beam Irradiation. *Ultramicroscopy*, *111*, 860-864.
70. Jay A. LaVerne, a. L. T., H2 and Cl2 Production in the Radiolysis of Calcium and Magnesium Chlorides and
Hydroxides. *Journal of Physical Chemistry* **2005**, *109*, 2861-2865.
71. Kloprogge, J. T.; Ruan, H. D.; Frost, R. L., Thermal Decomposition of Bauxite Minerals: Infrared Emission Spectroscopy of Gibbsite, Boehmite and Diaspore. *Journal of materials science* **2002**, *37*, 1121-1129.
72. Alphonse, P.; Courty, M., Structure and Thermal Behavior of Nanocrystalline Boehmite. *Thermochimica Acta* **2005**, *425*, 75-89.
73. Hasegawa, A. W. a. S., Relative Humidity-Temperature Relationships of Some Saturated Salt Solutions in the Temperature. Range 0 to 50c *Journal of Research of the National Bureau of Standards* **1954**, *Vol. 53*, 19-26.

74. Greenspan, L., Humidity Fixed Points of Binary Saturated Aqueous Solutions. *Journal of Research of the National Bureau of Standards - A* **1977**, *81A*, 89-96
75. Haschke, J. M.; Ricketts, T. E., Adsorption of Water on Plutonium Dioxide. *Journal of Alloys and Compounds* **1997**, *252*, 148-156.
76. Sutto, T. E., One-Step Bulk Synthesis of Stable, near Unit-Cell Sized Oxide Nanoparticles and Nanoparticle Blends Using Ko2. *Inorganic Chemistry*, *53*, 4570-4578.
77. Sutton, H. C., A Calibration of the Fricke Chemical Dosimeter. *Physics in Medicine and Biology* **1956**, *1*, 153.
78. Fricke, H. H., J. E, Attix, F. H., Roesch, W. C., Eds.; , In Radation Dosimetry, 2nd Ed. *Academic Press: New York and London* **1966**, *2*, 167.
79. Chatterjee, A.; Magee, J. L., Radiation Chemistry of Heavy-Particle Tracks. 2. Fricke Dosimeter System. *The Journal of Physical Chemistry* **1980**, *84*, 3537-3543.
80. Senvar, C., Chemical Dosimetry of Gamma Rays, Neutrons, and Accelerated Electrons. *Communs. faculte sci. univ. Ankara* **1960**, *8*.
81. Klassen, N.; Shortt, K.; Seuntjens, J.; Ross, C., Fricke Dosimetry: The Difference between G (Fe3+) for 60co-Rays and High-Energy X-Rays. *Physics in medicine and biology* **1999**, *44*, 1609.
82. Eduardo deAlmeida, C.; Ochoa, R.; de Lima, M. C.; David, M. G.; Pires, E. J.; Peixoto, J. G.; Salata, C.; Bernal, M. A. n., A Feasibility Study of Fricke Dosimetry as an Absorbed Dose to Water Standard for 192 Ir Hdr Sources. *PloS one*, *9*, e115155.
83. Buxton, G. V.; Stuart, C. R., Re-Evaluation of the Thiocyanate Dosimeter for Pulse Radiolysis. *Journal of the Chemical Society, Faraday Transactions* **1995**, *91*, 279-281.
84. Bradshaw, W. W.; Cadena, D. G.; Crawford, G. W.; Spetzler, H. A. W. C. F. p. d. J., The Use of Alanine as a Solid Dosimeter. *Radiation research* **1962**, *17*, 11-21.
85. McLaughlin, W., Esr Dosimetry. *Radiation Protection Dosimetry* **1993**, *47*, 255-262.
86. Mierzwińska, G., Michalec, B., OGŁODEK, I., Petelenz, B., & Waligorski, M. P. R., Alanine/Epr Dosimetry as a Potential Tool for Quality Assurance in Proton Beam Radiotherapy. *Romanian Reports in Physics*, *66*, 54-60.
87. Scherrer, P., Bestimmung Der Grösse Und Der Inneren Struktur Von Kolloidteilchen Mittels Röntgenstrahlen. *Nachr. Ges. Wiss. Göttingen* **1918**, *26*, 98-100.
88. Mierzwińska, G.; Michalec, B.; OGŁODEK, I.; Petelenz, B.; Waligorski, M., Alanine/Epr Dosimetry as a Potential Tool for Quality Assurance in Proton Beam Radiotherapy. *Romanian Reports in Physics* **2014**, *66*, 54-60.
89. Palmer, D. A., Bénézeth, P., Wesolowski, D. J., & Hilic, S. , Experimental Studies of the Solubilities of Aluminum Oxy-Hydroxy Phases to 300 C. **2001**.
90. Panias, D.; Asimidis, P.; Paspaliaris, I., Solubility of Boehmite in Concentrated Sodium Hydroxide Solutions: Model Development and Assessment. *Hydrometallurgy* **2001**, *59*, 15-29.
91. Park, S. Y.; Kim, J. S.; Lee, J. B.; Esler, M. B.; Davis, R. S.; Wielgosz, R. I., A Redetermination of the Argon Content of Air for Buoyancy Corrections in Mass Standard Comparisons. *Metrologia* **2004**, *41*, 387.
92. A.Boumaza a, e., L.Favaro a, J.Le´dion b, G.Sattonnay a, J.B.Brubach c, P.Berthet d, A.M.Huntz a, P.Royc,a, R.Te´ tot a,, Transition Alumina Phases Induced by Heat Treatment of Boehmite: An X-Ray Diffraction and Infrared Spectroscopy Study. *Journal of solid state chemistry* **2009**, 1171–1176.

93. Johnston, C. T., Wang, S. L., & Hem, S. L. , Measuring the Surface Area of Aluminum Hydroxide Adjuvant *Journal of pharmaceutical sciences* **2002**, *VOL. 91*.
94. Ramesh, T. N., Polytypic Transformations of Aluminum Hydroxide: A Mechanistic Investigation. *Particuology*, *10*, 359-364.
95. Lefevre, G. g.; Duc, M.; Lepeut, P.; Caplain, R.; FÃ©doroff, M., Hydration of Î³-Alumina in Water and Its Effects on Surface Reactivity. *Langmuir* **2002**, *18*, 7530-7537.
96. Kolesova, V.; Ryskin, Y. I., Infrared Absorption Spectrum of Hydroargillite Al (Oh) 3. MEZHDUNARODNAYA KNIGA 39 DIMITROVA UL., 113095 MOSCOW, RUSSIA: 1959; Vol. 7, pp 261-263.
97. Freund, F., Infrarotspektren Von Mg (Oh) 2 Bei Erhöhten Temperaturen. *Spectrochimica Acta Part A: Molecular Spectroscopy*, *26*, 195-205.
98. Fripiat, J. J.; Bosmans, H. J.; Rouxhet, P. G., Proton Mobility in Solids. I. Hydrogenic Vibration Modes and Proton Delocalization in Boehmite. *The Journal of Physical Chemistry* **1967**, *71*, 1097-1111.
99. Kiss, A.; Keresztury, G.; Farkas, L., Raman and Ir Spectra and Structure of Boehmite (Γ-Alooh). Evidence for the Recently Discarded D 17 2h Space Group. *Spectrochimica Acta Part A: Molecular Spectroscopy* **1980**, *36*, 653-658.
100. Boumaza, A.; Djelloul, A.; Guerrab, F., Specific Signatures of A-Alumina Powders Prepared by Calcination of Boehmite or Gibbsite. *Powder Technology* **2010**, *201*, 177-180.
101. Gadzhieva, N. N., Oxidation and Accumulation of H2 in the Aluminum-Water System under the Radiation-Thermal Action. *Journal of Applied Spectroscopy* **2005**, *72*, 471-477.
102. Busing, W.; Levy, H. A., A Single Crystal Neutron Diffraction Study of Diaspore, Alo (Oh). *Acta Crystallographica* **1958**, *11*, 798-803.
103. Nakamoto, K., Infrared and Raman Spectra of Inorganic and Coordination Compounds. In *Handbook of Vibrational Spectroscopy*, John Wiley & Sons, Ltd: 2006.
104. Ruan, H. D.; Frost, R. L.; Kloprogge, J. T., Comparison of Raman Spectra in Characterizing Gibbsite, Bayerite, Diaspore and Boehmite. *Journal of Raman Spectroscopy* **2001**, *32*, 745-750.
105. Huang, E.; Li, A.; Xu, J.-a.; Chen, R.-J.; Yamanaka, T., High-Pressure Phase Transition in Al(Oh)3: Raman and X-Ray Observations. *Geophysical Research Letters* **1996**, *23*, 3083-3086.
106. Takamura, T.; Koezuka, J., Infra-Red Evidence of the Grinding Effect on Hydrargillite Single Crystals. **1965**.
107. Kloprogge, J. T.; Duong, L. V.; Wood, B. J.; Frost, R. L., Xps Study of the Major Minerals in Bauxite: Gibbsite, Bayerite and (Pseudo-)Boehmite. *Journal of Colloid and Interface Science* **2006**, *296*, 572-576.
108. Rotole, J. A.; Sherwood, P. M. A., Gibbsite (A-Al(Oh)3) by Xps. *Surface Science Spectra* **1998**, *5*, 25-31.
109. Rotole, J. A.; Sherwood, P. M. A., Nordstrandite (Al(Oh)3) by Xps. *Surface Science Spectra* **1998**, *5*, 32-38.
110. Rotole, J. A.; Sherwood, P. M. A., Bayerite (B-$Al(Oh)_3$) by Xps. *Surface Science Spectra* **1998**, *5*, 39-45.
111. Rotole, J. A.; Sherwood, P. M. A., Diaspore (B-Alooh) by Xps. *Surface Science Spectra* **1998**, *5*, 46-52.
112. Rotole, J. A.; Sherwood, P. M. A., Boehmite (Γ-Alooh) by Xps. *Surface Science Spectra* **1998**, *5*, 53-59.

113. Hall, P. L., The Application of Electron Spin Resonance Spectroscopy to Studies of Clay Minerals: I. Isomorphous Substitutions and External Surface Properties. *Clay Miner* **1980**, *15*, 321-335.
114. Yves, B.; Bruno, D.; Sandrine, C.; Jean-Victor, Z., Electron Spin Resonance and Dilatometric Studies of Ancient Ceramics Applied to the Determination of Firing Temperature. *Japanese Journal of Applied Physics* **1998**, *37*, 4367.
115. Galamboš, M., Daňo, M., Rosskopfová, O., Šeršeň, F., Kufčáková, J., Adamcová, R., & Rajec, P., Effect of Gamma-Irradiation on Adsorption Properties of Slovak Bentonites. *Journal of Radioanalytical and Nuclear Chemistry*, *292*, 481-492.
116. Brunauer, S.; Emmett, P. H.; Teller, E., Adsorption of Gases in Multimolecular Layers. *Journal of the American Chemical Society* **1938**, *60*, 309-319.
117. Brunauer S, E. P., Teller E. . 1938;60:309e19., Desorption of Gases in Multimolecular Layers. *J Am Chem Soc* **1938**, *60*, 309-319.
118. Frost, R. L.; Kloprogge, J. T.; Russell, S. C.; Szetu, J., Dehydroxylation of Aluminum (Oxo)Hydroxides Using Infrared Emission Spectroscopy. Part Ii: Boehmite. *Applied Spectroscopy* **1999**, *53*, 572-582.
119. Frost, R. L.; Kloprogge, J. T.; Russell, S. C.; Szetu, J., Dehydroxylation and the Vibrational Spectroscopy of Aluminum (Oxo)Hydroxides Using Infrared Emission Spectroscopy. Part Iii: Diaspore. *Applied Spectroscopy* **1999**, *53*, 829-835.
120. Frost, R. L.; Kloprogge, J. T.; Russell, S. C.; Szetu, J. L., Vibrational Spectroscopy and Dehydroxylation of Aluminum (Oxo)Hydroxides: Gibbsite. *Applied Spectroscopy* **1999**, *53*, 423-434.
121. Griscom, D. L., Diffusion of Radiolytic Molecular Hydrogen as a Mechanism for the Post-Irradiation Buildup of Interface States in Sio2-on-Si Structures. *Journal of Applied Physics* **1985**, *58*, 2524-2533.
122. Chen, W., Optically Detected Magnetic Resonance of Defects in Semiconductors. In *Epr of Free Radicals in Solids*, Lund, A.; Shiotani, M., Eds. Springer US: 2003; Vol. 10, pp 601-625.
123. Janak, J. F., G Factor of the Two-Dimensional Interacting Electron Gas. *Physical Review* **1969**, *178*, 1416-1418.
124. Chen, W. M., *Epr of Free Radicals in Solids Ii. Trends in Methods and Applications. Chapter: Optically Detected Magnetic Resonance of Defects in Semiconductors.*, 2nd ed.; Springer.
125. Leroy, G.; Sana, M.; Tinant, A., Étude Théorique Des Réactions D'abstraction D'hydrogène, Avec R, X≍ H, Ch3, Nh2, Oh Et F. *Canadian journal of chemistry* **1985**, *63*, 1447-1456.
126. LaVerne, J. A.; Tonnies, S. E., H2 Production in the Radiolysis of Aqueous Sio2 Suspensions and Slurries†. *The Journal of Physical Chemistry B* **2003**, *107*, 7277-7280.
127. Brodie-Linder, N., Le Caër, S., Alam, M. S., Renault, J. P., & Alba-Simionesco, C, H 2 Formation by Electron Irradiation of Sba-15 Materials and the Effect of Cuii Grafting. *Physical Chemistry Chemical Physics* **2010**, *12*, 14188-14195.
128. Tenchurina, A.; Sal'keeva, A., Radiolysis and Photolysis of Sodium Sulfate Crystalline Hydrate. *Russian Journal of Physical Chemistry A* **2016**, *90*, 688-690.
129. Agency, I. A. E. *Spent Fuel Storage and Transport Cask Decontamination and Modification* 1999.

8. Appendix

Appendix A: TN 12 casks

TN 12 casks are used to carry twelve fuel assemblies from the 900 MW (e) reactors while TN 13 casks are used to carry twelve spent fuel assemblies, from the 1300 and 1450 MW (e) stations. The TN 12 and TN 13 casks are identical, except the length.[129]

TN 12 casks are used to carry twelve fuel assemblies from the 900 MW (e) reactors while TN 13 casks are used to carry twelve spent fuel assemblies, from the 1300 and 1450 MW (e) stations. The TN 12 and TN 13 casks are identical, except the length.[129] A description of the TN12 is shown in **Erreur ! Source du renvoi introuvable.**.

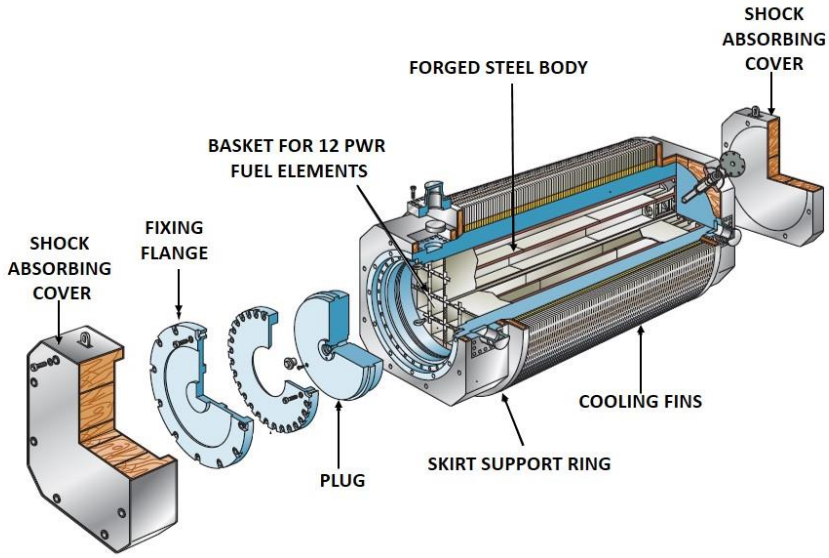

Figure 8.1. TN 12/2 cask for nuclear waste transportation (AREVA TN).

The TN12 is made of two parts:

- A body with a double closure system and two shock absorbers,
- A basket designed to receive 12 fuel assemblies.

The basket is made of modules with a neutron absorber material allowing also satisfactory heat exchange conditions. Cask cavity and baskets are dried for seven hours between 150 and 200°C under vacuum and they are tight sealed before transportation.

The internal basket designed specifically for a high decay heat load allows individual assemblies with up to 6 kW and a total power of 50 kW (for the 12 fuel assemblies). In order to better evacuate heat and improve pitting resistance,

Appendix B: EPR spectra of hydrated AlOOH and $Al(OH)_3$

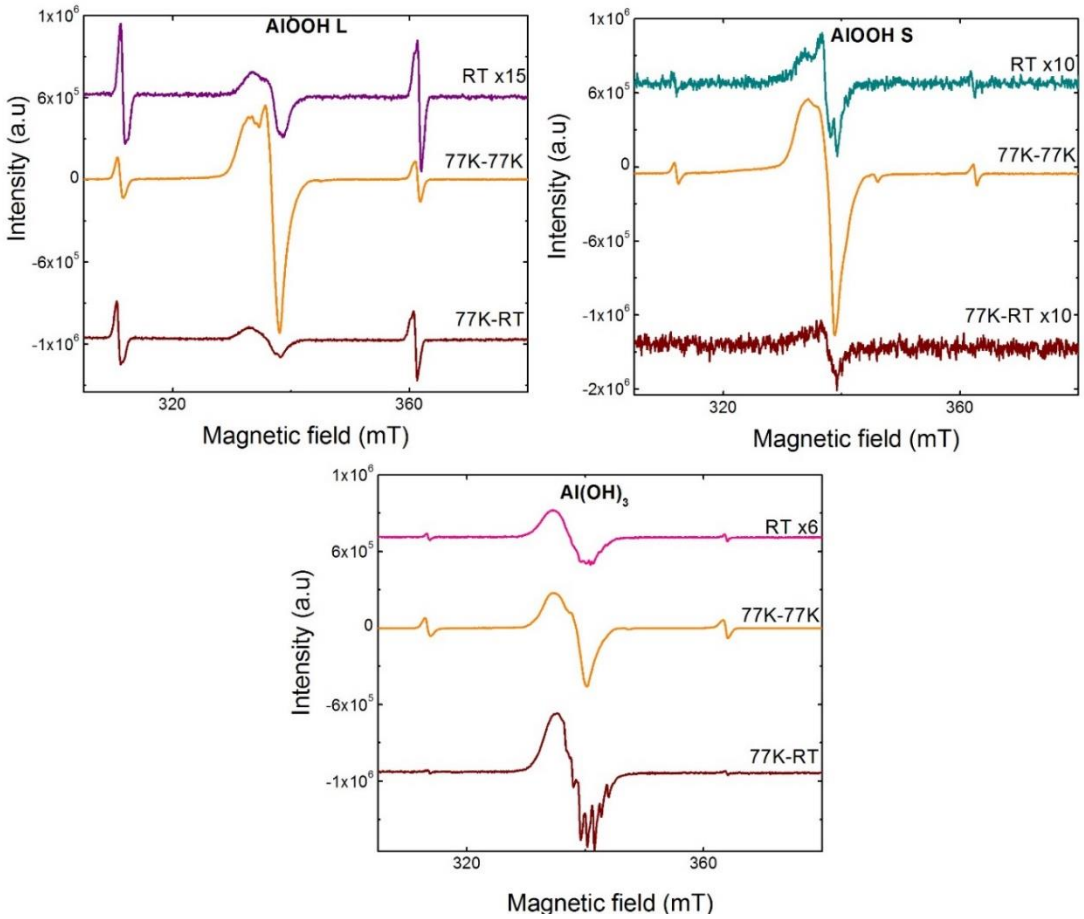

Figure 8.2. EPR spectra of electron irradiated AlOOH L, S and $Al(OH)_3$. RT indicated in the first line significates irradiation and analyze at RT, 77K-77K significates irradiation and analyze at 77K and 77K-RT significates irradiation at 77K and analyze at RT

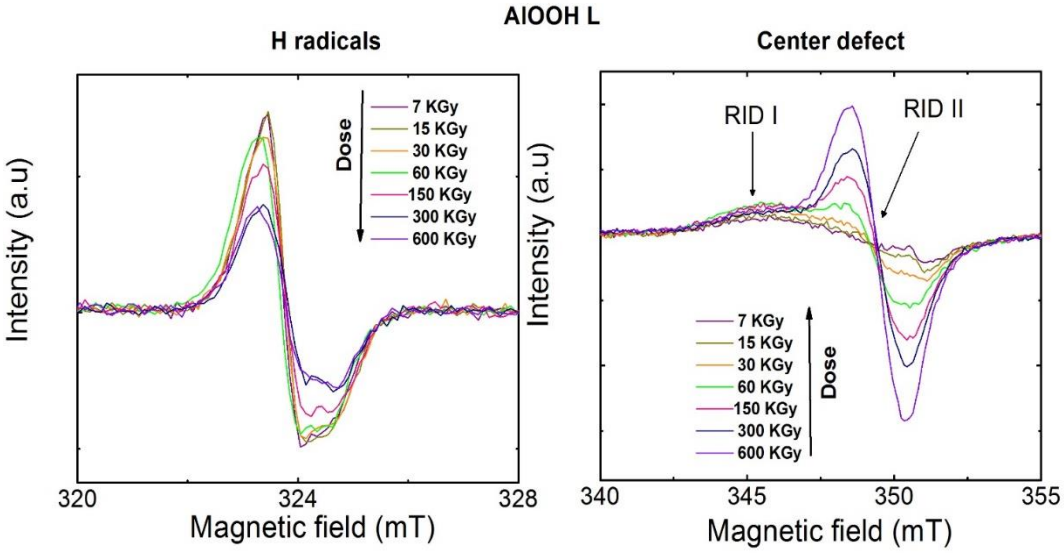

Figure A 8.1. Evolution of H radicals and radiation induced defects as a function of the dose in electron beam-irradiated AlOOH L.

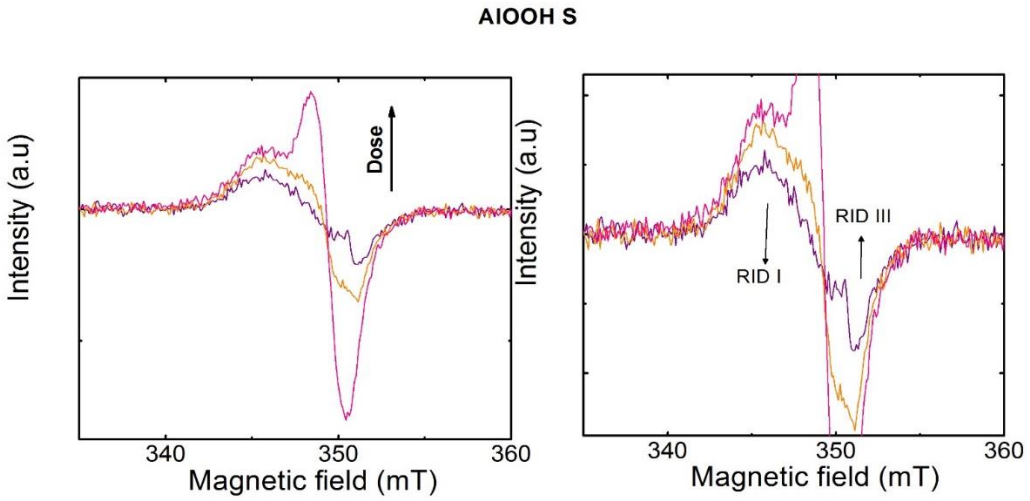

Figure 8.3. Evolution of RID I and RID II as a function of the dose in electron beam-irradiated AlOOH L. Purple, orange and pink represents 7, 15 and 30 kGy respectively.

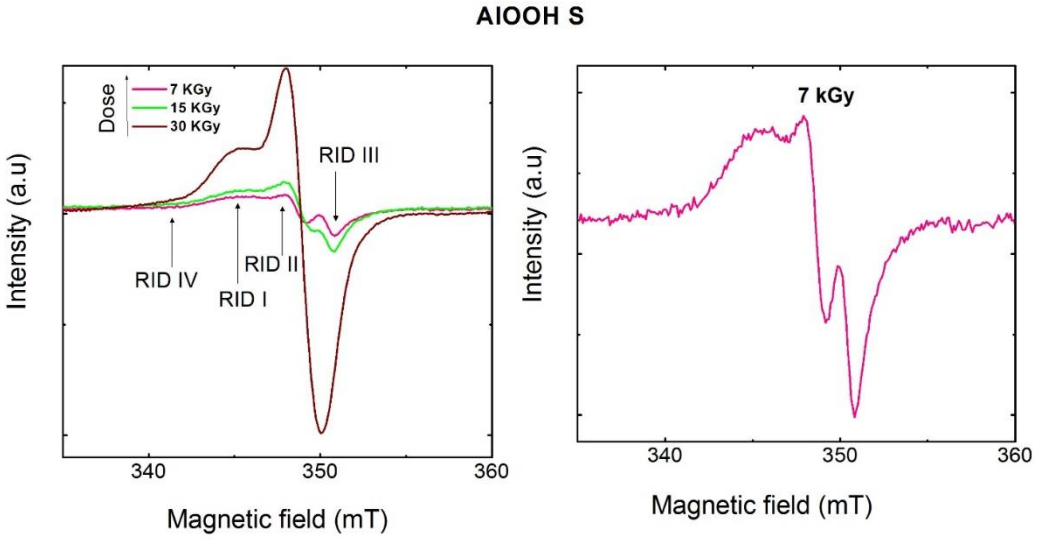

Figure 8.4. Evolution radiation induced defects as a function of the dose in electron beam-irradiated AlOOH S. At low doses (figure on the right) the EPR spectra is shown in order to compare it with that at 30 kGy.

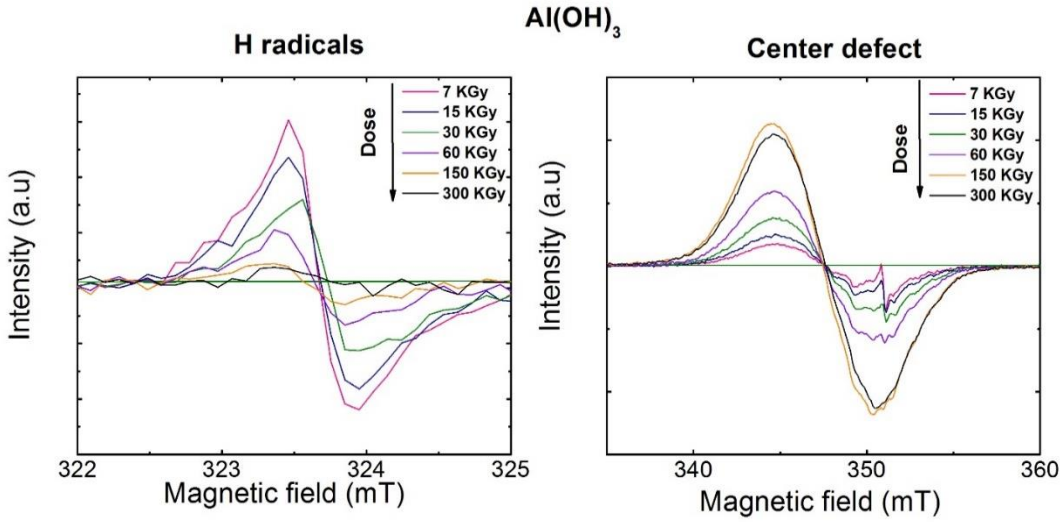

Figure 8.5. Evolution of H radicals and radiation induced defects as a function of the dose in electron beam-irradiated $Al(OH)_3$.

université PARIS-SACLAY | ÉCOLE DOCTORALE Sciences chimiques : molécules, matériaux, instrumentation et biosystèmes

Titre : Production de dihydrogène par irradiation d'hydroxyde et d'oxohydroxide d'aluminium

Mots clés : Radiolyse, eau de structure, irradiation, hydroxide d'aluminium, défauts sous irradiation

Résumé : Dans le cadre de l'entreposage et du stockage des colis de déchets nucléaires et du transport de combustibles usés, nous nous sommes intéressés par l'étude de la production d'hydrogène de deux produits de corrosion de l'aluminium : l'hydroxyde d'aluminium ($Al(OH)_3$) et l'oxyhydroxyde d'aluminium (AlO(OH)). La production du dihydrogène par irradiation de ces matériaux a été étudiée en fonction de la taille et de la structure que ce soit à température ambiante ou après recuit. Afin d'avoir une meilleur compréhension des mécanismes de production de ce gaz, les défauts créés par irradiation ont été caractérisés en utilisant la Résonnance Paramagnétique Electronique (RPE). Différentes sources d'irradiation ont été utilisées comme le rayonnement Gamma, les électrons accélérés et les ions lourds. Dans un second temps, l'effet de l'hydratation de surface des matériaux a été également étudié. Enfin, l'effet de la présence d'impuretés sur la production de H_2 a été brièvement étudié.

Title : Molecular hydrogen production from irradiated aluminum hydroxide and oxyhydroxide

Keywords : Radiolysis, structural water, irradiation, aluminum hydroxide, radiation induced defects

Abstract: Molecular hydrogen production is a critical issue for the current management of nuclear wastes. One potential source of hydrogen generation is the radiolysis of hydrated mineral phases encountered in the nuclear waste transportation and storage casks. We chose to study aluminum hydroxide ($Al(OH)_3$) (Bayerite) and oxyhydroxides (AlOOH) (Boehmite) as model compounds. The determination of molecular hydrogen production was evaluated with respect to structure and particle size at room temperature and after annealing. In order to have a better understanding of the mechanisms and to identify the precursors of molecular hydrogen, we studied the irradiation defects and their stabilities using Electron Paramagnetic Resonance (EPR). The effect of adsorbed water and structural water on the molecular hydrogen production was studied. Different radiation sources were used such as Gamma radiation, electron beam radiations and heavy ions. In the last part, preliminary results related to the impact of impurities on hydrogen production are presented.